FIELD ELECTRON EMISSION FROM DIAMOND AND RELATED FILMS SYNTHESIZED BY PLASMA ENHANCED CHEMICAL VAPOR DEPOSITION

A Thesis Submitted to the College of

Graduate Studies and Research

In Partial Fulfillment of the Requirements

For the Degree of Doctor of Philosophy

In the Department of Physics and Engineering Physics

University of Saskatchewan

Saskatoon

By

XIANFENG LU

Keywords: field electron emission, diamond films, chemical vapor deposition

PERMISSION TO USE

In presenting this thesis in partial fulfilment of the requirements for a Postgraduate degree from the University of Saskatchewan, I agree that the Libraries of this University may make it freely available for inspection. I further agree that permission for copying of this thesis in any manner, in whole or in part, for scholarly purposes may be granted by the professor or professors who supervised my thesis work or, in their absence, by the Head of the Department or the Dean of the College in which my thesis work was done. It is understood that any copying or publication or use of this thesis or parts thereof for financial gain shall not be allowed without my written permission. It is also understood that due recognition shall be given to me and to the University of Saskatchewan in any scholarly use which may be made of any material in my thesis.

Requests for permission to copy or to make other use of material in this thesis in whole or part should be addressed to:

Head of the Department of Physics and Engineering Physics

University of Saskatchewan

Saskatoon, Saskatchewan S7N 5E2

ABSTRACT

The focus of this thesis is the study of the field electron emission (FEE) of diamond and related films synthesized by plasma enhanced chemical vapor deposition. The diamond and related films with different morphologies and compositions were prepared in a microwave plasma-enhanced chemical vapor deposition (CVD) reactor and a hot filament CVD reactor. Various analytical techniques including scanning electron microscopy (SEM), atomic force microscopy (AFM), and Raman spectroscopy were employed to characterize the surface morphology and chemical composition.

The influence of surface morphology on the field electron emission property of diamond films was studied. The emission current of well-oriented microcrystalline diamond films is relatively small compared to that of randomly oriented microcrystalline diamond films. Meanwhile, the nanocrystalline diamond film has demonstrated a larger emission current than microcrystalline diamond films. The nanocone structure significantly improves the electron emission current of diamond films due to its strong field enhancement effect.

The sp^2 phase concentration also has significant influence on the field electron emission property of diamond films. For the diamond films synthesized by gas mixture of hydrogen and methane, their field electron emission properties were enhanced with the increase of methane concentration. The field electron emission enhancement was attributed to the increase of sp^2 phase concentration, which increases the electrical conductivity of diamond films. For the diamond films synthesized through graphite etching, the growth rate and nucleation density of diamond films increase significantly with decreasing hydrogen flow rate. The field electron emission properties of the diamond films were also enhanced with the decrease of hydrogen flow rate. The field electron emission enhancement can be also attributed to the increase of the sp^2 phase concentration.

In addition, the deviation of the experimental Fowler-Nordheim (F-N) plot from a straight line was observed for graphitic nanocone films. The deviation can be mainly attributed to the nonuniform field enhancement factor of the graphitic nanocones. In low macroscopic electric field regions, electrons are emitted mainly

from nanocone or nanocones with the largest field enhancement factor, which corresponds to the smallest slope magnitude. With the increase of electric field, nanocones with small field enhancement factors also contribute to the emission current, which results in a reduced average field enhancement factor and therefore a large slope magnitude.

ACKNOWLEDGMENTS

This work is supported by the Canada Research Chair Program and Natural Sciences and Engineering Research Council of Canada.

I would like to express my deepest gratitude to my supervisors, Dr. Chijin Xiao and Dr. Akira Hirose. Had they not offered me the opportunity to pursue my education at the University of Saskatchewan and without their constant guidance along the way, this thesis would not have been possible. I am grateful to them for their skillful way of combining guidance and encouragement with trust and freedom, which afforded me the opportunity to rely on my own judgment in pursuing some of the experiments.

I am indebted to Dr. Qiaoqin Yang for her help during the sample preparation and the draft of papers. I am also grateful to David McColl for his help during the construction of the experimental apparatus. He has voluntarily offered help on many occasions, and has always been kind, supportive and generous. Thanks also to Dr.Yuanshi Li for valuable discussions on some experiments.

Assistance from Weifeng Chen in the operation of the microwave CVD system and on sample preparation; from Dr. Ramaswami Sammynaiken for his help in Raman and FTIR characterization; from Tom Bonli with SEM experiments; and from Jason Maley with the AFM tests, are all sincerely appreciated.

On a personal level, I would like to thank my parents for always supporting me unconditionally. Their support and understanding are always appreciated. Finally I would like to thank my wife, Xin Wang, for never hesitating in offering her ideas and suggestions on my personal development, for supporting the whole family, and for always being there for me.

TABLE OF CONTENTS

LIST OF TABLES

LIST OF FIGURES

LIST OF ABBREVIATIONS

AFM	Atomic Force Microscope
BEN	Bias Enhanced Nucleation
CBM	Conduction Band Minimum
CRT	Cathode Ray Tube
CVD	Chemical Vapor Deposition
FCC	Face-Centered-Cubic
FED	Field Emission Display
FEE	Field Electron Emission
FEF	Field Enhancement Factor
F-N	Fowler-Nordheim
GEF	Geometrical Enhancement Factor
HFCVD	Hot Filament Chemical Vapor Deposition
IC	Integrated Circuit
LCD	Liquid Crystal display
MEMS	Micro-ElectroMechanical System
MIV	Metal–Insulator–Vacuum
MPCVD	Microwave Plasma-enhanced Chemical Vapor Deposition
NEA	Negative Electron Affinity
PEA	Positive Electron Affinity
PECVD	Plasma Enhanced Chemical Vapor Deposition
PFEEM	Photo/Field Emission Electron Microscope
RIE	Reactive Ion Etching
SED	Surface-conduction Electron-emitter Display
SEM	Scanning Electron Microscope
SSSC	Saskatchewan Structural Sciences Centre
TEM	Transmission Electron Microscope
UHV	Ultra High Vacuum
WF	Work Function

LIST OF SYMBOLS

a	Lattice constant of diamond
e	Magnitude of electron charge
E	Applied electric field, kinetic energy of electron
E_F	Fermi energy
E_g	Energy band gap
E_{vac}	Vacuum energy potential
F	Local electric field
f	Image force
$f(E, E_F, T)$	Fermi-Dirac statistics
h	Planck's constant
I	Emission current
j	Current density
k	Boltzmann constant
m	Free electron mass
$n(E)$	Electron distribution function
p	Momentum of electron
T	Temperature
V	Surface potential, bias voltage
α	Effective emission area
β	Field enhancement factor
φ	Work function
ε_0	Permittivity of free space
χ	Electron affinity

Chapter 1

Introduction

1.1 Background and Motivation

Advances in electron source technology have had a profound impact on a whole range of applications. Presently, the most widely employed electron source is the 'bulky' thermionic cathode, which is used in CRT and high power vacuum tubes. However, in the quest for miniaturization, recent requirements for electron sources in applications such as flat panel displays, parallel electron beam microscopy, nanolithography, compact microwave amplifiers and portable X-ray tubes have motivated worldwide research on alternative electron sources, which are smaller and more efficient. The field electron emission cold cathode has such a potential. Field electron emission is defined as the emission of electrons from the surface of condensed matter under the action of high electrical field. Compared to the commonly used thermionic emission based on a hot filament, the field electron emission source is more power efficient. In addition, field electron emission sources also offer several attractive characteristics such as instantaneous response to field variation, and resistance to temperature fluctuation and radiation.

This work focuses on the investigation of field electron emission from diamond and related films for both the understanding of fundamental physics and the practical applications.

1.2 The Importance of Field Electron Emission Research

The electron sources of field electron emission can be utilised in many applications such as field emission scanning electron microscopy, field electron emission flat panel displays and many other vacuum microelectronic devices [1-7]. Field emission display (FED) is one of the most important applications [8-10]. FED is a new type of flat-panel display in which electron emitters, arranged in a grid, are individually controlled by "cold" cathodes to generate colored pixels. Currently the main challenge for FED is to find a phosphor that can work under low voltage. A similar technology to be commercialized is the surface-conduction electron-emitter display (SED) [11]. The surface conduction electron emitter apparatus consists of a thin slit across which electrons tunnel when excited by moderate voltages (tens of volts). When the electrons cross electric poles across the thin slit, some are scattered at the receiving pole and are accelerated toward the display surface by a large voltage gradient (tens of kV) between the display panel and the surface conduction electron emitter apparatus. Figure 1-1 shows the working principle of SED.

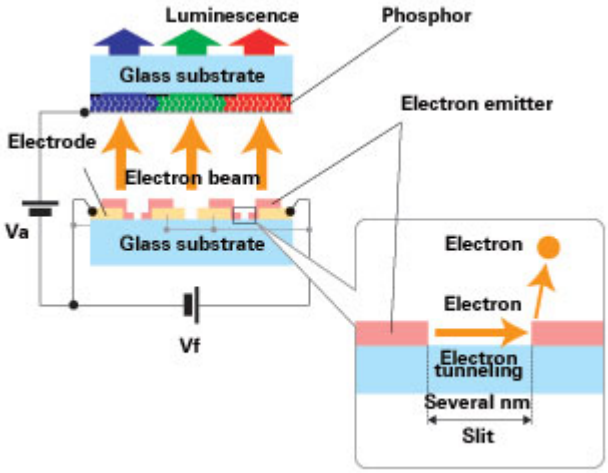

Figure 1-1: Basic working principle of SED [12].

SED has several advantages over the conventional cathode ray tube (CRT) display, Liquid Crystal display (LCD) and plasma display:

- Makes possible the thin flat panel display comparable to today's LCD. As the SED monitor does not require electronic beam deflection, it is possible to make screens that are only few centimeters thick.
- Offers a wider field-of-view than LCD. As the SED monitor works with the same light production theory as CRT monitors, it can provide a sharper, more dynamic color, and a wider field of view than LCDs and plasma displays.
- Increases the overall power efficiency of display. The SED power consumption is only one-half that of a large-screen CRT and about one-third that of a plasma display panel.
- Makes it easy to integrate small SED with other electronic circuits.

In some other situations, it is necessary to eliminate unnecessary or even harmful field electron emission phenomena. For example, field electron emission can happen for metal working under strong electric field. A large emission current will produce large amounts of heat, which can damage the metal. In large-scale integrated circuits (IC), the distance between components is only several micrometers. For such short distances, field electron emission can happen easily even under low voltages. This can influence the performance of components and even destroy the whole device. Studies of field electron emission can help avoid these phenomena.

1.3 Diamond

Diamond has a well-known cubic structure (Figure 1-2). It consists of two face-centered-cubic (fcc) lattices, one of which is displaced by (¼ *a*, ¼ *a*, ¼ *a*), where *a* is the lattice constant of diamond, *a*=3.567 Å (1Å=0.1nm). There are two atoms in a crystallographic unit cell. Each carbon atom has four sp^3 bonds with the neighbouring four atoms where the bond length is 1.54 Å. Since there are two identical atoms per unit cell, only one single band is observed in the Raman spectrum at 1332 cm^{-1}. The atomic density of diamond is 1.77×10^{23}/ cm^3.

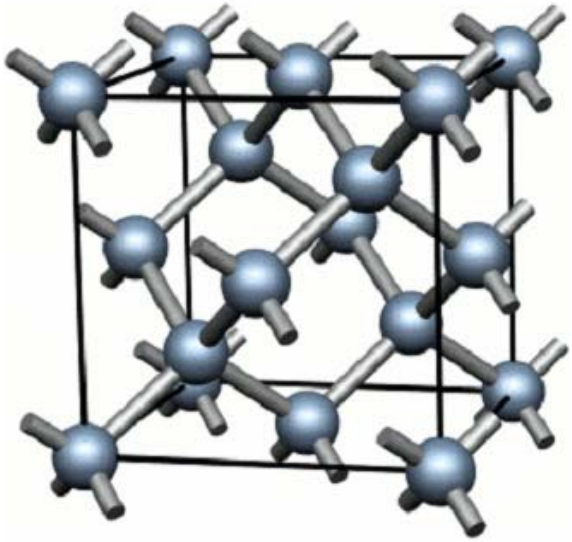

Figure 1-2: Cubic structure of diamond [13].

Diamond is the hardest material in nature and has a high elastic modulus. It is a good electric insulator but excellent thermal conductor, and has a low thermal expansion coefficient. Diamond is also extremely inert chemically. A summary of the properties of bulk diamond is given in Table 1-1.

Table 1-1: Summary of diamond properties.

Property	**Value**	**Units**
Hardness	10	Mohs scale
Young's modulus	1.05×10^{12}	N/m^2
Density	3.52	g/cm^3
Unit cell spacing	0.3567	nm
Nearest neighbor	0.1545	nm
Thermal conductivity	20	W/K/cm
Thermal expansion coefficient	8×10^{-7} (298 K)	1/K
Dielectric constant	5.7	
Band gap	5.47	eV
Resistivity	$> 10^{16}$	Ohm·cm

The superior properties of diamond make it attractive for industrial machining such as grinding, sawing, and drilling. In recent years it has been this unique combination of properties that have made diamond attractive to the electronics community (e.g., high resistivity with high thermal conductivity). Applications ranging

from heat sinks to vacuum microelectronic field emitters have been demonstrated. Furthermore, with recent progress in the development of micro-electromechanical systems (MEMS), the exploitation of diamond for improved electrical, mechanical, and chemical behavior continues.

1.4 Diamond as Cold Cathode Material

1.4.1 Unique Properties of Diamond Beneficial for Field Electron Emission

Cold cathode materials currently used such as carbon nanotubes (CNTs) have some disadvantages in FEE stability and longevity. Some researchers have observed the modification of surface morphology due to the evaporation of CNTs in FEE experiments. Diamond can overcome these problems due to its excellent properties such as good mechanical and chemical stability, high thermal conductivity, and high resilience against radiation [14, 15]. Diamond film also possesses negative electron affinity (NEA), which can make it emit electrons at low electric fields. Major advantages of diamond film for field electron emission applications are: (1) superior electronic properties at high temperatures and harsh environments; (2) high breakdown voltage, electron saturation velocity, carrier mobility, thermal conductivity, and electrical stability for microelectronic devices with very high power and frequency possibilities; (3) wide-band gap and NEA properties for vacuum microelectronics with outstanding power, speed, and radiation hardness; and (4) chemical and electrical stability, compatible with hostile environments for field electron emission applications.

The properties of diamond and related films have been extensively investigated. However, experimental data available on these properties tend to be rather scattered since they are very much dependent on the film growth conditions. Nevertheless, Table 1-2 gives a summary of the properties of various diamond surfaces that are important for understanding field emission phenomena from this material.

Table 1-2: Typical values of energy band-gap E_g, electron affinity χ, and work function ϕ for various diamond surfaces.

Type	**Parameters**		
	E_g **(eV)**	χ **(eV)**	ϕ **(eV)**
Bare diamond	5.47	0.38	4.97
Diamond covered by H	5.47	−1.27	3.52

An important property of diamond is its negative electron affinity. The electron affinity χ is defined as the energy difference between the vacuum level and the conduction band minimum (CBM). The electron affinity value represents the energy needed to extract an electron from the CBM to vacuum. When an electron is raised from the valence band to the CBM by photon excitation in a semiconductor, such an electron is not free to leave the sample because it encounters an energetic barrier of a few eV at the surface, i.e. the electron affinity. Such a semiconductor has a positive electron affinity (PEA). However, an electron at the CBM is free to leave a diamond surface that has NEA.

It is now quite clear that a pure diamond surface has a PEA, but it is small – in the region of ~0.38 eV [15]. If a diamond surface is terminated with hydrogen, it may have negative electron affinity and the exact value depends on the percentage of hydrogen coverage over the surface [15]. For a diamond film synthesized by CVD, its surface will be automatically terminated with hydrogen due to the presence of hydrogen plasma in the synthesis process. For natural diamond, the following steps may be followed to hydrogenate its surface [15]: first, the diamond is subjected to annealing under ultra high vacuum (UHV) conditions at 1400 K for ~12 minutes to remove the surface contamination. This process is then followed by a treatment in hydrogen plasma at about 1100 K for ~10 minutes.

Cui *et al.* attributed the origin of NEA of hydrogenated diamond to the surface electric dipole formed by the C-H bond that is more electronegative to C [15]. The length of the dipole is about 1.1 Å and an electron will see a potential drop in the dipole layer formed by C-H bonds as large as 1.65 eV, which is equivalent to the change in χ from bare to hydrogenated diamond. This value is so large mainly due to

a high density of surface dipoles on account of the small lattice constant of diamond. Also, the short atomic distance over which the potential drops, allows electrons to tunnel readily through the narrow potential barrier.

1.4.2 Field Electron Emission from Diamond Films

1.4.2.1 Deposition Techniques

The diamond films have been prepared mainly by plasma enhanced chemical vapour deposition technology. The growth process essentially consists of two steps and the typical growth conditions in a microwave plasma enhanced CVD reactor are given in Table 1-3 [16]. The first step is the negative bias enhanced nucleation process and the second step is the diamond growth process. Briefly speaking, the CVD technology relies on a sequence of chemical reactions occurring both in the gas phase and on the solid substrate surface.

Table 1-3: Typical conditions for diamond film deposition on a silicon substrate using the microwave CVD technique.

First step	
Pressure (Pa)	4×10^3
Substrate temperature (°C)	690–820
Microwave power (W)	360–620
Reaction sources	CH_4/H_2
Total flow (sccm)	100
CH_4 concentration (%)	1.7
Bias voltage (V)	−250
Time (min)	15
Second step	
Pressure (Pa)	4×10^3
Substrate temperature (°C)	690–820
Microwave power (W)	360–620
Reaction sources	CH_4/H_2
Total flow (sccm)	100
CH_4 concentration (%)	0.5
Time (min)	45

1.4.2.2 Basic FEE Characteristics

Field emission current versus applied electric field (I-E) characteristic: As essential data, field emission currents are recorded at a sequence of vacuum gap voltages. The current–field (*I–E*) data may then be plotted and compared with the Fowler–Nordheim formula. This is to check if the electrons are really emitted by a tunneling process. Figure 1-3 shows the *I–E* curve and its corresponding F-N plot obtained from a diamond film. The details of the F-N plot and its use in determining two important FEE parameters, the effective emission area α and the field enhancement (FEF) β, will be discussed in Chapter 2. It is often necessary to undergo a switch-on process before a reproducible *I–E* characteristic may be observed [17]. From an *I–E* characteristic curve, the current density may be determined by dividing the total current by the total surface area of the sample. This value is useful for checking whether the electron emission meets the requirement for a particular application. For instance, a current density of 10 mA/cm^2 is necessary for a field emission flat panel display. The corresponding electric field necessary for obtaining the above minimum current density can then be determined and may be defined as the threshold field.

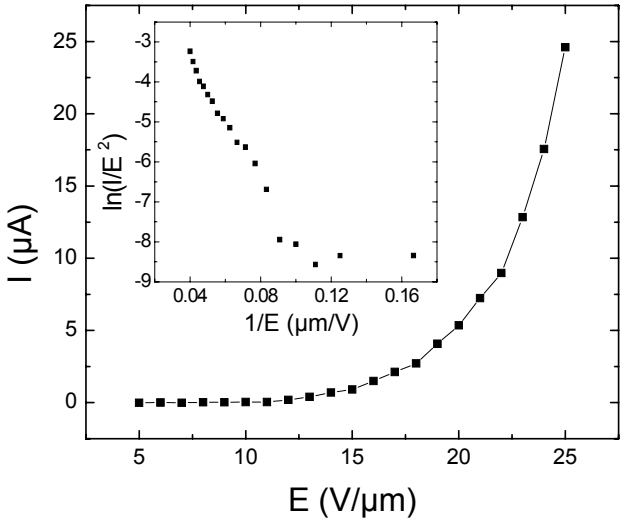

Figure 1-3: The *I–E* curve and the corresponding F–N plot (inset) of a CVD diamond film.

Spatial distribution of emission sites: It has been observed that the electron emission from a substrate surface is nonuniform and the effective emission area α is much smaller than the surface area. This is supported by the experimental evidence collected using the analytical techniques developed independently by Xu *et al.* and Wang *et al.* [18, 19], which reveal that emission is always from localized regions on the surface.

However, a uniform distribution of emission over a flat film is required for large-area applications. Since a good *I–E* characteristic is not enough to provide this information, the transparent anode imaging technique developed by Latham *et al.* has been adapted and extensively used for imaging emission from flat diamond films [20]. The transparent anode consists of a glass disc coated with conducting tin oxide film, so that visible transition radiation can be produced by impacting electrons. Thus, the position of an emission site on the cathode surface is directly marked on the anode by light generated by impacting electrons. Accordingly, the spatial distribution of these pinpoints of light represents a map of emission sites on the surface of the sample. Such a distribution and its variation with time are constantly recorded using a CCD camera directly facing the sample surface. Xu and Latham succeeded in recording the spatial distribution of electron emission from large-area CVD diamond films, as shown in Figure 1-4a [21]. Since the vacuum gap between the anode and the emitting surface is small, the divergence of the electrons from an emission site is not significant. Therefore, the emission sites on the surface of the diamond film correspond to the white spots in the image shown in Figure 1-4a. The value of the site density was obtained by counting the total number of white spots and dividing it by the total area of the sample surface. In addition, the site density was also studied as a function of applied electric field. Comparing Figure 1-4b and c, it is obvious that with increasing field, the site density also increases [22]. This indicates that the emission sites have different *I–E* characteristics: some sites emit at low fields and others at high fields.

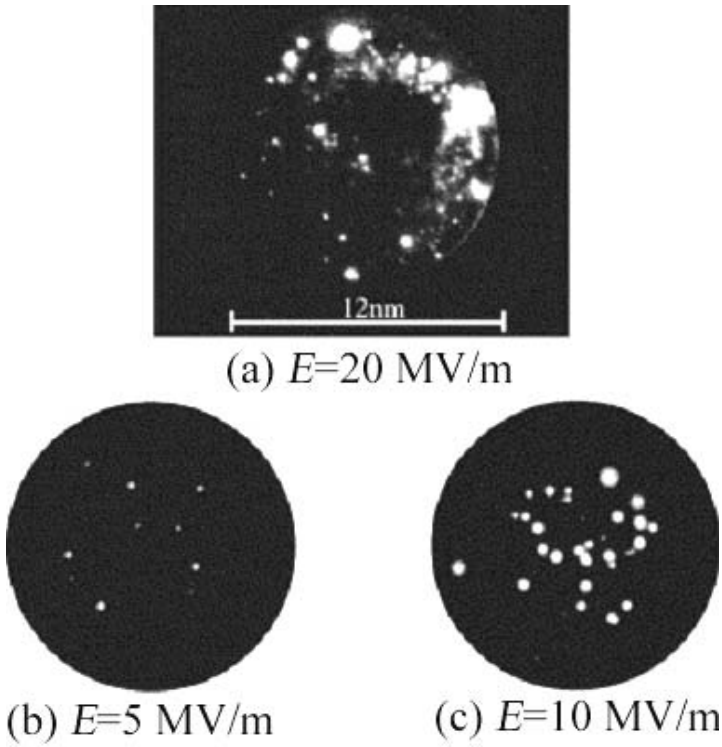

Figure 1-4: (a) The emission-site distribution of a large-area (12 mm in diameter) CVD diamond film. (b) and (c) The site density increases at higher electric field [22].

The spatial distribution of emission sites on the emitting surface with a nanometer resolution can be obtained using the field emission microscopic imaging technique. One may use this method to obtain an enlarged image of a white spot as shown in Figure 1-4. Such a spot in fact often consists of a number of much smaller spots with irregular shapes (top-left of Figure 1-5 [22]). These field emission images contain important information as to which crystalline surface has strong FEE ability. In order to obtain experimental evidence to show the exact correlation between the field electron emission image and the SEM image, the conventional field emission microscopic technique was developed and combined with UV photoelectron emission microscopy. Wang *et al.* employed a projection electron emission microscope to investigate if there is a correlation between the surface feature and the emission site [23]. No such relationship was found with diamond films. But, it may be necessary to use a high-resolution photo/field emission electron microscope (PFEEM) for further studies.

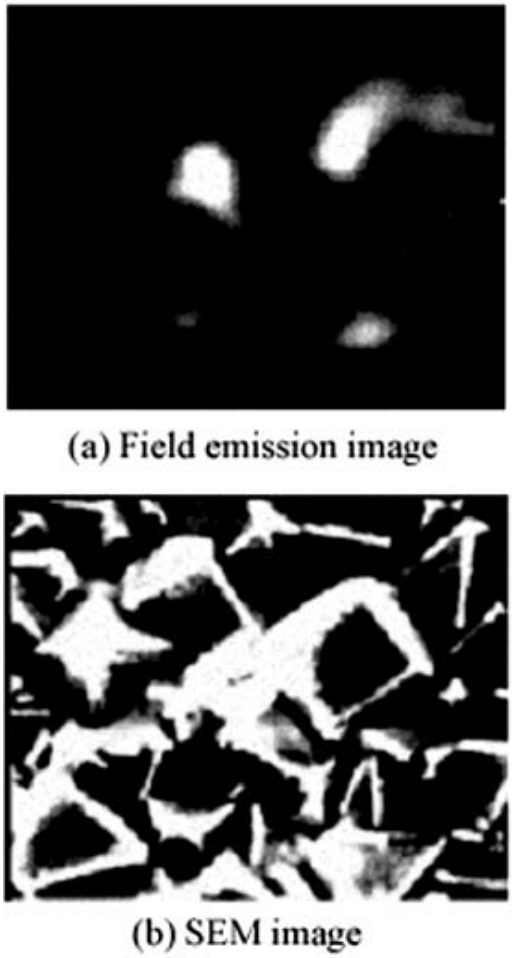

Figure 1-5: Field emission microscopic images of a CVD diamond film may have shapes in rectangular form (a), which may be correlated to shapes of the diamond crystallites shown in the SEM image (b) [22].

Effects of electrical conductivity: Even if the surface of a diamond film has a low surface electron affinity, it is difficult to observe continuous low-field electron emission, since the diamond film may not have enough conduction electrons to be supplied to the emitting surface. In a photo cathode, electrons emitted into vacuum are first promoted from a valence band to a conduction band by photon excitation. For a cold cathode field-emitter, however, conduction electrons will not be available for diamond film due to its low electrical conductivity. The ideal situation is to have an n-type diamond that may have electrical conductivity as high as that of *n*-type silicon. However, this so far has not been achieved, due to the difficulty in doping diamond. The reason for this is believed to be due to the very special crystalline structure of

diamond in which all the carbon atoms form very stable structures with very small lattice constants.

1.4.2.3 Field Electron Emission Mechanism

There is not yet a widely accepted model for explaining the phenomenon of field emission from diamond films. A number of models proposed so far have some degree of similarity, which is illustrated in Figure 1-6 [24]. Graphite inclusions are assumed to exist in grain boundaries (Figure 1-6a) and can act as conduction channels for electron transport, as shown in Figure 1-6b [25]. With the application of an electric field the electrons may be injected into the conduction band of the diamond film through the conduction channels, from which situation they may then be emitted. Some other researchers have also found that the electrons are emitted from diamond grains rather than grain boundary areas [22].

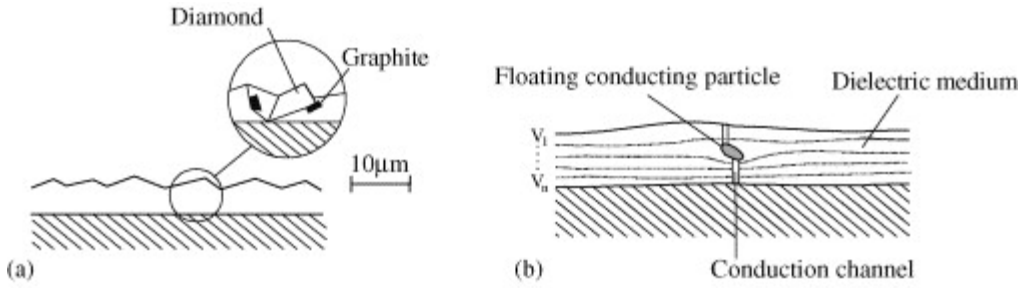

Figure 1-6: (a) The microscopic details of the CVD film in favour of low-field emission, which was assumed to have graphite inclusions along the grain boundaries. (b) Illustrating how a graphite inclusion may act as conduction channels [24, 25].

1.4.3 Fabrication of Diamond Field Emitters

Diamond films have potential applications in field electron emission devices. Currently, a significant technical challenge is to fabricate diamond field emitters. There have been a number of successful attempts in this aspect [26, 27]. An easy way to produce diamond emitters is to coat either Spindt field emission arrays (FEAs) or silicon emitter arrays with a thin film of diamond. However, eventually large-area

arrays with emitters completely made from diamond and related materials will have to be realized.

The most compelling work on diamond-emitter array fabrication was reported by Kang *et al.* [28]. They have developed techniques for producing arrays of diamond microtips with extractor gates, as shown in Figure 1-7. The technique developed by Kang *et al.* is based on the use of an array of silicon mold. In their initial work, arrays of diamond microtips without extractor gates were produced (Figure 1-7a). A silicon (1 1 1) wafer was used as substrate, and the array of molds were first created by isotropic etching. The diamond film was then deposited onto the silicon substrate. Deposition conditions were adjusted so that the diamond microtip contained a significant amount of graphite components as detected by Raman spectroscopy. It was proposed that the possible formation of diamond–graphite interlayer structure may be responsible for the low-field emission. Later, the above technique was developed to produce a 2 × 2 array of diamond microtips with extractor gates (Figure 1-7b).

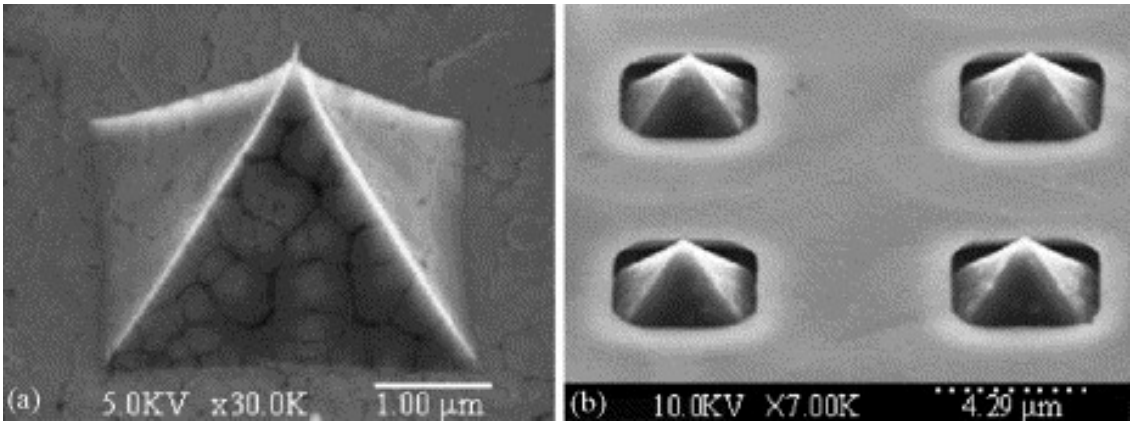

Figure 1-7: SEM images of a single diamond nanotip (a) and the array of the gated diamond nanotips (b) [28].

1.5 State of the Problem

In recent years, much effort has been put into the field electron emission of diamond and related films. Although there are still no satisfactory theories that can

explain all the experimental results, experimental observations suggest the following basic features:

- Surface morphologies have important influence on the field electron emission property. The sharp structures such as tips and ultra-tips can improve the field electron emission properties greatly. It can reduce the turn-on electric field and enhance the field electron emission. However, it is still unclear about the influence of grain morphologies on the field electron emission properties of diamond films. At the same time, it still remains a problem on how to synthesize diamond films with various tip structures.
- The sp^2 phase plays an important role in the field electron emission of diamond films. Many researchers concluded that the formation of small sp^2 regions embedded in the sp^3 matrix will lead to low turn-on fields [5-8]. In order to explain the field electron emission experimental results of diamond and related materials, V.D. Frolov *et al.* proposed a physical model of the field electron emission process, which has been called the conduction channel model [29]. The model suggests the existence of narrow conduction channels between insulating diamond grains. Electrons are transferred from a conductive channel into the vacuum through a specific region which is positioned at a boundary between the conducting and insulating phases of the film materials. Large grain boundary areas, which can be realized by reducing the grain size, will increase the number of conduction channels. Another way to increase the conduction channels is to increase the sp^2 phase concentration in the diamond films directly. However, the knowledge on how to adjust the sp^2 phase concentration in diamond films is still limited.
- Single cold cathode material normally has only one, sometimes several, but rarely all properties beneficial for field electron emission. Diamond and graphite are two typical carbon-based materials. They have their own advantages and disadvantages. It is important to combine diamond and graphite for the fabrication of field electron emitters.

1.6 Objective of This Work

The objectives of this work are as follows:

- Selective and controlled growth of diamond films with specific morphologies for field electron emission applications.

The selective and controlled growth of diamond films is necessary for the fabrication of diamond emitters with required morphology and composition. Due to its high mechanical strength and chemical stability, Si-based microfabrication methods are difficult to apply to diamond films. One attempted idea has been to make Si components to near-net shape and then coat a layer of diamond films on the surface. Much effort has been put into the manufacture of Si microtip arrays coated with diamond films. However, this method does not provide a satisfactory solution, since the mechanical properties of such devices are still dominated by the Si core. Combining the Si-based microfabrication technology with selective and controlled growth technique offers a solution to solve this problem. In general, synthesis of diamond thin film requires a nucleation layer, which is usually achieved by exposing the substrate to a suspension of fine diamond particles. Using photolithography, photoresist is patterned on the substrate to prevent seeding to a selected area, which realizes the so-called selective deposition.

- Enhancement of field electron emission properties by synthesizing diamond films with high sp^2 phase concentrations.

The main problem for the field electron emission of diamond films is low electrical conductivity, which limits the electron transport and thus the emission current. As a material with wide band gap, the *n*-type doping of diamond films has not yet been effectively realized. However, the conduction channels between the grain boundaries can provide paths for electron transport. The number of conduction channels depends on the grain boundary areas and sp^2 phase concentrations. Although reducing grain sizes can increase the grain boundary areas, it is much more efficient to adjust the sp^2 phase concentration in the diamond films by controlling the deposition conditions.

- Fabrication of diamond field emitters with desirable field electron emission properties.

In general, single carbon-based material cannot have all the properties necessary for field electron emission with high performance. But each of them has one or several special properties that can enhance field electron emission. Based on this point, a field emitter with better field electron emission property can be fabricated by combining several carbon-based materials.

- Study of field electron emission mechanism.

It can be found from the Fowler-Nordheim equation that there are two ways to enhance the field electron emission property of emitters. One is to enlarge the field enhancement factor. As the field enhancement factor is determined mainly by the surface morphology of emitters, it is necessary to investigate systematically the influence of surface morphology on the field electron emission property. The other method is to increase the effective emission areas of field emitters. Until now, increasing the effective emission areas remained a major problem. In this PhD work, the field electron emission properties of diamond films with different morphologies and compositions have been compared.

1.7 Major Results of This Project

Some major results of this project are as follows:

- Surface morphology has important influence on the field electron emission properties of diamond films. Firstly, by reducing the grain sizes, the field electron emission properties of diamond films have been enhanced due to the increase of effective emission areas. Secondly, diamond films with randomly oriented grains exhibit larger emission current than those with well-oriented grains. The enhancement of the field electron emission property is mainly due to the larger effective emission area of randomly oriented diamond films. Thirdly, for the diamond films with well-oriented grains, the field electron emission properties were enhanced with the decrease of top area of grains. The increase in the field enhancement factor is the main reason for field electron emission enhancement in this case. In addition, diamond nanocones with large aspect ratio have been synthesized successfully. Superior field electron emission properties were observed for diamond nanocones due to very large field enhancement factors.

- The effective emission areas of diamond films can be increased by increasing the sp^2 phase concentration, which can provide more conduction channels for the electron emission. For diamond films synthesized using H_2 and CH_4, this can be realized by increasing the CH_4 concentration during deposition. For diamond films synthesized using graphite etching, the sp^2 phase concentration can be increased by decreasing the H_2 flow rate during deposition.
- The nonlinear Fowler-Nordheim plot was observed for graphitic nanocone films. A new mechanism, the nonuniform field enhancement factor, was proposed to explain this phenomenon.

1.8 Organization of the Thesis

In this chapter the discussion was focused on the importance of field electron emitters and their applications. A brief introduction to the qualities that make diamonds excellent field emitters was given along with the possible applications that they may have.

In Chapter 2 a detailed discussion of the electron emission will be presented. Several field electron emission mechanisms, including thermionic emission, photoelectric emission, field electron emission from metallic emitters, and field ionization, will be discussed.

Chapter 3 will cover the detailed experimental procedures and experimental setups that were used. It will also cover growth processes for different samples used in the experiments.

Chapters 4, 5, and 6 will present the main results. In Chapter 4, field electron emission characteristics of diamond films with different surface morphologies are studied, including microcrystalline diamond films with different grain morphologies, nanostructured carbon-based films, and diamond composite films. In Chapter 5, effects of sp^2 phase concentration on the field electron emission characteristics of diamond thin films are investigated. In Chapter 6, nonlinear Fowler-Nordheim plots of the field electron emission from graphitic nanocones are presented and discussed. The nonlinearity is attributed to the influence of nonuniform field enhancement factors. Chapter 7 concludes the thesis.

Chapter 2

Field Electron Emission Theory

In this chapter various mechanisms of electron emission from solids are presented.

2.1 Work Function of Solids

Inside a metal, the behavior of electrons can be approximately described by the free electron gas model. The electrons move freely inside the metal. Electrons are unable to come out of the metal surface freely because there is a potential barrier at the surface. This surface barrier is called the work function. It represents the difference in energy between the highest normally occupied electron energy level inside the metal and the state of an electron at rest outside the surface. The phenomenon of electron emission occurs when electrons overcome this surface barrier and come outside of the surface.

The work function plays a decisive role in all electron emission phenomena. The work function of a metal depends both on its bulk properties and on the characteristics of its surface. The energy difference involved in the definition of the work function can be divided into two parts: the energy of the highest filled level in the metal relative to the mean electrostatic potential inside, and the difference between this interior potential and the potential outside. The former has nothing to do with conditions at the surface and thus involves only the bulk properties of the metal. The latter involves the surface and is influenced by the surface structure.

Before the 1960's, the electron theory of metals was primarily concerned with properties of the metal interior. These bulk properties are of fundamental interest. The theory of bulk metal properties gives a quantitatively accurate description of wide classes of metals. However, the theory of metal surfaces lagged far behind at the time. This was primarily due to the additional difficulties introduced by the rapid decrease of electron density near the surface.

In metals, the positive charges are fixed in space, and they cannot move freely. However, electrons can move freely. So the positive charge density is constant up to the surface and zero beyond the surface. It is a step function. The electron density equals the positive charge density in the deep interior, but falls gradually rather than suddenly to zero as the surface is crossed. The result is a double layer, with an excess of negative charge just outside the surface and an excess of positive charge just inside.

This double layer produces an electrostatic potential that results in a positive energy barrier that makes it difficult for electrons inside to escape from the surface. However, the work function does not only come from this double layer 'dipole' potential. Outside the surface, electrons experience the classical image potential [30, 31]. In the intermediate region the potential connects smoothly across the surface [30, 31]. Bardeen made an important contribution to the theory of metal surfaces in 1936 by performing an approximately self-consistent calculation for the metal sodium [30]. The wave functions of the conducting electrons of the sodium crystal are, except in the immediate vicinity of the ions, very nearly the same as those of perfectly free electrons [30]. By taking the surface dipole layer potential energy into the free electron gas model, Bardeen calculated the work function of sodium to be about 2.35 eV, which agrees well with the experimental value of 2.46 eV. However, after Bardeen's work, there was almost no progress in the theory of metal surfaces for thirty years. During the middle of the 1960's the development of the density functional theory by Kohn *et al.* greatly advanced the treatment of electron systems, especially in inhomogeneous electron gas system [32-35]. Based on this theory, Lang and Kohn [36] developed a self-consistent scheme for calculating the work function for metals, taking into consideration the surface double layer dipole potential and the image potential. They developed their method based on a model of metals in which the positive ionic charges

inside the metal are replaced by a uniform charge background of positive charge density. Their results from the calculated work function quantitatively agreed with the experimental results of many metals. This method laid down the foundation of calculating work functions and has been improved and modified [37].

2.2 Electron Emission

Electron emission is the process of extracting electrons from the surface of a solid. This phenomenon is characterized by getting electrons to overcome the natural energy barrier existing at the surface and emit out. Electrons can be removed from solids by:

1. Providing electrons with sufficient kinetic energy to surmount the potential barrier at the surface of the solid, or
2. Reducing the height of or thinning the barrier, so that the electrons can penetrate the barrier and escape by virtue of their wave characteristics: tunneling.

Sufficient kinetic energy may be given to electrons by application of heat, resulting in thermionic emission, or by absorption of light quanta of sufficient energy to cause photoelectric emission. Reduction and thinning of the barrier could be brought about by application of high electric fields to the surface, leading to field electron emission. Finally, electron emission from solids can also be caused by the incidence of energetic particles, such as electrons, positive ions, and neutral atoms.

Figure 2-1 is a schematic of the electron energy versus position inside a metal. It is convenient to consider a metal as a box within which the potential energy of an electron is lower than that of an electron outside by an amount δ, as illustrated. Here, δ is the energy difference between the bottom of the metal conduction band and the vacuum level. In the box, at absolute zero temperature, the electrons have kinetic energies which are distributed up to the Fermi level E_f. The distance between the Fermi level and the vacuum potential level is the work function φ, which is the work necessary to remove an electron from the metal.

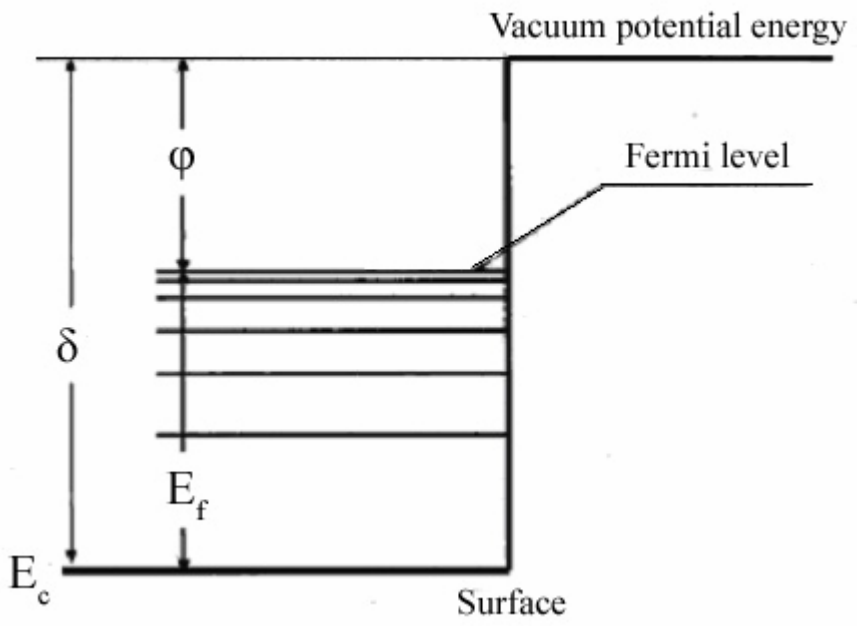

Figure 2-1: Schematic of the electron energy in a metal.

2.3 Thermionic Emission

Thermionic emission from metal surfaces is caused by the transfer of energy from vibrations of the crystal lattice to the free electrons, a process that is enhanced at elevated temperatures. A necessary but not sufficient condition for emission is that electron energy should be greater than the height of the potential barrier.

At zero temperature the electron distribution function has the form of a step function:

$$n(E) = \begin{cases} 1 & E<E_f \\ 0 & E>E_f \end{cases}. \tag{2-1}$$

At a finite temperature, the step distribution function becomes smoother as electrons can be excited to occupy energy levels higher than the Fermi level. The energy distribution function is given by the Fermi-Dirac distribution function

$$n(E) = \frac{1}{\exp\left(\frac{E-E_f}{kT}\right)+1}, \tag{2-2}$$

where $n(E)$ is the probability density of occupation (average number of electrons per unit energy per unit volume) of a state with energy E, E_f is the Fermi level

mentioned above and illustrated in Figure 2-1, $k = 1.38 \times 10^{-23}$ J/K is the Boltzmann constant, and T is the absolute temperature. It can be seen from Equation 2-2 that the probability of occupation increases when the temperature increases for the same energy difference $E - E_f$, and decreases when the energy difference $E - E_f$ increases at the same temperature. It is convenient to assume that without the presence of an external electric field (i.e., the vacuum level remains flat at the surface) only electrons with energy levels higher than the vacuum level are able to escape over the barrier into the vacuum. This is understandable because the tunneling probability of an electron through an infinitely wide barrier is nearly zero.

When the temperature T is very low, the density of electrons that have energy higher than the vacuum level is extremely small, and therefore the electron emission from the material is undetectable. When the material is heated, more electrons will be thermally excited to occupy energy levels higher than the vacuum level. Thus thermionic electron emission occurs.

Richardson and Dushman [38, 39] investigated electron emission from metals at high temperatures and developed a thermodynamic theory from which they related the current density j to the absolute temperature T of the metal. The thermionic current density J from a metal surface with a work function φ and at a temperature T can be given by the following equation:

$$j = \int_{E \geq E_{\min}} en(E)v(E)dE\,, \tag{2-3}$$

where e is the magnitude of electron charge, E is the electron energy, and $v(E)$ is the velocity distribution. $n(E)dE$ is the density of electrons, in the energy range between E and $E + dE$, per unit volume, which can be written as:

$$n(E)dE = \frac{8\pi m^3}{\hbar^3} \frac{v^2 dv}{1 + \exp(\frac{E - e\varphi}{kT})}\,. \tag{2-4}$$

By integrating Equation 2-3 for energies sufficient to escape the potential barrier, i.e. $E \geq E_{\min} = e\varphi$, the Richardson-Dushman equation is obtained:

$$j_R(\phi,T) = AT^2 \exp\left(-\frac{e\varphi}{kT}\right), \tag{2-5}$$

$$A = \frac{emk^2}{2\pi^2\hbar^3} \approx 120\ (\mathrm{A\cdot cm^{-2}\cdot K^{-2}}), \tag{2-6}$$

where $\hbar = h/2\pi$, h being Planck's constant.

Nordheim [40] obtained a similar formula, including the possibility that an electron can be reflected back into the metal after escaping from the metal:

$$j = A(1-r)T^2 \exp\left(-\frac{e\varphi}{kT}\right), \tag{2-7}$$

where r is the probability that electrons which have sufficient energy to get over the barrier are reflected back.

2.4 Space Charge Limited Current

Space charge is a localized region of excess negative charge that occurs near a metal surface emitting electrons. The space charge limited current was discovered by Clement Dexter Child and Irving Langmuir. The description of this current was called the Child-Langmuir Law, which states that the space charge-limited current (SCLC) in a plane-parallel diode varies directly as the three-half power of the anode voltage V_a and inversely as the square of the distance d separating the cathode and the anode. Thus,

$$j = \frac{4\varepsilon_0}{9}\sqrt{\frac{2e}{m}}\frac{V_a^{\frac{3}{2}}}{d^2}, \tag{2-8}$$

where j is the current density, ε_0 the permittivity of free space, e the magnitude of electron charge, and m the free electron mass [41].

2.5 Schottky Emission

Under the action of applied electric fields the work function is reduced to:

$$\varphi' = \varphi - e^{\frac{3}{2}}F^{\frac{1}{2}}, \tag{2-9}$$

where F is the electric field. This is also called the 'Schottky Lowering'. Thus if j_0 is the thermionic emission current density from zero electric field at a temperature T, i.e., $j_0 = AT^2 \exp(-e\varphi / kT)$, then j_F, the emission current density for an electric field F, is

$$j_F = j_0 \exp\left(\frac{e^{\frac{3}{2}} F^{\frac{1}{2}}}{kT} \right). \tag{2-10}$$

This relation was derived by Schottky and has been shown to be valid over a wide range of temperature and for fields up to 10^6 V/cm [42]. Under this situation, electrons do not have to surmount the potential barrier of height φ, but can by virtue of their wave properties tunnel through the potential barrier. This is known as the tunneling effect and is the onset of the field electron emission which will be discussed in detail in the following section.

The origin of Schottky Lowering comes from the image potential that an electron experiences near a conducting surface. More details about the image potential and its effects on field electron emission will be discussed in the following section within the framework of the theory of field electron emission.

2.6 Field Electron Emission

Field electron emission from a solid can be characterized as having two continuous processes:

1. electron flux to the surface of the emitters, determined and limited by the electron supply, and
2. electron tunneling through the surface potential barrier, determined by the tunneling transmission coefficient

After the electrons come out of the solid's surface and go into the vacuum, they could be accelerated, focused, bunched or manipulated, based on the application of interest.

The field electron emission process is treated by considering a one-dimensional potential barrier. This potential barrier was originally proposed by Schottky and was used by Nordheim [40] in his modification of the original Fowler-Nordheim theory.

At room temperature, the potential barrier at the surface of the metal has an infinite width, thus preventing electrons from coming out of the surface. When an external electrical field is applied, the vacuum level is bent and the barrier width is no longer infinite. Field electron emission occurs when the vacuum level bending is so much that the barrier width is small enough for the electrons inside the metal to tunnel through the barrier.

The following field electron emission theory is derived for a metal. However, it can be also applied to semiconductors such as diamond. The only difference is in the work function. For a metal, the work function is the energy difference between vacuum level and Fermi level. For semiconductor, the work function has different definition. If electrons are emitted from the conduction band, the work function is the energy difference between vacuum level and conduction band minimum. For electron emitted from the valence band, the work function is the energy difference between vacuum level and valence band maximum. The field electron emission from valence band of silicon has been experimentally observed and it can fit the field electron emission theory (F-N theory) very well [21].

2.6.1 An Argument from the Uncertainty Principle

Tunneling is a quantum mechanical phenomenon. From the Heisenberg uncertainty principle, the momentum of an electron within an uncertainty implies a corresponding uncertainty Δx in its position, given by

$$\Delta p \cdot \Delta x \cong \hbar / 2 , \tag{2-11}$$

where $\hbar = h / 2\pi$, h being Planck's constant. Considering electrons near the Fermi level, the pertinent uncertainty in momentum is $(2m\varphi)^{\frac{1}{2}}$ [42]. The corresponding uncertainty in position, according to Equation 2-11, is

$$\Delta x \cong \hbar / 2(2m\varphi)^{\frac{1}{2}} , \tag{2-12}$$

where the presence of an external electric field, the barrier width is given by

$$x = \varphi / Fe . \tag{2-13}$$

If the uncertainty in position is of the order of the barrier width (Equation 2-13) there will be a good chance of finding an electron on either side of it. This can be expressed by requiring that

$$\varphi / Fe \cong \hbar / 2(2m\varphi)^{\frac{1}{2}}, \tag{2-14}$$

or that

$$2\left(\frac{2m}{\hbar^2}\right)^{\frac{1}{2}} \frac{\varphi^{\frac{3}{2}}}{Fe} \approx 1 . \tag{2-15}$$

So the field required to extract electrons out from the metal is estimated as

$$F \approx \frac{2(2m)^{\frac{1}{2}} \varphi^{\frac{3}{2}}}{e\hbar} . \tag{2-16}$$

A direct calculation of Equation 2-16 gives rise to an electric field of 8.34×10^8 V/cm, assuming $\varphi = 4.05$ eV for the case of the conduction band electron of silicon. This electric field value is approximately 40 times larger than the electric field actually needed for field electron emission.

2.6.2 Modification of the Surface Potential Barrier

2.6.2.1 Image Potential

An electron outside a conducting plane experiences an image charge force, because the electron induces a positive charge on the surface of the conducting plane. As it moves around, the electron experiences a potential created by its image charge. Figure 2-2 shows the schematic of the image charge.

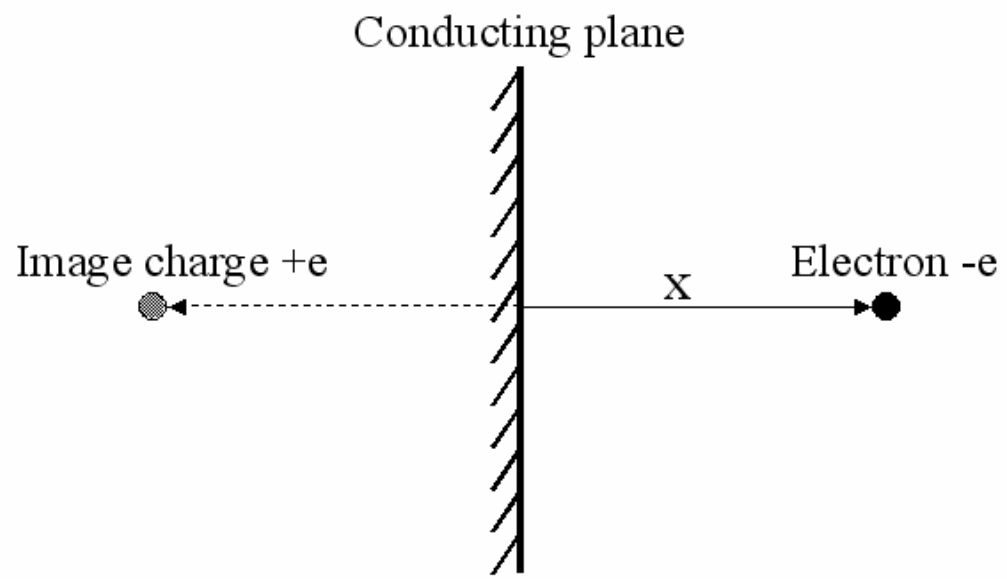

Figure 2-2: Schematic of the image charge of an electron sitting in front of a conducting plane. The image charge has the opposite sign of the electron, and the distance between the image charge and the plane is equal to the distance between the electron and the plane.

The electrostatic force the electron experiences in front of a conducting plane is equal to the electrostatic force between the electron and the image charge. Taking the positive x direction to be the direction pointing from the plane to the electron, the electric force the electron experiences is equal to

$$f = \frac{-e^2}{4x^2}. \tag{2-17}$$

The energy E of an electron transferred from infinity to a distance x from the surface is given by

$$E(x) = \int_x^\infty f \cdot dx = -\frac{e^2}{4x}. \tag{2-18}$$

In the presence of a constant electric field F, the total energy potential $V(x)$, in the unit of eV, for an electron outside a metal surface is

$$V(x) = \varphi - \frac{e^2}{4x} - eFx. \tag{2-19}$$

2.6.2.2 Schottky Lowering

One of the direct consequences of the image potential is the so-called Schottky Lowering effect [40]. Figure 2-3 shows a schematic of the effect. Figure 2-3(a) shows

the potential energy without the image potential, nor the external electric field. The barrier height is the work function φ, and Figure 2-3(b) shows the potential energy with an external electric field, but without an image potential. The barrier height is also φ, but narrower. Figure 2-3(c) shows the potential energy with an image potential, but without the external electric field. The steep potential discontinuity at the surface is rounded, but the barrier height remains at φ. Figure 2-3(d) shows the potential energy with both image potential and external electric field. In this case, the potential barrier at the surface is actually decreased and is narrower. This effect is called Schottky Lowering. A simple calculation can give the lowering to be

$$\Delta\varphi = -\sqrt{e^3 F} \tag{2-20}$$

at the position

$$x = \frac{1}{2}\sqrt{\frac{e}{F}}, \tag{2-21}$$

where the potential finds its maximum as shown in Figure 2-3(d).

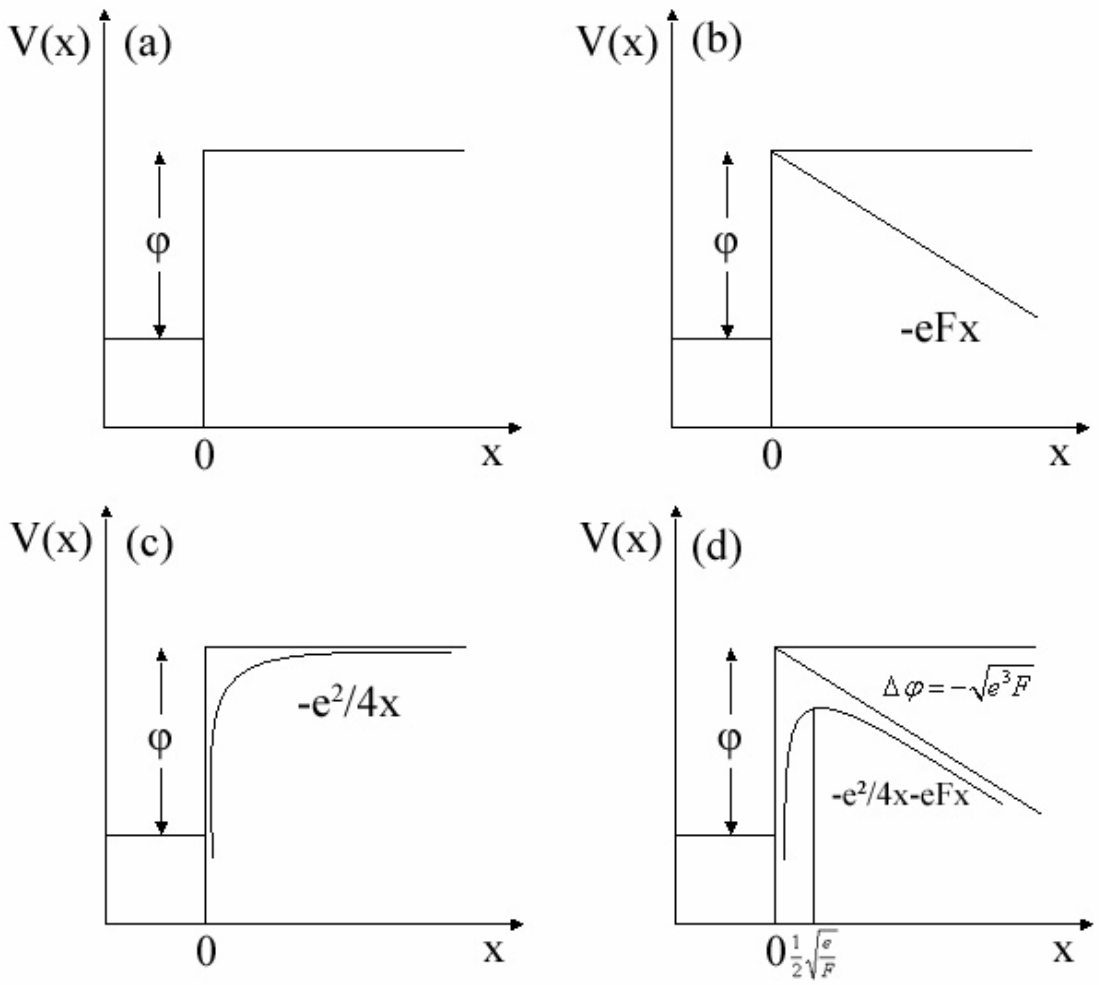

Figure 2-3: Schematic of Schottky Lowering: (a) without image potential and external field, (b) without image potential but with external field, (c) with image potential but without external field, and (d) with both image potential and external field.

Schottky lowering is the source of the so-called Schottky emission briefly described in section 2.5. When the external electric field is small, the work function of the metal surface is effectively lowered, resulting in Equation 2-9. The net effect is the increased thermionic electron emission, resulting in Equation 2-10. In the presence of a strong external electric field, field electron emission predominates.

2.6.2.3 Formulation of the Surface Potential Barrier

Figure 2-4 illustrates the profile of the potential energy an electron experiences in the case of field electron emission. Compared with Figure 2-1, the zero energy point in this diagram is set at the energy level in vacuum and $\zeta = -\phi$ corresponds to the Fermi level. Based on the discussion above, there are three contributions to the surface potential barrier:

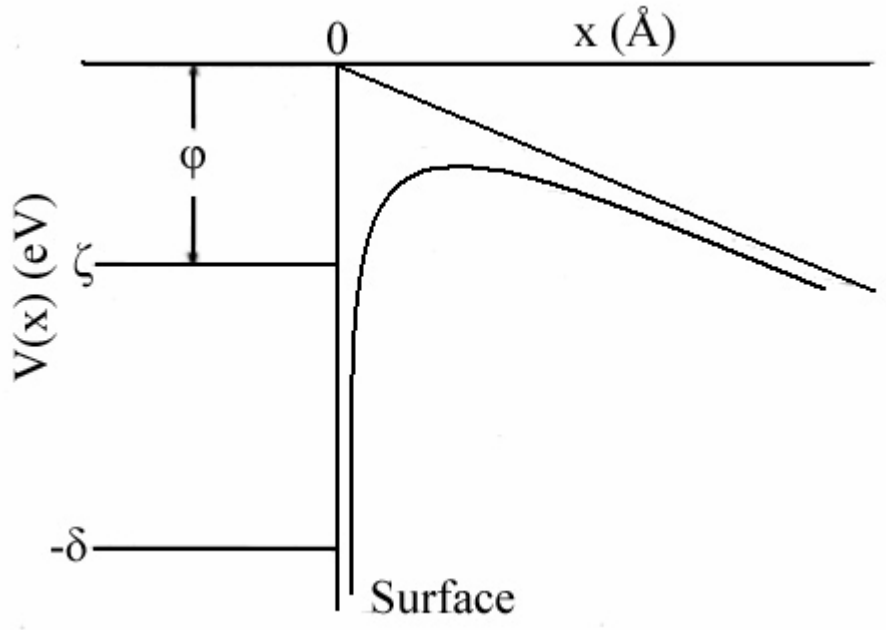

Figure 2-4: Schematic of the potential barrier near a metal surface in the presence of an external electric field.

1. Within the metal the potential energy has some constant value $-\delta$ relative to zero (here the zero point is the vacuum energy level). This energy is lower than the Fermi level in metals.
2. An external electric field F is applied to narrow the potential barrier, allowing the electrons to tunnel out of the metal. The origin will be chosen to be on the metal surface and the positive x-axis perpendicular to the surface and out of the metal. This field gives a contribution of $-eFx$ to the potential barrier. It is presumed that the free charges cause this field to be neutralized within the

metal and so it applies only outside, i.e., for metals, there is no field penetration. The zero point is chosen so that this contribution to the potential is zero when the applied electric field is zero.

3. The image potential is chosen to be zero when the electron is far from the metal. This energy applies only to electrons outside the metal.

The sum of the above three contributions gives

$$V(x) = \begin{cases} -\delta, & \text{for } x<0 \\ -eFx - e^2/4x, & \text{for } x>0 \end{cases}, \tag{2-22}$$

for the effective potential barrier.

The main features of field electron emission can be understood from the shape of the potential outside the metal. The maximum value of the potential is found by differentiation to be at the point

$$x_0 = \frac{1}{2}\sqrt{\frac{e}{F}}, \tag{2-23}$$

and the corresponding maximum value of $V(x)$ is

$$V_{\max} = -\sqrt{e^3 F}. \tag{2-24}$$

Under practical conditions this maximum remains above the Fermi energy. It is observed that Equation 2-24 is exactly equal to the Schottky lowering of the work function under an external electric field, as described by Equation 2-9.

2.6.3 Fowler-Nordheim Tunneling Theory

In their theory of field electron emission, Fowler and Nordheim assumed: (i) the free electron gas model for the conduction electrons, and (ii) the effective potential model of the metal presented in Equation 2-22, and made an additional physical assumption that the electrons inside the metal remain essentially at equilibrium. Under this set of assumptions, the current of electrons is found by integrating over all electron energies, the equilibrium flux of electrons incident on the surface times the probability that an electron penetrates the barrier.

The total energy ε of an electron under the surface energy potential *V(x)* is

$$\varepsilon = \frac{p_x^2}{2m} + \frac{p_y^2}{2m} + \frac{p_z^2}{2m} + V(x), \tag{2-25}$$

where p_x, p_y, and p_z are the momentum components of the electron in x, y and z directions.

Then this integral can conveniently be written in terms of the x-part of the energy W, defined by

$$W = \varepsilon - \frac{p_y^2}{2m} - \frac{p_z^2}{2m} = \frac{p_x^2}{2m} + V(x). \tag{2-26}$$

All energies will be measured from the same reference as the effective potential $V(x)$. Then, if $N(W)dW$ is the number of electrons with the x-part of their energy within dW incident on the surface per second per unit area, and $D(W)$ is the probability of transmission through the barrier, the product $P(W)dW$ gives the number of electrons within dW that emit from the metal per second per unit area

$$P(W)dW = D(W)N(W)dW, \tag{2-27}$$

and j, the electric current per unit area is

$$j = e\int_{-\delta}^{\infty} P(W)dW, \tag{2-28}$$

where e is the magnitude of an electron charge. The function $N(W)$ is called the supply function and $D(W)$ is called the transmission coefficient.

The supply function can be calculated to be

$$N(W) = \frac{4\pi mkT}{h^3} \ln\left(1 + \exp\left(-\frac{W-\zeta}{kT}\right)\right), \tag{2-29}$$

where $\zeta = -\phi$ corresponds to the Fermi level as mentioned earlier.

The transmission coefficient is calculated using the WKB approximation [43]:

$$D(W) = \exp\left(-\frac{4\sqrt{2m|W|^3}}{3heF} v(y)\right), \tag{2-30}$$

where

$$v(y) = 2^{-\frac{1}{2}} \sqrt{1+\sqrt{1-y^2}}\, E(k) - (1-\sqrt{1-y^2})K(k), \tag{2-31}$$

$$K(k)=\int_0^{\frac{\pi}{2}}\frac{d\delta}{\sqrt{1-k^2\sin^2\varphi}}, \tag{2-32}$$

$$E(k)=\int\sqrt{1-k^2\sin^2\varphi}\,d\varphi, \tag{2-33}$$

$$k^2=\frac{2\sqrt{1-y^2}}{1+\sqrt{1-y^2}}, \tag{2-34}$$

$$y=\frac{\sqrt{e^3F}}{|W|}. \tag{2-35}$$

The number of electrons within dW that emit from the metal per second per unit area is found by combining Equation 2-29 and Equation 2-30 according to the Equation 2-27:

$$P(W)dW=\frac{4\pi mkT}{h^3}\exp\left(-\frac{4\sqrt{2m|W|^3}}{3\hbar eF}v\left(\frac{\sqrt{e^3F}}{W}\right)\right)\ln\left(1+\exp\left(-\frac{W-\zeta}{kT}\right)\right)dW. \tag{2-36}$$

It is difficult to obtain an analytical expression of integral 2-28 with the integrand $P(W)$ having the form of Equation 2-36. Approximations have been made to obtain results of interest [44]. Dolan and Dyke studied Equation 2-36 numerically and calculated $P(W)$ for various temperatures and field strengths [45]. In their calculation, the work function was assumed to be $\varphi=4.5$ eV, the value for clean tungsten.

It is observed that at a low temperature, the energy distribution of the emitted electron $P(W)$ peaks near the Fermi level over the range of electric fields at which field electron emission occurs. This means that at a low temperature the field emitted electrons have energies approximately around the Fermi level $W=\zeta$. This result can be understood in the following way. At a low temperature, there are few electrons above the Fermi level. Electrons that are capable of participating in field electron emission almost all come from below the Fermi level. The transmission coefficient $D(W,F)$ is a maximum when $W=\zeta$. Because, at low temperature, the electron supply function $N(W)$ is a slowly varying function of W and the transmission coefficient $D(W,F)$ is a sensitive function of W (due to the exponential dependence

on W), the product of these two functions always peaks near the Fermi level and decreases quite quickly below the Fermi level.

When the temperature is very high, there are an appreciable number of electrons above the Fermi level. At the same time, the transmission coefficient for these electrons is much larger than that of electrons near the Fermi level. In this situation the energy distribution of emitted electrons could no longer peak near the Fermi level.

In Fowler-Nordheim theory, the low temperature limit is considered. It is permissible then to approximate the exponent in the transmission coefficient by the first two terms in a power series expansion at the Fermi level $W = \zeta$.

$$-\frac{4\sqrt{2m|W|^3}}{3\hbar eF} v\left(\frac{\sqrt{e^3F}}{|W|}\right) \approx -c + \frac{W-\zeta}{d}, \tag{2-37}$$

where

$$c = \frac{4\sqrt{2m\varphi^3}}{3\hbar eF} v\left(\frac{\sqrt{e^3F}}{\varphi}\right), \tag{2-38}$$

$$d = \frac{\hbar eF}{2\sqrt{2m\varphi}\ t\left(\frac{\sqrt{e^3F}}{\varphi}\right)}, \tag{2-39}$$

$$t(y) = v(y) - \frac{2}{3} y \frac{dv(y)}{dy}. \tag{2-40}$$

The function $t(y)$ is a slowly varying function, ranging only between 1.00 and 1.11. If numerical values of m, e, h, are inserted here, and if φ is expressed in eV and F is expressed in V/cm, then c and d are given by

$$c = \frac{6.83\times10^7 \varphi^{\frac{3}{2}}}{F} v\left(3.79\times10^{-4}\frac{F^{\frac{1}{2}}}{\varphi}\right), \tag{2-41}$$

$$d = \frac{9.73\times10^{-9} F}{\varphi^{\frac{1}{2}}\ t\left(3.79\times10^{-4}\frac{F^{\frac{1}{2}}}{\varphi}\right)}. \tag{2-42}$$

For low enough temperature, it is seen that

$$kT\ln\left(1+\exp\left(-\frac{W-\zeta}{kT}\right)\right)=\begin{cases}0 & \text{when } W>\zeta\\ \zeta-W & \text{when } W<\zeta\end{cases}. \tag{2-43}$$

If Equation 2-37 and Equation 2-43 are substituted into Equation 2-36, the result is

$$P(W)=\begin{cases}0 & \text{when } W>\zeta\\ \dfrac{4\pi m}{h^3}(\zeta-W)\exp\left(-c+\dfrac{W-\zeta}{d}\right) & \text{when } W<\zeta\end{cases}, \tag{2-44}$$

and this is the low temperature limit of the distribution of the emitted electrons. By differentiation, it can be found that the peak of $P(W)$ occurs at the energy $W=\zeta-d$ and has the value

$$P_{\max}=\frac{4\pi md}{h^3}e^{-(c+1)}. \tag{2-45}$$

The total electric current is found by integrating the distribution given by Equation 2-44 over all energies according to Equation 2-28. Normally the lowest energy $-\delta$ is far below the Fermi energy ζ so the lower limit of the integral may be taken at $-\infty$. The results are as follows:

$$j=e\int_{-\infty}^{\zeta}\frac{4\pi m}{h^3}e^{-c+\frac{W-\zeta}{d}}(\zeta-W)dW=\frac{4\pi med^2}{h^3}e^{-c} \tag{2-46}$$

Substituting 2-38 and 2-39 into the above equation, the current density is finally obtained:

$$j=\frac{e^3F^2}{8\pi h\varphi\, t^2\left(\dfrac{\sqrt{e^3F}}{\varphi}\right)}\exp\left(-\frac{4\sqrt{2m}\varphi^{\frac{3}{2}}}{3\hbar eF}v\left(\frac{\sqrt{e^3F}}{\varphi}\right)\right). \tag{2-47}$$

If φ in eV and F in V/cm are inserted into Equation 2-47 the result is

$$j=\frac{1.54\times10^{-6}F^2}{\varphi\, t^2\left(3.79\times10^{-4}\dfrac{F^{\frac{1}{2}}}{\varphi}\right)}\exp\left(-6.87\times10^{7}\frac{\varphi^{\frac{3}{2}}}{F}v\left(3.79\times10^{-4}\frac{F^{\frac{1}{2}}}{\varphi}\right)\right)\ \mathrm{A\cdot cm^{-2}}. \tag{2-48}$$

Equations 2-47 and 2-48 are the Fowler-Nordheim field emission formulae. Some numerical calculations of the current density for various fields and work functions are performed using Equation 2-48 but with t set equal to unity [46]. This simplification is often made because t^{-2} varies only between 1.00 and 0.81, contributing between 0 and –0.99 to $10\ln(j)$.

Based on the above observations of the properties of the functions $t^2(y)$ and $v(y)$, Spindt *et al.* [47] proposed a close approximation of these two functions:

$$t^2(y) = 1.1, \tag{2-49}$$

$$v(y) = 0.95 - y^2, \tag{2-50}$$

where

$$y = 3.79\times10^{-4}\frac{F^{\frac{1}{2}}}{\varphi}. \tag{2-51}$$

2.6.4 Geometric Field Enhancement

In practice, there are two basic shapes of field emission devices, planar and pointed. In order to produce electric fields of sufficient magnitude to extract measurable emission current from cold cathode materials, it is usually necessary to take advantage of geometrical field enhancement. The use of needle shaped emitters allows for substantial field enhancement at the apex of the tip. The use of planar emitters, with very small tip-to-anode spacing to achieve high fields, has been demonstrated with little success. Planar emitters suffer from several inherent problems: they are not designed to offer large geometric field enhancement and are thus subject to extremely irregular emission areas, for example due to protrusions; and the relatively large areas over which emission can occur make determination of variables such as work function, surface/interface roughness, and adsorbates more difficult. Furthermore, planar emitters are in fact not perfectly flat; there exist natural variations in surface roughness, which affect emission and complicate interpretation of emission data. Pointy emitters, whose geometry ensures the maximum field at the tip apex, are preferred because local electric fields can be determined more accurately, and emission is more predictable. The local electric field F is enhanced by:

$$F = \beta E, \tag{2-52}$$

where β is the field enhancement factor depending on the exact geometry of the system, and E is the applied electric field.

Making use of Equation 2-52, the expression for current density (Equation 2-48) can be multiplied by an effective emission area (α) to give an expression for current as a function of applied electric field (E):

$$\begin{aligned} I &= aE^2 \exp\left(-\frac{b}{E}\right), \\ a &\equiv \alpha \frac{A\beta^2}{1.1\varphi} \exp\left(\frac{9.84}{\varphi^{\frac{1}{2}}}\right), \\ b &\equiv \frac{0.95B\varphi^{\frac{3}{2}}}{\beta}, \\ A &= 1.51\times10^{-6}\,\mathrm{A\cdot eV\cdot V^{-2}}, \\ B &= 6.831\times10^{7}\ (\mathrm{eV})^{-\frac{3}{2}}\ \cdot \mathrm{V\cdot cm^{-1}} \end{aligned} \tag{2-53}$$

Equation 2-53 is the form of the Fowler-Nordheim equation. Generally, the following equation is commonly used in experiment [40, 48].

$$\ln(I/E^2) = \ln[A\alpha\beta^2/(\phi/e)] - B(\phi/e)^{\frac{3}{2}}/(\beta E) \tag{2-54}$$

where $A = 1.06$ μA·V^{-1} and $B = 6.85\times10^{3}$ V$^{-0.5}$·μm^{-1} are constants. ϕ (in eV) is the work function (The symbol φ is used in above derivation of F-N equation). E= V/d (electric field in parallel plate configuration defined by the ratio of applied voltage to the probe-sample distance in V/μm) is the applied electric field (The symbol F is used in above discussion). e is the magnitude of the electron charge. I (μA) is the measured emission current. β is the field enhancement factor. α is the effective emission area in μm^2. It can be seen that plotting field electron emission data in what is termed Fowler-Nordheim coordinates, namely $\ln(I/E^2)$ versus $1/E$, yields a straight line, with a slope $-b = B(\phi/e)^{\frac{3}{2}}/\beta$ and intercept $\ln(a)$ with $a = A\alpha\beta^2/(\phi/e)$. Furthermore, the experimentally determined values of a and b can be multiplied together to yield

$$ab^2 = \alpha \frac{0.95AB^2\phi^2}{1.1} \exp\left(\frac{9.84}{\phi^{\frac{1}{2}}}\right) \equiv \alpha(6.206\times10^9)g(\phi)\,, \tag{2-55}$$

where

$$g(\phi) = \phi^2 \exp\left(\frac{9.84}{\phi^{\frac{1}{2}}}\right), \tag{2-56}$$

which is independent of the field enhancement factor.

Clearly, if the work function is known, then emission area can be determined from Equation 2-53. However, even if the exact value of the work function is unknown (e.g. variations in work function due to different surface orientations), the emission area can be determined within an error of 10% or less. It is only necessary that a material have a work function within the range of 3.5-11.5 eV. This can be illustrated by plotting $g(\phi)$ from Equation 2-56 (Figure 2-5).

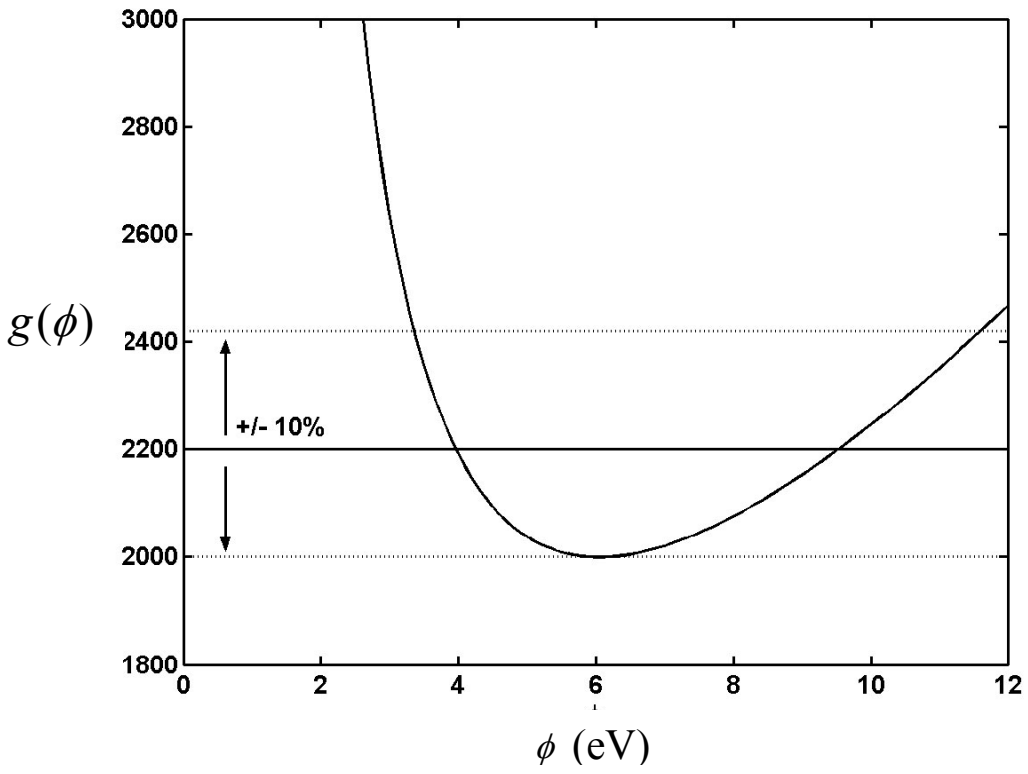

Figure 2-5: Plot of $g(\phi)$ illustrating maximum error of 10% in the range of 3.5-11.5 eV.

Chapter 3

Synthesis and Characterization of Diamond Films

The main work of this project is focused on the field electron emission study. Some work on the synthesis of diamond films has also been done. The method commonly used for the growth of diamond films is the plasma enhanced CVD process. This chapter will describe the CVD reactors used to grow diamond films and the techniques used to characterize the morphology, composition, and most importantly, the field electron emission properties of these films. The samples include carbon-based nanocones and the diamond films synthesized through graphite etching (provided by Professor Qiaoqin Yang), the diamond films with well-oriented grains (prepared by Mr. Weifeng Chen), and other samples synthesized by myself. In particular, the system used for measuring field electron emission properties and the use of Raman spectroscopy for qualitatively characterizing the composition (sp^2/sp^3) of diamond will be described.

3.1 Plasma Enhanced Chemical Vapor Deposition

All the carbon-based films in the experiments were prepared using a hot filament CVD reactor and a microwave plasma enhanced CVD reactor. Before each deposition, the silicon substrate was treated by hydrogen ions to remove the possible silicon oxide on the surface.

3.1.1 Hot Filament CVD System

The hot filament CVD system was used in this work for the synthesis of diamond nanocone films and diamond nanocomposite films. Pure hydrogen gas was used in the process and the carbon etched by hydrogen from a solid graphite sheet was the source for the growth of films. Figure 3-1 shows the configuration of the hot filament CVD reactor. The filament was a coiled tungsten wire of 0.3 mm in diameter and was heated by an ac power supply at voltages of 30~40 V and corresponding currents of 9~10 A. A thermocouple was mounted behind the substrate to measure the substrate temperature. The distance between the filament and substrate was typically 8 mm and the typical substrate temperature was 700 ºC. P-type mirror polished Si wafers ((100)-oriented) were used as substrates. An isotropic ultrafine polycrystalline graphite sheet (Poco's EDM-3) was placed beside the silicon substrates. The graphite etched by hydrogen is the carbon source for diamond growth. After the substrates and graphite sheet were placed on the substrate holder, the deposition chamber was pumped down to a base pressure of 2.7 Pa using a rotary pump. Then pure hydrogen was introduced using a mass flow controller at a constant flow rate of 30 sccm. When the working pressure was stabilized at the preset value, a current was passed through the tungsten filament coil which is followed by different processes for deposition of various films. After the deposition processes, a trough was formed on the graphite surface closest to the filament, providing a direct evidence of etching. More detailed experimental conditions will be described in Chapter 4.

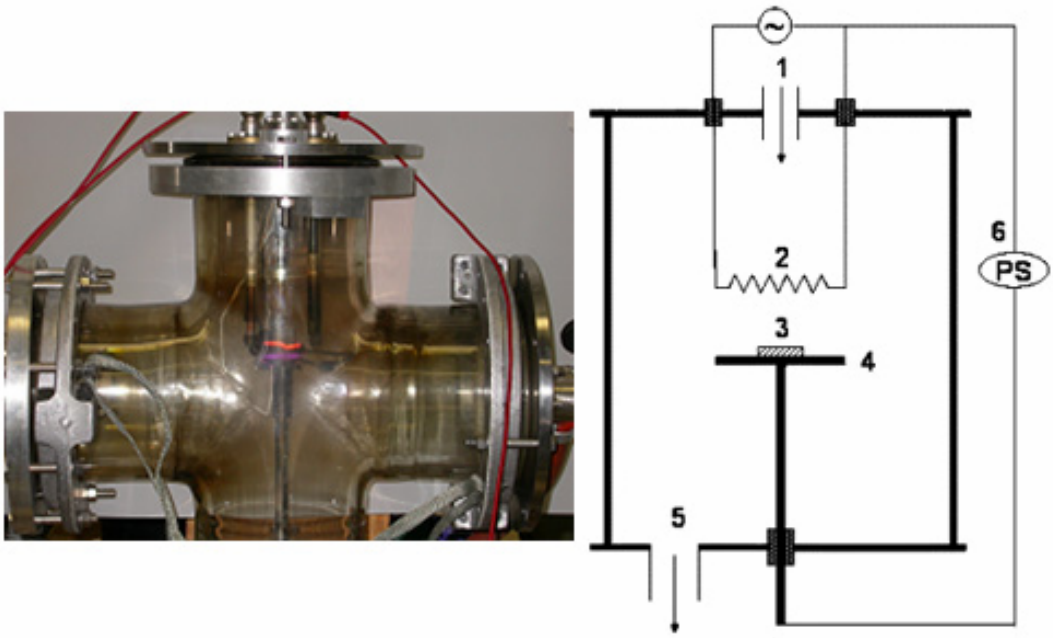

Figure 3-1: Device picture (left image) and schematic (right image) of the hot filament chemical vapor deposition system: (1) gas inlet, (2) filament, (3) substrate, (4) substrate holder, (5) pumping port and (6) dc power supply. A Pyrex glass cross of diameter 20 cm is used as vacuum chamber.

3.1.2 Microwave Plasma-Enhanced CVD System

All the other diamond films were prepared using a microwave plasma-enhanced CVD system (Figure 3-2). The maximum power of the 2.45 GHz microwave source is 1 kW. Two growth methods were used to synthesize diamond films. One uses hydrogen and methane as the reaction sources (Figure 3-2b). By controlling the deposition conditions including the methane concentration and the gas flow rate, diamond films with different morphologies and sp^2 phase concentrations can be prepared. The other one for diamond growth uses graphite etching (Figure 3-2c). In this method, diamond films were deposited on the Si substrate with a high growth rate using graphite etching as carbon source. In conventional diamond synthesis using hydrogen and methane, a substrate temperature above 700 ^{0}C is required for the synthesis of high quality diamond films with reasonably high growth rates. Therefore substrates that melt or undergo problematic phase transitions at such high temperatures cannot be employed. Removing this limitation by decreasing the synthesis temperature would significantly expand the applications of diamond films. Graphite etching can

overcome this disadvantage. High quality diamond films have been deposited at temperatures as low as 250 ˚C using this method. The advantages of the new process over the conventional methods using H_2 and CH_4 gas mixture include deposition at lower temperature, higher growth rate, and reduced carbon soot contamination to the deposition system.

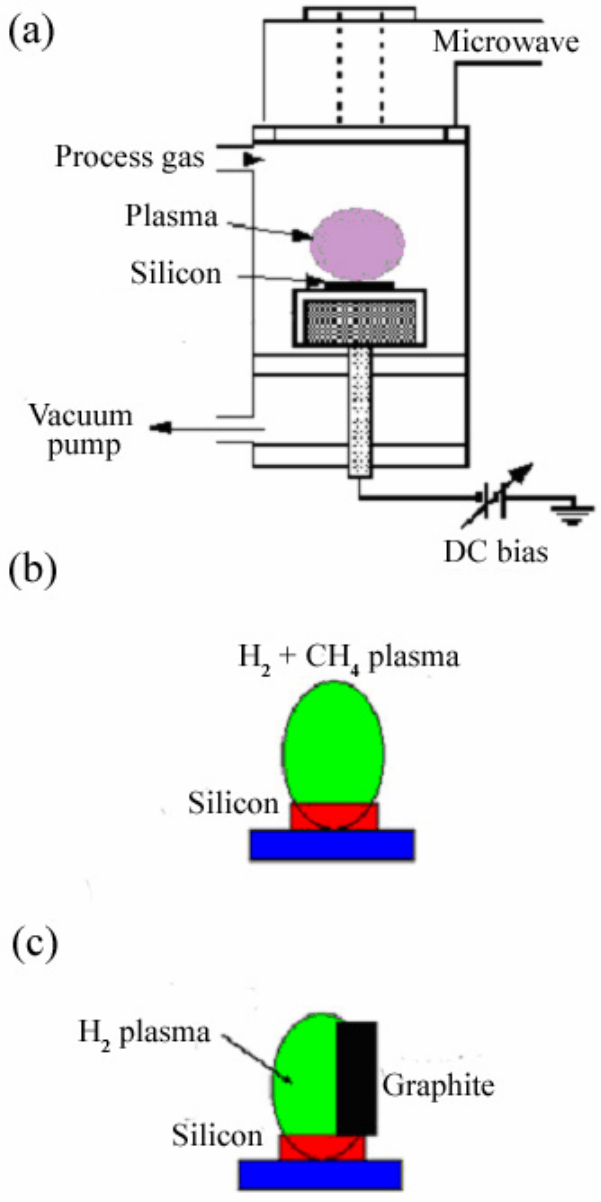

Figure 3-2: Schematic of the microwave CVD system: (a) configuration of reactor, (b) diamond grown using H_2 and CH_4 and (c) diamond grown through graphite etching with pure hydrogen working gas.

The detailed experimental conditions for growth of various diamond and related films will be described separately in the following Chapters.

3.2 Characterizations

Several characterization techniques were used to analyze the surface morphology and compositions of deposited diamond films:

3.2.1 The Surface Morphology

The surface morphologies of diamond and related films were mainly characterized by the scanning electron microscope (JEOL 840A), which is housed in the Electron Microscopy Laboratory, Department of Geological Sciences, University of Saskatchewan. An Atomic Force Microscope (AFM) at the Saskatchewan Structural Sciences Centre (SSSC) was also used to obtain morphology and surface roughness information on the diamond films.

3.2.2 The sp^2 Phase Concentration

The sp^2 phase concentrations of diamond films were estimated using Raman spectroscopy at SSSC. Raman scattering is the inelastic scattering of incident photons by matter. For scattering off a solid material, the photons may either lose part of their energy by exciting phonons in lattice vibrations (Stokes), or they may gain energy by absorbing phonons (anti-Stokes). The scattered photon is shifted in wavelength by the phonon energy (called Raman shift). Typically, the Stokes signal is more intense at room temperatures, and so is generally used.

Raman spectroscopy is the most commonly used method for differentiating between three-coordinated sp^2 carbon bonding and four-coordinated sp^3 carbon bonding. Because of the relative ease of the technique and its ability to distinguish carbon bonds, the application of Raman spectroscopy to diamond and related materials has been extensively studied.

The scattering efficiency of graphite (sp^2) is approximately 50 times higher than that of diamond (sp^3). This difference in scattering efficiencies has the benefit that Raman spectroscopy is ideal for detecting the small concentration of the sp^2 carbon

phase in diamond films. The choice of the wavelength of the laser excitation is very important, since the intensities and peak positions of some non-diamond carbon is dependent on the wavelength used. The Raman cross section of non-diamond carbon relative to diamond increases with increasing wavelength of the excitation source. Two possible explanations have been suggested for this effect. The first is that a resonance effect occurs for the non-diamond carbon at longer wavelengths. In this case, the laser excitation wavelength is close to the energy of electron transitions, causing an increase in the signal intensity. The second theory is ascribed to an absorption effect, where graphite and other non-diamond carbon have higher absorption efficiency than that of diamond. As the excitation wavelength is changed, the relative interaction volume is changed, causing a change in signal intensity. In order to analyze the sp^2 phase concentration in diamond films, an excitation source with long wavelength (visible Raman) is often used.

In the Raman spectra of CVD diamond films, the sharp peak at 1332 cm^{-1} shows the characteristic diamond peak and a peak at 1580 cm^{-1} indicates the presence of the sp^2 phase. As already mentioned, the high intensity of the sp^2 feature in the spectrum for CVD diamond is largely the result of the high scattering efficiency for sp^2 carbon. In order to analyze the sp^2 phase information in diamond films, the Raman spectra were obtained using a Renishaw micro-Raman system 2000 spectrometer operated at an argon laser wavelength of 514.5 nm (visible Raman). The laser spot size was approximately 2 μm in diameter.

3.3 Field Electron Emission Measurement

3.3.1 High Vacuum for Field Emission Measurement

Normally, field electron emission measurements are performed under very high vacuum due to the following reasons:

- To avoid absorption of emitted electrons by air molecules

During the period after emission from the solid surface and before electrons reach the anode collector, the chance that electrons will be absorbed by air molecules is large if the density of air molecules is large. Thus the number of electrons reaching

the probe will be reduced. The value of emission current measured will be reduced. Field electron emission measurements under such conditions do not reflect the real FEE properties of cold cathode materials. In order to avoid this situation, a low pressure is necessary in the FEE measurement device.

- To make the field electron emission start before avalanche breakdown

According to Paschen theory, when an electric field is applied between two electrodes, gas breakdown may occur if emitted electrons gain enough energy between successive collisions with neutral air molecules to ionize them. Ionization releases an additional electron which is also accelerated, collides with air molecules, and causes more ionization. Finally, if these mechanisms are allowed to persist, the avalanche breakdown will happen.

The maximum voltage without avalanche breakdown is given by the following equation:

$$V_{\max} = \frac{Apd}{\ln(pd) + B},$$

$$A = \frac{V_i}{(1.013 \times 10^5\, Pa) l_0}, \tag{3-1}$$

$$B = -\ln\left((1.013 \times 10^5\, Pa) l_0 \ln\left(1 + \frac{1}{\gamma}\right)\right),$$

where $V_{\max}$ is the maximum voltage without avalanche breakdown; V_i is the ionization energy of the air; p is the air pressure; d is the distance between two electrodes; γ is constant; l_0 is the mean free path of air molecules.

Figure 3-3 shows Paschen curves for air, nitrogen and hydrogen. With the decrease of the *pd* product, the voltage required for avalanche breakdown is decreased firstly and then increased. A minimum voltage of 327 V is obtained for the *pd* product of about $0.65\ \text{cm} \cdot \text{Torr}$.

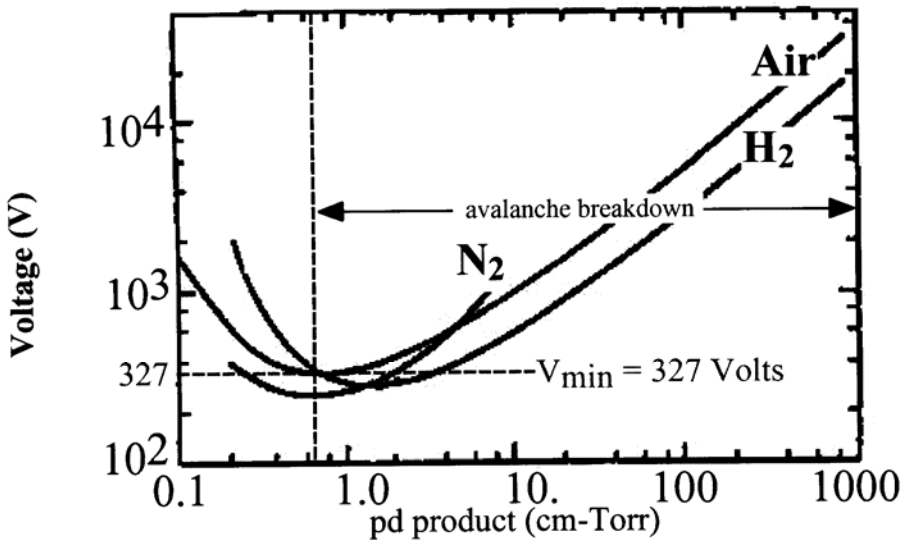

Figure 3-3: The Paschen curve for dry air, nitrogen and hydrogen [49].

In order to obtain field electron emission results, the field electron emission has to be started before avalanche breakdown occurs. Moreover, the maximum electric field applied in field electron emission measurement should be smaller than the electric field necessary for avalanche breakdown in the given conditions. The vacuum during the field electron emission measurement in this research is usually 1.3×10^{-5} Pa (1×10^{-7} Torr). Assuming that the distance between the probe and sample is d=30 μm, then $pd=3\times10^{-10}$ (cm·Torr). The corresponding voltage from the Paschen curve is over 3000 V. Generally, the voltage used in field electron emission measurements was about 1000 V, well below the critical values causing avalanche breakdown.

3.3.2 Field Electron Emission Measurement System

A field electron emission measurement device with a parallel plate structure was designed and set up to perform the *I-E* measurement, as given in Figure 3-4. The diameter of the stainless steel anode is 1 mm, and the anode-cathode spacing can be adjusted using a micrometer in the range of 0 – 100 μm. A high voltage source-measurement unit, a Keithley 237, was used in the field electron emission measurement. The Keithley 237 is a fully programmable instrument, capable of sourcing and measuring voltage and current simultaneously. The Keithley 237 is

connected to a PC using IEEE 488 (GPIB) card. The data acquisition was performed using Labview software. The field electron emission *I-E* curve and corresponding F-N plot can be obtained and displayed on the computer screen at the same time. The anode and sample were placed in a stainless steel vacuum chamber. The current – voltage (*I-E*) measurements were performed at room temperature in a high vacuum, maintained by a turbo molecular pump backed by a mechanical pump. The system can reach the base pressure of $(1-2)\times10^{-7}$ Torr in 3 hours. For adjusting the distance between anode and cathode without damaging the sample surface, the anode was moved down to the sample while monitoring the resistance between the anode and sample. The distance was set to be zero when the resistance changes from infinity to a finite value. Then the anode was moved up to the desired distance for field electron emission measurement. Before each FEE test, a limitation of maximum emission current was preset to avoid the variation of surface morphology due to too large emission current.

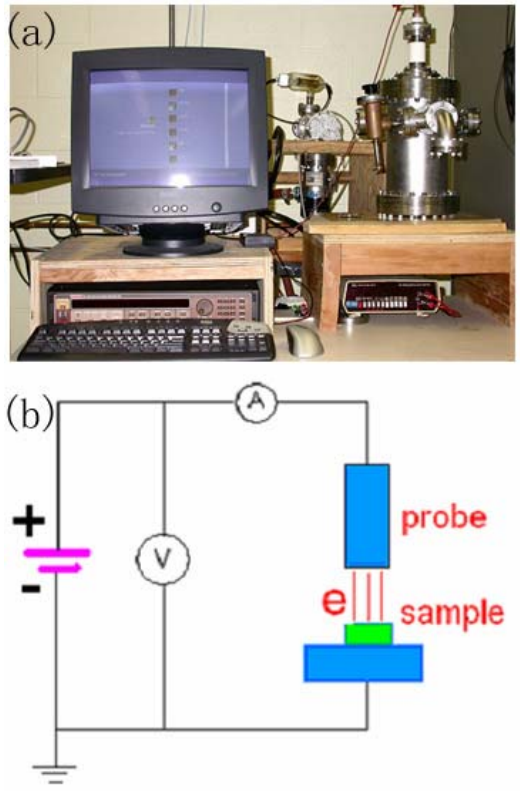

Figure 3-4: Device image (a) and schematics (b) of set-up for field electron emission measurement. The left part of (a) is Keithley 237 unit. The right part of (a) is the high vacuum chamber with the test probe and sample inside.

Chapter 4

Field Electron Emission Characteristics of Diamond Films: Influence of Surface Morphology

Surface morphology has an important influence on the field electron emission properties of diamond films [50-52]. In this experiment, diamond films with different morphologies were prepared. The field electron emission characteristics were investigated.

4.1 Microcrystalline Diamond Films with Different Grain Morphologies

In this experiment, the field electron emission properties of microcrystalline diamond films with different grain morphology were studied. The influence of the orientation and shape of diamond grains on field electron emission are investigated.

4.1.1 Sample Preparation

The diamond films with different grain morphologies were prepared in the microwave CVD reactor. The microcrystalline diamond thin film samples were synthesized in a 2.45 GHz microwave CVD system using a gas mixture of CH_4 and H_2 under controlled conditions. The *p*-type (100)-oriented mirror polished silicon wafers placed on a stainless steel holder were used as substrates. Under the action of substrate bias voltage, diamond grains can grow preferentially along (100) orientation. Figure 4-1 shows SEM images of four films with different types of diamond grains as described

in the figure caption. The orientation of diamond grains can be analyzed by x-ray diffraction (XRD).

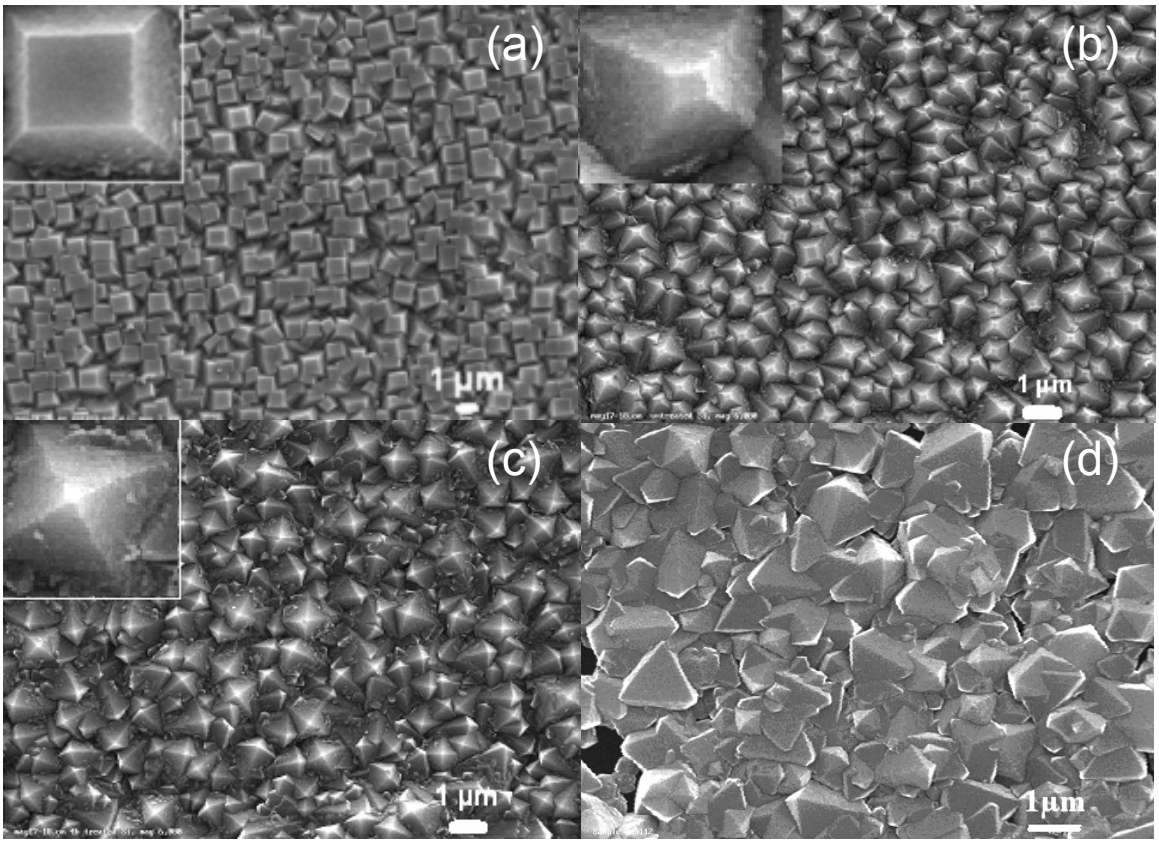

Figure 4-1: Typical SEM micrographs of diamond films with different grain morphologies: (a) well aligned flat grains, (b) well aligned flattened pyramid grains, (c) well aligned pyramid grains, and (d) randomly oriented grains. The insets in (a), (b) and (c) show the enlarged views (8 times SEM micrographs) of a selected grain.

The well-aligned diamond films shown in Figure 4-1a-c were prepared by the following two steps. In both steps, the total pressure, substrate temperature, and microwave power were maintained at 30 Torr, 700 ^{o}C, and 1000 W, respectively. In the first plasma processing step, the Si substrates were pretreated for 30 min in a microwave plasma with a gas mixture of 5% CH_4 and 95% H_2 with a bias enhanced nucleation (BEN). A bias voltage of -300 V was applied to the substrate. The total gas flow rate, controlled accurately by a mutichannel mass flow controller, was fixed at 100 sccm. In the second plasma processing step, the bias voltage was removed and the

methane concentration was reduced to 2%. The diamond films with well-aligned flat grains (Figure 4-1a) were synthesized at a gas flow rate of 200 sccm. By reducing the gas flow rate from 200 sccm to 50 sccm, diamond films with flattened pyramid grains were obtained (Figure 4-1b).

In order to synthesize the diamond films with sharp pyramid tips shown in Figure 4-1c, the silicon substrate was first scratched in an ultrasonicated bath containing diamond paste to increase the diamond nucleation rate. Then the diamond film was deposited in the microwave plasma using a gas mixture of 1% CH_4 and 99% H_2 at a flow rate of 50 sccm.

The microcrystalline diamond film with randomly oriented grains shown in Figure 4-1d was deposited directly on the untreated silicon substrate with a gas mixture of 1% CH_4 and 99% H_2 and a bias voltage of -100V in the microwave plasma reactor.

4.1.2 Results and Discussion

The Raman spectra of the diamond films under investigation are very similar. Figure 4-2 displays a typical Raman spectrum of randomly oriented diamond films containing both diamond (sp^3 peak at 1332 cm^{-1}) and graphite (sp^2 peak at 1550 cm^{-1}) graphitic phases [53].

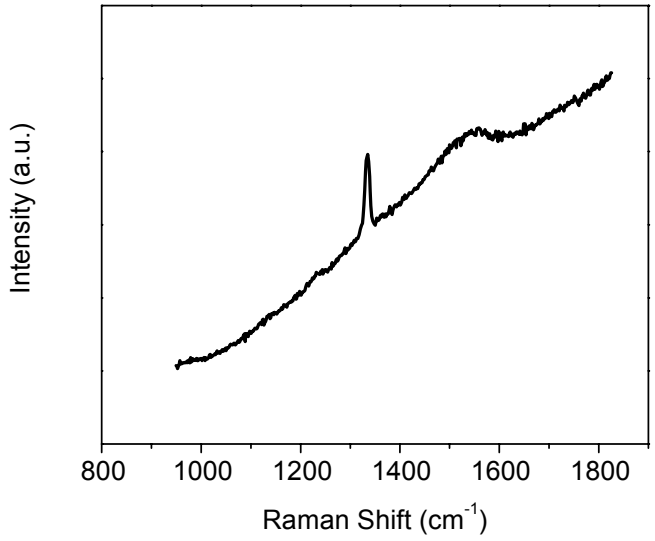

Figure 4-2: Raman spectrum of randomly oriented diamond films.

The typical field electron emission *I-E* curves for the diamond films with different grain morphologies are shown in Figure 4-3. Note that the current, not the current density, is shown. This is because the emission current density is often ill defined due to the ambiguity in the emission area (physical anode surface area is not necessarily the effective emission area). A turn-on electric field (defined as the electric field corresponding to the emission current of 0.01 μA) of 8.0 V/μm and an emission current of 0.8 μA at 20 V/μm for the sample "a" (corresponding to the diamond film shown in Figure 4-1a can be determined from the *I-E* curve. With the decrease of the grain top area, the turn-on electric fields for the sample "b" and sample "c" (corresponding to the diamond films shown in Figure 4-1b and Figure 4-1c) were decreased to 5.0 V/μm and 2.5 V/μm, respectively. The corresponding emission currents at the electric field of 20 V/μm were increased to 2.6 μA and 5.6 μA, respectively.

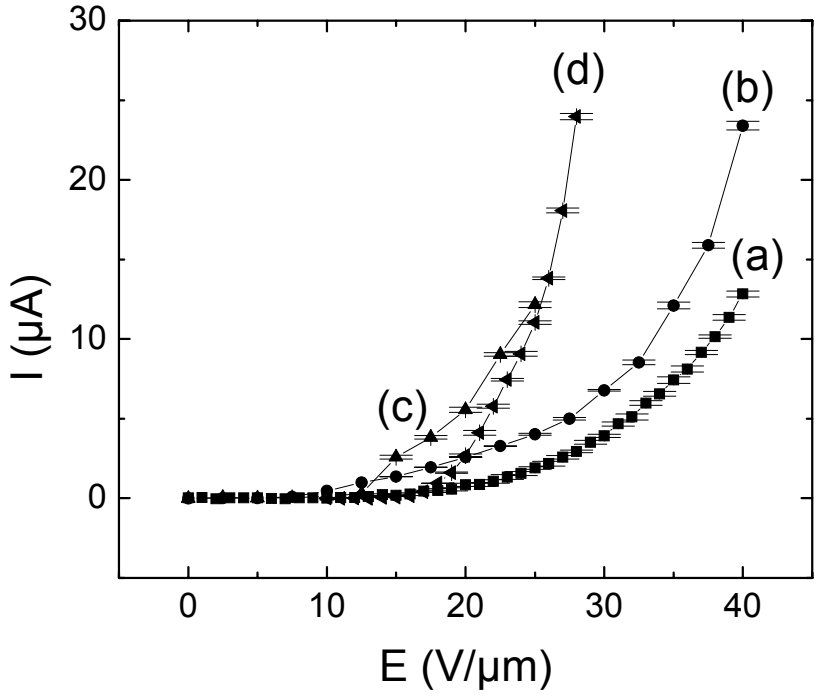

Figure 4-3: Typical field electron emission *I-E* curves of diamond films with different grain morphologies: (a) well aligned flat grains, (b) well aligned flattened pyramid grains, (c) well aligned pyramid grains, and (d) randomly oriented grains.

For the microcrystalline diamond film with randomly oriented grains, a turn-on electric field of 7.0 V/μm and an emission current of 2.7 μA at 20 V/μm were observed (Figure 4-3d).

The existence of a significant amount of sp^2 phase shown in Figure 4-2 warrants the application of the Fowler-Nordheim field electron emission theory, which is usually applied to conductors, to the diamond samples studied. Furthermore, other authors have suggested that the conducting graphitic phase on the crystal boundary is another factor allowing application of the Fowler-Nordheim theory to diamond [54].

It is known that the work function depends mainly on the material. However, orientation of crystals may also affect the work function [55-57]. For diamond, work function values in the range between 4 eV and 5 eV have been used by some researchers [58, 59]. A constant work function value of 5 eV has been assumed for all diamond films with different morphologies investigated in this study. It should be pointed out that the β value derived from the slope of an F-N plot is proportional to $\phi^{\frac{3}{2}}$. Different choices of the ϕ values in the range 4-5 eV have an impact on the field emission factors and effective emission areas. But the impact remains small enough when compared with the values across different samples as to be shown.

The field electron emission F-N plots of the microcrystalline diamond films with different grain morphologies are shown in Figure 4-4. Each F-N plot can be fitted into a straight line above a threshold electric field, which is defined by the electric field at which the F-N plot becomes a straight line. The deviation of the F-N plot from a straight line below the threshold electric field may be attributed to the influence of resonance states on the emitter surface. Absorbates have been considered as the source of these states [60]. The threshold electric fields for the diamond samples “a” – “d” are approximately 21 V/μm, 25 V/μm, 15 V/μm and 20 V/μm, respectively. The solid symbols indicate the data points below the threshold electric field. The data points denoted by the open symbols above the threshold electric field were used for fitting and the resultant straight lines are also shown.

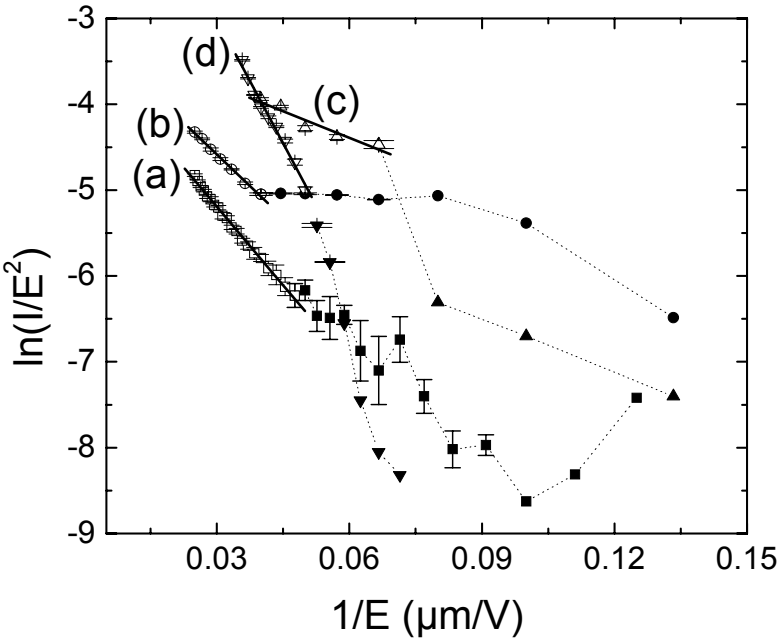

Figure 4-4: Typical field electron emission F-N curves of diamond films with different grain morphologies: (a) well aligned flat grains, (b) well aligned flattened pyramid grains, (c) well aligned pyramid grains, and (d) randomly oriented grains. For some data points, the error bars are smaller than the symbols.

Table 4-1 summaries the turn-on field, the emission current at 20 V/μm, the threshold field, the fitted field enhancement factor and the effective emission area for the four diamond samples "a" – "d". Two β values are given for each sample in the table to indicate the range of the field enhancement factors when the work function is varied from 4 eV to 5 eV. Since the range of the field enhancement factor of any sample has little overlap with that of other samples, the choice of the work function value does not greatly affect the relative field enhancement factor. Therefore, it suffices to use the values of the field enhancement factor corresponding to ϕ =5 eV throughout the discussion to follow.

Table 4-1: Typical field electron emission parameters of diamond films with different grain morphologies: (a) well aligned flat grains, (b) well aligned flattened pyramid grains, (c) well aligned pyramid grains, and (d) randomly oriented grains. Two values, corresponding to ϕ =4 eV and ϕ =5 eV, are given for the field enhancement factors and effective emission areas.

Sample	**Turn-on field (V/μm)**	**Emission current (μA) at 20 V/μm**	**Threshold field (V/μm)**	**Field enhancement factor**	**Effective emission area (μm^2)**
a	8.0	0.8	21	950-1250	$(1.0\text{-}1.6)\times10^{-7}$
b	5.0	2.6	25	1180-1550	$(0.9\text{-}1.3)\times10^{-7}$
c	2.5	5.6	15	2820-3710	$(1.5\text{-}2.3)\times10^{-8}$
d	7.0	2.7	20	600-790	$(0.7\text{-}1.1)\times10^{-5}$

For the diamond films with well-oriented grains (samples “a”, “b” and “c”), the improvement of field electron emission properties originates mainly from the increase in the field enhancement factors. With the change of grain morphology from the flat to flattened pyramid and then to pyramid shape, the field enhancement factors of samples “a”, “b” and “c” increase from 1250 to 1550, then to 3710. The increase in field enhancement factors is due to the sharpness of diamond grains. At the same time effective emission areas of 1.0×10^{-7} μm^2, 8.8×10^{-8} μm^2 and 1.5×10^{-8} μm^2, decreasing with the increase in the field enhancement factor, were observed. The fact that the effective emission area decreases with the increasing field enhancement factor may be attributed to the screening effect due to a locally enhanced electric field which prevented the electron emission from other potential emission sites in the close vicinity. A similar relationship between the field enhancement factor and the effective emission area has also been found by other researchers. J. C. She *et al.* have found that the emission current from a group of emission sites is dominated by a very small proportion of exceptionally protruded sites. The current from the surrounding sites will be several orders of magnitudes smaller [61]. Therefore, it can be speculated that emission sites with the largest field enhancement factors could be responsible for most of the total effective emission areas. Thus, the contribution of those sites with small field enhancement factors is screened.

From the F-N equation, the emission current is linearly dependent on the effective emission area α. The emission current is also proportional to the square of the field enhancement factor β^2 in addition to the strong β dependence in the exponent $\exp[-B(\phi/e)^{3/2}/\beta E]$. For the diamond films with well-aligned grains, the effect of the increasing field enhancement factor on the emission current outweighs the effect of the decreasing effective emission area.

For the randomly oriented diamond film, a significant (two orders of magnitude) increase in the effective emission area leads to an overall improvement in the field electron emission current compared to the well aligned diamond films. The size of diamond grains in the sample "d" is similar to that of the well-aligned grains in samples "a" – "c". The randomness of the diamond grain orientation in sample "d" appears to be the reason for the reduced field enhancement factor and increased effective emission area. It can be seen that some edges of the diamond grains in sample "d" protruded from and parallel to the film surface. The field enhancement factor (effective emission area) near those "lines" is expected to be smaller (larger) than the pointy tops of the pyramid. R. S. Takalkar *et al.* have also found that the edge geometry has a smaller field enhancement factor but the effective emission area is larger due to multiple emission sites along the edge as compared to the tip geometry [62], with which the observations in this experiment are consistent.

4.1.3 Conclusion

Field electron emission properties of microcrystalline diamond films with different grain morphologies have been characterized and investigated. The results demonstrate that the grain morphologies have significant influence on the field electron emission properties of diamond films. With the change of grain shape from flat to flattened pyramid, and then to pyramid, the field electron emission properties of diamond films with well-oriented grains are improved due to the increase in the field enhancement factor, even though the effective emission area is progressively reduced by screening effect. Compared with the well-oriented diamond films, the diamond film with randomly oriented grains exhibits larger emission currents. The increase in the

effective emission area is the main factor contributing to field electron emission enhancement.

4.2 Carbon-Based Nanocone Films

As seen in Section 4.1, diamond films with sharp grains exhibit low turn-on electric field due to the large geometrical enhancement factor (GEF) near the tips [63]. Larger GEF can be obtained by synthesis of diamond nanocones with nanosized tips and submicron scale roots.

In this experiment, well-aligned graphitic and diamond nanocone films were synthesized by a hot filament CVD reactor. A novel carbon nanostructure composed of well aligned nanocones of both diamond and graphitic carbon has been synthesized. The field electron emission properties of diamond nanocone films, graphitic nanocone films and mixed nanocone films have been studied. It has been found that all nanocone films investigated in the experiments exhibit better field electron emission properties including lower turn-on electric field and larger emission current at low electric field than diamond films shown in Section 4.1. Relatively, the mixed nanocone films exhibit improved field electron emission properties over the diamond nanocone films.

4.2.1 Sample Preparation

The carbon-based nanocone samples were prepared in an HFCVD reactor. In order to prepare diamond nanocone films, the following three processes have been followed. Firstly, a silicon substrate was scratched in an ultrasonicated bath containing diamond paste in order to increase the diamond nucleation rate. Secondly, microcrystalline diamond film with a thickness of approximately 10 μm was deposited on the pre-treated substrate using a gas mixture of H_2 and CH_4 (1%) without plasma. Finally, the as-grown diamond film was further processed in a pure hydrogen plasma for 2 hours.

The graphitic nanocone films were prepared on the untreated p-type (100) polished silicon wafers in a plasma of H_2 and CH_4 (20%) mixture. The deposition time was 1 hour. The higher methane concentration and untreated substrate were the main factors that contributed to the growth of graphitic nanocone.

Finally, to obtain the mixed diamond and graphitic nanocone films, sparsely distributed diamond particles were deposited on the untreated silicon substrates (with low diamond nucleation rate) in the HFCVD device without plasma. Then, mixed diamond and graphitic nanocones were grown on the substrate in an H_2 and CH_4 (1%) plasma. The deposition time was 2 hours.

4.2.2 Results and Discussion

Figure 4-5 shows the SEM images of the following three samples: (a) diamond nanocone film, (b) graphitic nanocone film, and (c) mixed diamond and graphitic nanocone film. The nanocones are well-aligned with nanosized tips and submicron scale roots. Figure 4-6 shows the typical Raman spectra of above three samples. The strong peak at 1332 cm^{-1} observed in the Raman spectrum of the sample (a) confirms that the nanocones shown in Figure 4-5a are diamond. The spectrum of sample (b) contains two broad peaks, identified as the D-band and G-band of graphitic carbon, suggesting that the nanocones shown in Figure 4-5b are graphitic. The Raman spectrum of the mixed nanocone film is similar to Figure 4-6a in some areas (denser area in Figure 4-5c) and similar to Figure 4-6b in other areas. The plot shown in Figure 4-6c is the Raman spectrum taken cross the border between the two areas, and exhibits a narrow diamond peak superimposed on the broad D-band and G-band peaks of graphitic carbon, indicating a mixture of diamond and graphitic structure. The results suggest that the nanocones shown in Figure 4-5c are a mixture of diamond and graphitic nanocones and the diamond and graphitic nanocones were grown in substrate areas with and without pre-deposited diamond particles, respectively.

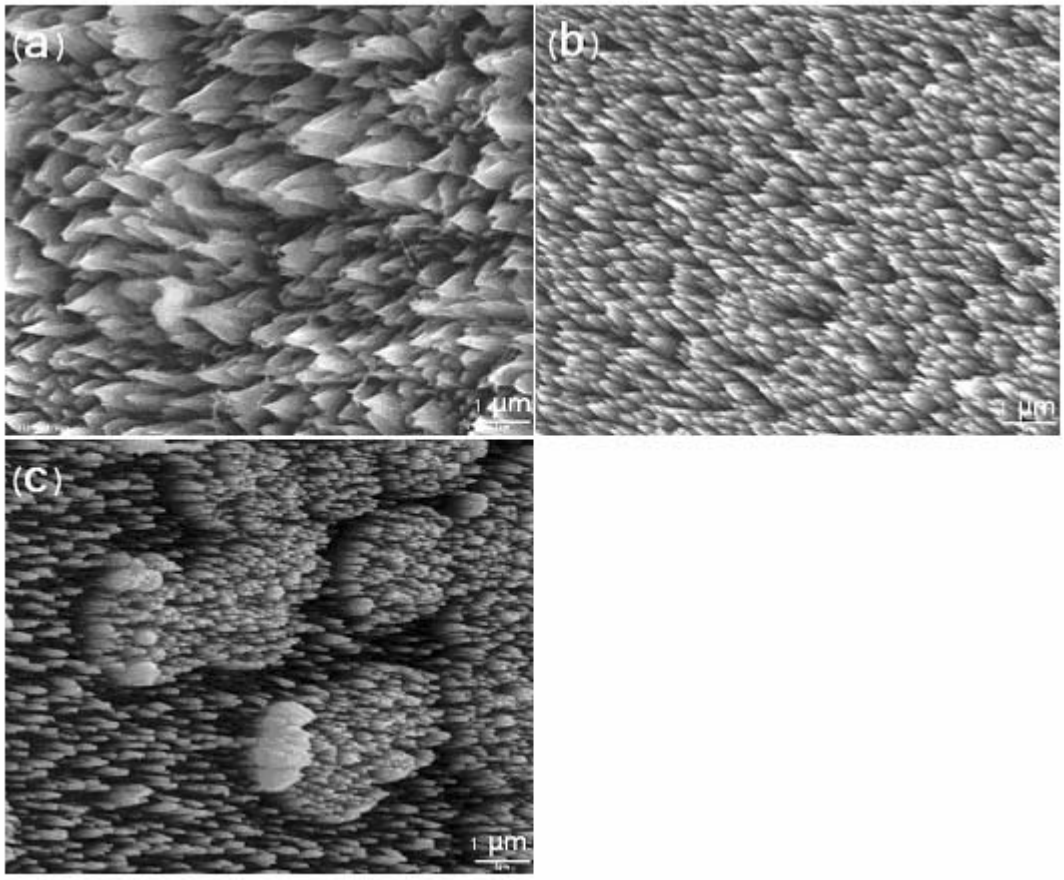

Figure 4-5: Typical SEM micrographs of (a) diamond nanocone film, (b) graphitic nanocone film, and (c) mixed diamond and graphitic nanocone film.

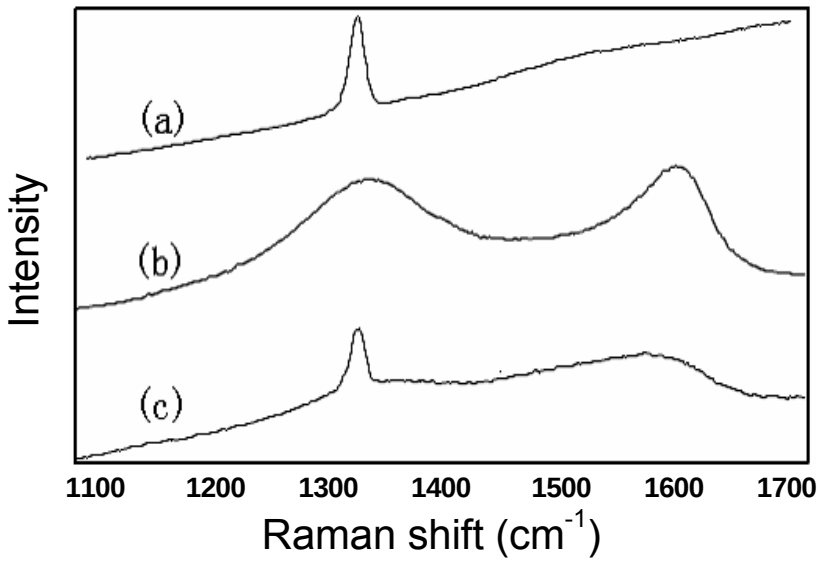

Figure 4-6: Typical Raman spectra of (a) diamond nanocone film, (b) graphitic nanocone film, and (c) mixed diamond and graphitic nanocone film.

The field emission *I-E* curves of the samples are depicted in Figure 4-7. The turn-on electric fields of the diamond nanocone film, graphitic nanocone film, and mixed diamond and graphitic nanocone film are 10 V/μm, 4 V/μm, and 5 V/μm, respectively. The corresponding emission currents from the three samples are 86 μA at 26 V/μm, 1.8×10^2 μA at 13 V/μm and 1.7×10^2 μA at 20 V/μm, respectively. The emission currents of the graphitic nanocone film and the mixed nanocone film are significantly larger than those of the diamond nanocone film. This may be attributed to the higher conductivity of the graphitic nanocones in the graphitic nanocone films and the mixed nanocone films. Electrons in the graphitic nanocone films can be transported to the surface easily, thus enhancing the electron emission current. The turn-on field for the graphitic nanocone film is much lower than that of the diamond nanocone film. The difference may be attributed to the difference in the field enhancement factor which depends on the geometry of the cone tips. Comparing the micrograph of the graphitic nanocone film in Figure 4-5b with that of the diamond nanocone film in Figure 4-5a, the former has tips with a higher aspect ratio which may be responsible for larger GEF. It has also been noticed that the turn-on field of the diamond nanocone films is much lower than those reported for diamond films without the cone structure [64-68].

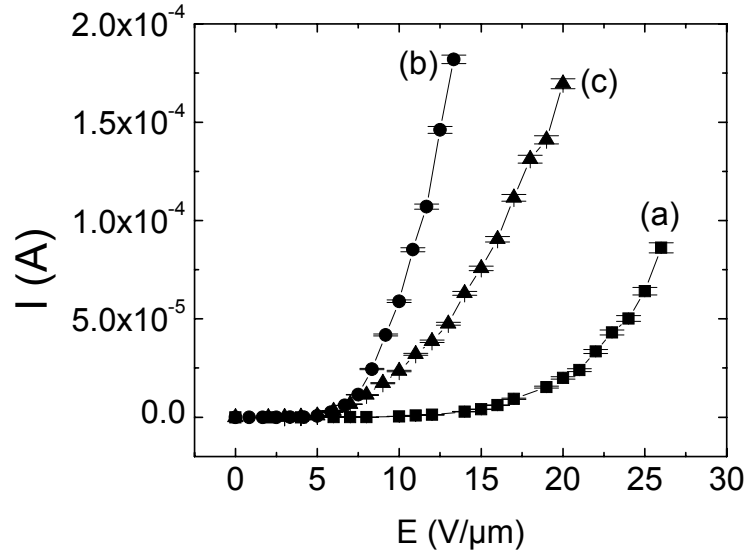

Figure 4-7: *I-E* curves of (a) diamond nanocone film, (b) graphitic nanocone film, and (c) mixed diamond and graphitic nanocone film.

The corresponding F-N plots of the samples are shown in Figure 4-8. The symbols in the plots are experimental data and the straight lines represent the best linear fitting to the experimental data. For the diamond nanocone film, the linear fitting yields a low emission area ($\alpha \sim 1.0 \times 10^{-6}$ μm^2) and a large field enhancement factor ($\beta \sim 5000$). The value of α is significantly smaller than the surface area of the probe (3.1×10^6 μm^2). The field enhancement effect is very large due to the nanocone structure shown in the SEM micrograph. The effective emission area and field enhancement factor of the graphitic nanocone film can be calculated by assuming that its work function is similar to that of graphite ($\phi \sim 4.6$ eV) [69]. The results are summarized in Table 4-2. Since the work function for the mixed diamond and graphitic nanocone film is unknown, it is not possible to determine α and β values from the linear fitting.

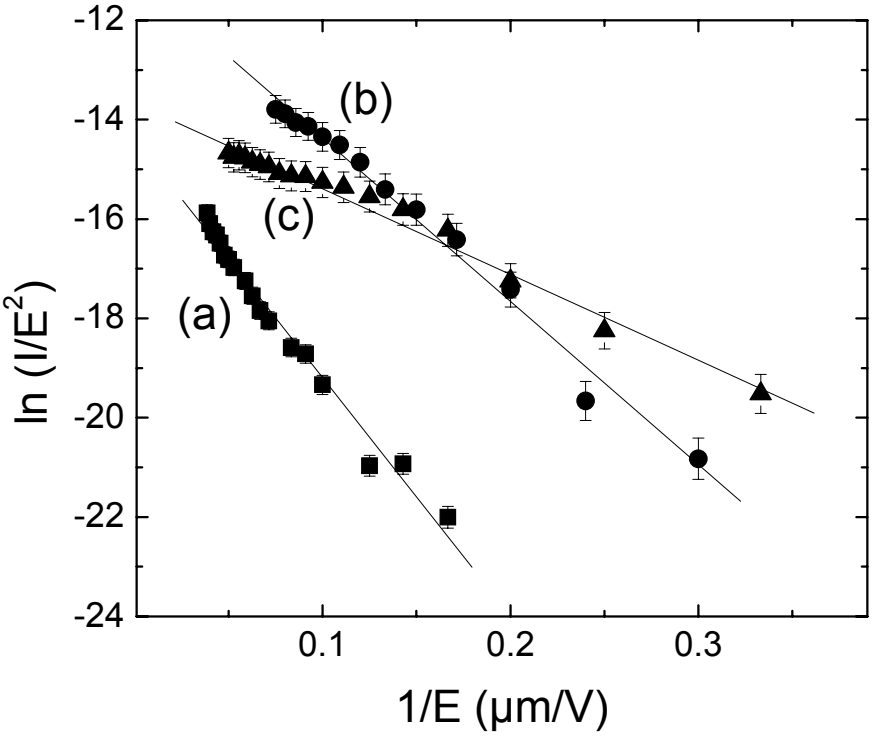

Figure 4-8: Field emission F-N plots of (a) diamond nanocone film, (b) graphitic nanocone film, and (c) mixed diamond and graphitic nanocone film.

Table 4-2: Field electron emission parameters of the diamond nanocone film, graphitic nanocone film, and mixed diamond and graphitic nanocone film.

Sample	**Turn-on field (V/μm)**	**Work function (eV)**	**Field enhancement factor**	**Effective emission area (μm^2)**	**Emission current (μA)**
Diamond nanocones	10	5	5×10^3	1.0×10^{-6}	85 at 26 V/μm
Graphitic nanocones	4	4.6	2×10^3	1.6×10^{-5}	180 at 13 V/μm
Mixed nanocones	5	N/A	N/A	N/A	170 at 20 V/μm

4.2.3 Conclusion

The field electron emission properties from diamond nanocone films, graphitic nanocone films and mixed diamond and graphitic nanocone films have been studied. It has been found that all the nanocone films exhibit much better field electron emission properties than the diamond films in section 4.1. The graphitic nanocone film has the lowest turn-on field of 4 V/μm and the highest field electron emission current of 1.8×10^2 μA at 13 V/μm. Compared to the graphitic nanocone film, the mixed diamond and graphitic nanocone film shows a slightly higher turn-on field of 5 V/μm, and a slightly smaller emission current of 1.7×10^2 μA at 20 V/μm. The field electron emission properties of the diamond nanocone films are much better than those of diamond films without the cone structure. It has also been found that the nanocone films with pure or mixed graphitic structures have better FEE properties than diamond films. The effect of the sp^2 concentration on FEE will be further discussed in Chapter 5.

4.3 Diamond Nanocomposite Films

In this experiment, the field electron emission property of diamond nanocones was further enhanced by depositing a layer of a nanocrystalline diamond film on top of diamond nanocones. The nanocomposite diamond films exhibit similar field electron

emission properties as reported for carbon nanotubes (CNTs) [70-72]. The FEE enhancement can be attributed to the sharp protrusions on the surface of the nanocomposite films in both micrometer and nanometer scales.

4.3.1 Sample Preparation

The diamond nanocomposite films were synthesized by growing nanocrystalline diamond film on a layer of diamond nanocone film through graphite etching in a plasma enhanced HFCVD reactor. The filling pressure of the pure hydrogen working pressure was in the range 5.32 Pa to 1.99 kPa (typically 1.04 kPa). Over 1.5 hours deposition without plasma in HFCVD device, a diamond film of 7 μm with submicron scale grain size was deposited on the substrate. Then, a dc glow discharge between the filament (anode) and the substrate holder (cathode) was initiated. The discharge voltage and current were approximately 300 V and 100 mA, respectively. After 1.5 hours of plasma-enhanced deposition, the diamond nanocone film was synthesized on the substrate. After that, the bias was removed and the discharge disappeared. The diamond nanocone film was further processed for additional 1.5 hours without discharge. A layer of nanocrystalline diamond was deposited on the layer of diamond nanocones.

4.3.2 Results and Discussion

4.3.2.1 Characterization

Figure 4-9a-d show typical SEM images of diamond layers formed at different steps. As seen in Figure 4-9a, the diamond film deposited directly on Si through graphite etching without discharge is a very dense, continuous film. The average grain size of the film is approximately 200 nm, an order of magnitude smaller than that of the film with similar thickness synthesized by using a gas mixture of 1% CH_4 and 99% H_2.

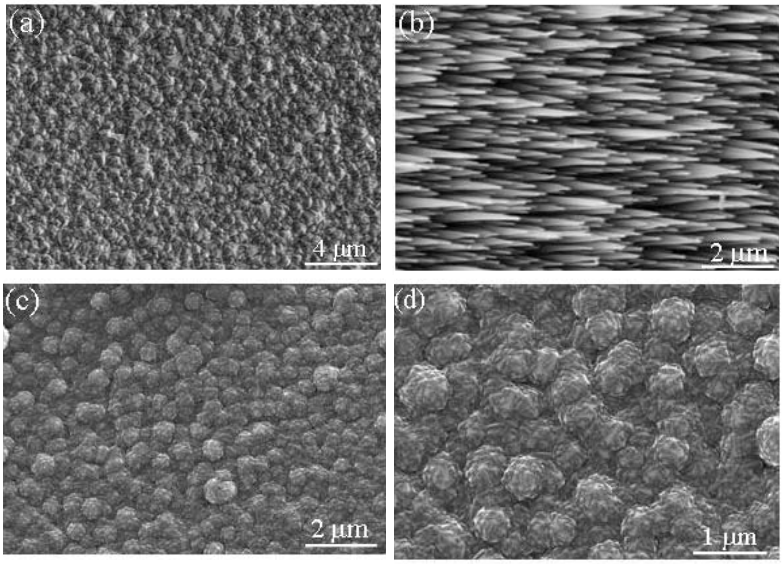

Figure 4-9: SEM micrographs of diamond layers grown (a) directly on Si without discharge, (b) after biased deposition in plasma for 1.5 hours; (c) after further deposition without plasma for 1.5 hours (low magnification); (d) same as (c) but with higher magnification).

When the submicrocrystalline diamond films were further processed for 1.5 hours in a dc glow discharge with substrate holder negatively biased, well-aligned diamond nanocones were achieved (Figure 4-9b). After the samples with nanocone features were further deposited for 1.5 hours without discharge, a nanocomposite film with a layer of nanocrystalline diamond formed on the layer of diamond nanocone film was synthesized, as shown in Figure 4-9c, d. The diamond nanocomposite film has the following features: (a) The nanocrystalline diamond layer on nanocones consists of diamond conglomerates with nanotips, (b) individual conglomerate, at the size of approximately 0.6 μm, is comprised of 20-40 grains of 15-200 nm diamond crystals, and (c) the density of the conglomerates on the diamond nanocones (Figure 4-9c) and the density of the diamond nanocones (Figure 4-9b) are on the same order of magnitude ($\sim 10^9/cm^2$), suggesting that each diamond conglomerate may have nucleated from each diamond cone and grown through high renucleation and growth of secondary nuclei. The high secondary nucleation rates are possibly the result of the high concentration of the activated hydrocarbon radicals around the substrate in the graphite etching process. Due to the high original and secondary nucleation rates, nanocrystalline diamond film was consequently synthesized on diamond nanocones.

Figure 4-10 shows the AFM 3-D surface images of diamond nanocomposite films at two different scales. Figure 4-10a depicts the height variation within an area of 8.5×7.9 μm^2 which includes several conglomerates as seen in the inset on the left-bottom corner. Figure 4-10b depicts the height variation within an area of 250×250 nm^2 which includes part of one of the conglomerates. Both images exhibit a self-similar morphology with a relatively rough surface featured by many protrusions in two different scales. The AFM images are consistent with the SEM images in Figures 4-9c and 4-9d. The morphology contains features of height variations in both micrometer and nanometer scales, which have been proved to be particularly suitable for field electron emission [73]. The turn-on electric field is expected to be very low because of the high aspect ratio of the micro- and nano-protrusions. A large effective emission area is also expected due to the irregular distribution of the tips.

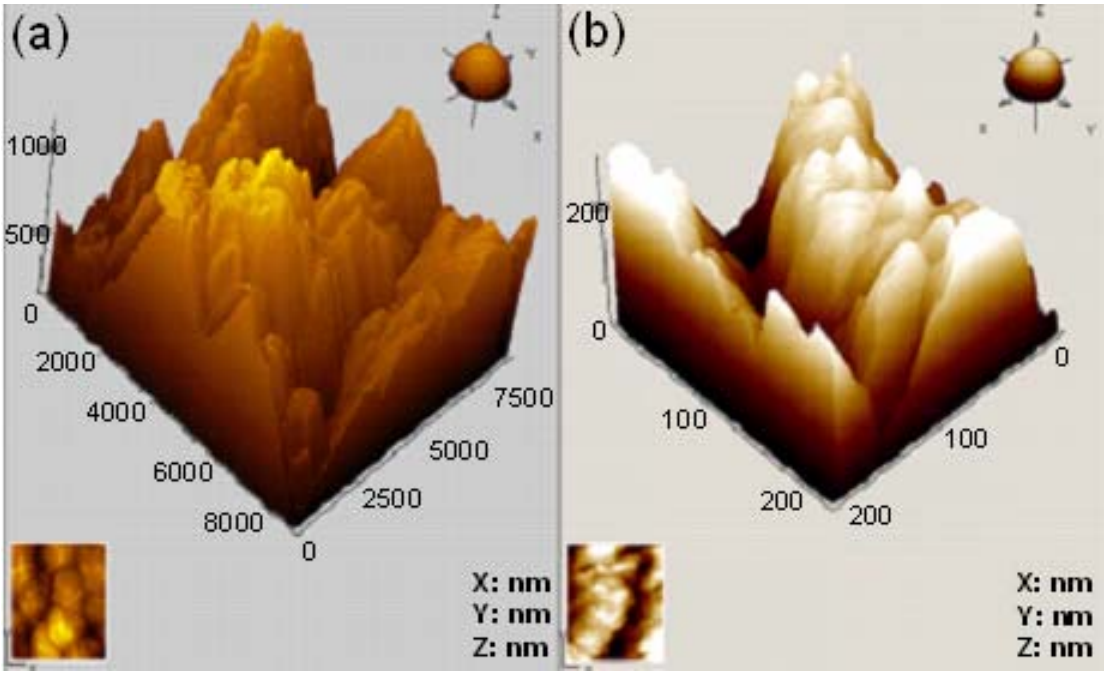

Figure 4-10: Typical AFM images of the diamond nanocomposite film: (a) for an area of 8.5×7.9 μm^2. (b) for an area of 250×250 nm^2.

A typical Raman spectrum of the diamond nanocomposite films is depicted in Figure 4-11. The sharp peak centered at 1332 cm^{-1} indicates the formation of the diamond (sp^3). In addition to this peak, a broad peak around 1550 cm^{-1}, indicative of

the non-diamond (sp^2) carbon, is observed. Considering the fact that Raman scattering in the visible range (514 nm) is about 50 times more sensitive to sp^2-bonded carbon than to sp^3-bonded carbon, the concentration of sp^2 carbon in the film is quite low. Furthermore, the grain boundaries of polycrystalline diamond usually consist of sp^2-bonded carbon. The appearance of sp^2 in the film might be attributed to the nanostructure with a large area of grain boundary. The Raman spectrum clearly reveals the presence of both sp^3 and sp^2 carbon in the film. Introduction of non-diamond carbon into the diamond films will enhance the electron emission due to the enhancement in the films' electric conductivity [74, 75].

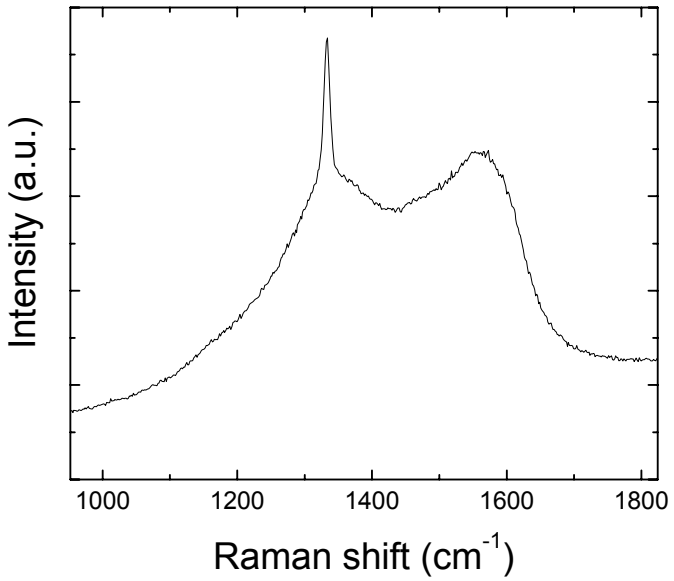

Figure 4-11: Raman spectrum of the diamond nanocomposite film.

4.3.2.2 Field Electron Emission Properties

The *I-E* curve of diamond nanocomposite films at the chamber pressure of 10^{-7} Torr is shown in Figure 4-12. The field electron emission turn-on electric field is as low as 6 V/μm. The emission current reaches 36 μA at the electric field of 20 V/μm. The observed field electron emission properties are better than either a single layer microcrystalline diamond film (emission current of 10 μA at 30 V/μm with a turn-on field of 12 V/μm) [29] or a single layer nanocrystalline diamond film (emission current of 12 μA at 20 V/μm with a turn-on field of 10 V/μm) [76]. Comparing the FEE

properties of diamond nanocomposite films with the diamond nanocone films presented in Section 4.2.2 (e.g., curve (a) in Figure 4-7), the turn-on electric field of the diamond nanocone film decreased from 10 V/μm to 6 V/μm. The corresponding emission current at the electric field of 20 V/μm increased from 19 μA to 36 μA. These results indicate that the nanocrystalline diamond film significantly enhances the field electron emission properties of diamond nanocone film.

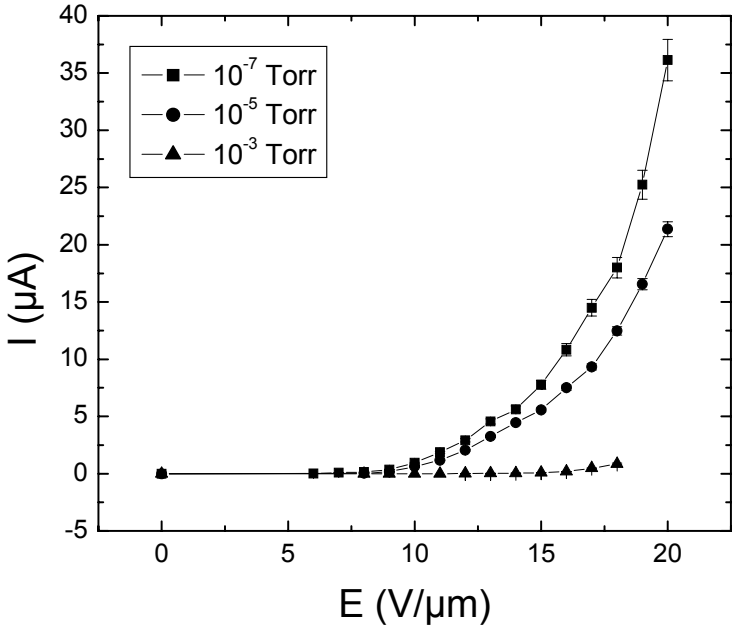

Figure 4-12: field electron emission *I-E* curves of diamond nanocomposite film at different pressures.

It has been found that absorbates have significant influence on the field electron emission process [76, 77]. The concentration of absorbate can be changed by controlling the pressure in the vacuum chamber and by pre-treatment with high electric field. In this work, the FEE measurement was performed under different air pressure to investigate the influence of pressure on the FEE properties of diamond nanocomposite films. As shown in Figure 4-12, with the increase of pressure, the turn-on electric field increases from 6 V/μm at 10^{-7} Torr to 8 V/μm at 10^{-5} Torr, and further to 12 V/μm at 10^{-3} Torr. The emission current decreases as the pressure increases. At the electric field

of 18 V/μm, the emission current at 10^{-5} Torr drops to 70 % of the emission current at 10^{-7} Torr. When the pressure increases further to 10^{-3} Torr, the emission current is only 5% of the emission current at 10^{-7} Torr. The pressure dependence of the emission current may be attributed to the absorbates on the surface of the samples and, to a lesser extent, to electron collisions with air molecules.

The F-N plots measured at three different pressures are presented in Figure 4-13. The field enhancement factor can be calculated by linear fitting of F-N plots. Assuming that the work function of the diamond nanocomposite film is 5 eV, the calculated FEF of the film at 10^{-7} Torr is 159, and the corresponding effective emission area is 7×10^{-4} μm^2, which is similar to that of diamond coated silicon emitter (10^{-4} – 10^{-3} μm^2) and much larger than that of the uncoated silicon emitters (10^{-8} μm^2).

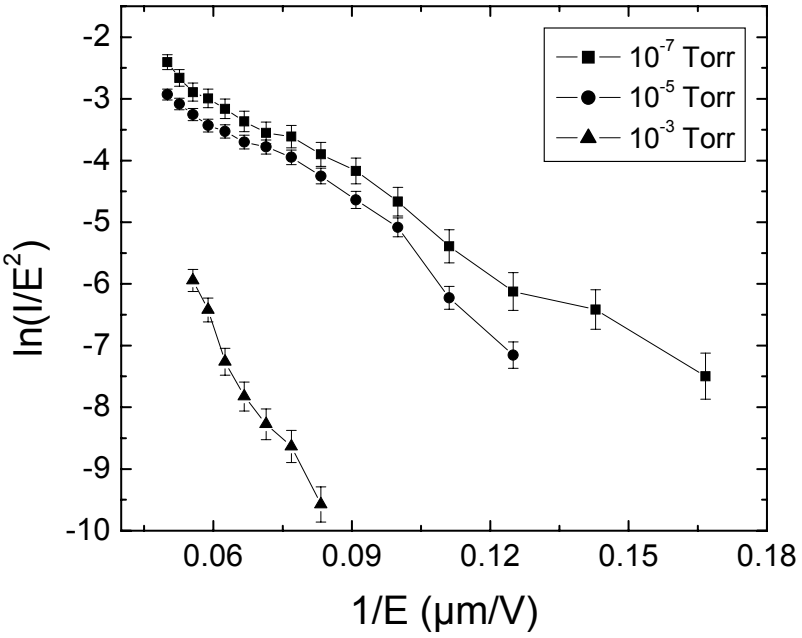

Figure 4-13: field electron emission F-N plots of diamond nanocomposite film at different pressures.

As seen in Figure 4-13, the F-N plot at 10^{-7} Torr has a slope similar to that at 10^{-5} Torr. Linear fitting results show that the field enhancement factors of the nanocomposite film at 10^{-7} Torr and at 10^{-5} Torr are 159 and 140, respectively, indicating that the pressure has little influence on the field electron emission properties of the films when the pressure is lower than 10^{-5} Torr. However, the F-N plot at a

higher pressure of 10^{-3} Torr is quite different from the plots at the lower pressures. The corresponding field enhancement factor is only 55. Some typical field electron emission parameters of the nanocomposite film are summarized in Table 4-3.

Table 4-3: Typical field electron emission parameters of diamond nanocomposite film at different pressures.

Pressure	10^{-7} Torr	10^{-5} Torr	10^{-3} Torr
Turn-on electric field	6 V/μm	8 V/μm	12 V/μm
Emission current at 18 V/μm	18 μA	12.48 μA	0.85 μA
Field enhancement factor	159	140	55

4.3.3 Conclusion

Diamond nanocomposite films have been synthesized by growing a nanocrystalline diamond layer on top of a layer of diamond nanocone film. Many sharp protrusions on the surface of the film make it suitable for field electron emission. Compared with diamond nanocones, the diamond composite films exhibit lower turn-on electric field and larger emission current. The influence of air pressure on the field electron emission properties of diamond nanocomposite films was also investigated. At the chamber pressure of 10^{-7} Torr, the nanocomposite film exhibits a low turn-on field of 6 V/μm and a strong emission current of 36 μA at the electric field of 20 V/μm. When the air pressure increases from 10^{-7} Torr to 10^{-5} Torr, a 30% current drop and very similar field electron emission F-N plots were observed.

Chapter 5

Field Electron Emission Characteristics of Diamond Films: Influence of sp^2 Phase Concentration

The sp^2 phase plays an important role in the field electron emission of diamond films. In fact, one of the possible routes for increasing the field electron emission capacity of diamond films is to increase the sp^2 phase concentration in the diamond grain boundary region, as it has been proposed that grain boundaries of diamond films are sp^2-bonded and the grains are sp^3-bonded. The sp^2-bonded regions are of low electrical resistivity and act as an electron transport path, which facilitates the electron field emission properties [78]. Until now, techniques still need to be developed to control the sp^2 phase concentration. In this Chapter, several methods utilized to control the sp^2 phase concentration in diamond films are described. The effect of the sp^2 phase concentration on the field electron emission property of diamond films is also presented and discussed.

5.1 Control of sp^2 Phase Concentration in Diamond Films Deposited Using H_2 and CH_4

Deposition conditions have significant influence on the growth of diamond films. Among all the important processing parameters utilized in the microwave plasma enhanced CVD growing process, the methane concentration and bias voltage are observed to influence the nucleation behaviour of diamond films most prominently. By varying these two parameters, diamond films with different grain size and sp^2 phase concentrations can be obtained. In this experiment, different diamond films were

synthesized by varying the methane concentration and substrate bias voltage. The effects of growth parameters on the grain size and sp^2 phase concentration of the films are systematically studied. These characteristics are then correlated with the field electron emission properties of the diamond films.

5.1.1 Sample Preparation

The diamond films were grown in the microwave plasma enhanced CVD reactor on p-type mirror-polished Si (100) substrates. The substrate was immersed in methane and hydrogen plasma. Three sets of diamond films were synthesized by varying the methane concentration and substrate bias voltage. The first sets of diamond films were deposited at various methane concentrations (1%, 5%, 10%, 20% and 50%) without applying substrate bias voltage. The second sets of deposition experiments were performed at different methane concentrations (1%, 10%, 20% and 50%) with a -250 V bias voltage. In order to investigate the influence of substrate bias voltage, the third sets of diamond films were synthesized using 1% methane concentration under different continuous negative bias voltages (-50 V, -100 V, -150 V and -200 V). The deposition time for all diamond films was 7 hours.

5.1.2 Results and Discussion

5.1.2.1 Diamond Films Deposited Under Different CH_4 Concentrations Without Substrate Bias Voltage

The typical microstructures of the diamond films grown using different CH_4 concentrations without substrate bias voltage are shown in Figure 5-1. With the increase of CH_4 concentration from 1% to 5%, 10%, 20% and 50%, the diamond grain sizes are decreased. Raman spectra of these films are shown in Figure 5-2 and are very similar, except that the ratio of the sp^3 phase (1332 cm^{-1} peak) to the sp^2 phase (1480 cm^{-1}) is decreased with the increase of CH_4 concentration.

While the methane concentration in the reaction chamber imposes a significant influence on the SEM granular structure and Raman resonance characteristics of the diamond films, it also shows marked effects on the field electron emission properties

of the films. Figure 5-3 shows the field electron emission *I-E* curves and F-N plots of diamond films deposited at different CH_4 concentrations (1%, 5%, 10%, 20% and 50%) without bias voltage. Some typical field electron emission parameters are listed in Table 5-1. It can be found that the field electron emission for the diamond films synthesized using 1% CH_4 can be turned on at 20 V/μm and the emission current can reach 0.12 μA at 26 V/μm. With the increase of methane concentration, the field electron emission performances of diamond films were improved. The turn-on fields were lowered down to 16 V/μm, 14 V/μm, 10 V/μm and 6 V/μm for the diamond films synthesized using the CH_4 concentration of 5%, 10%, 20% and 50%, respectively.

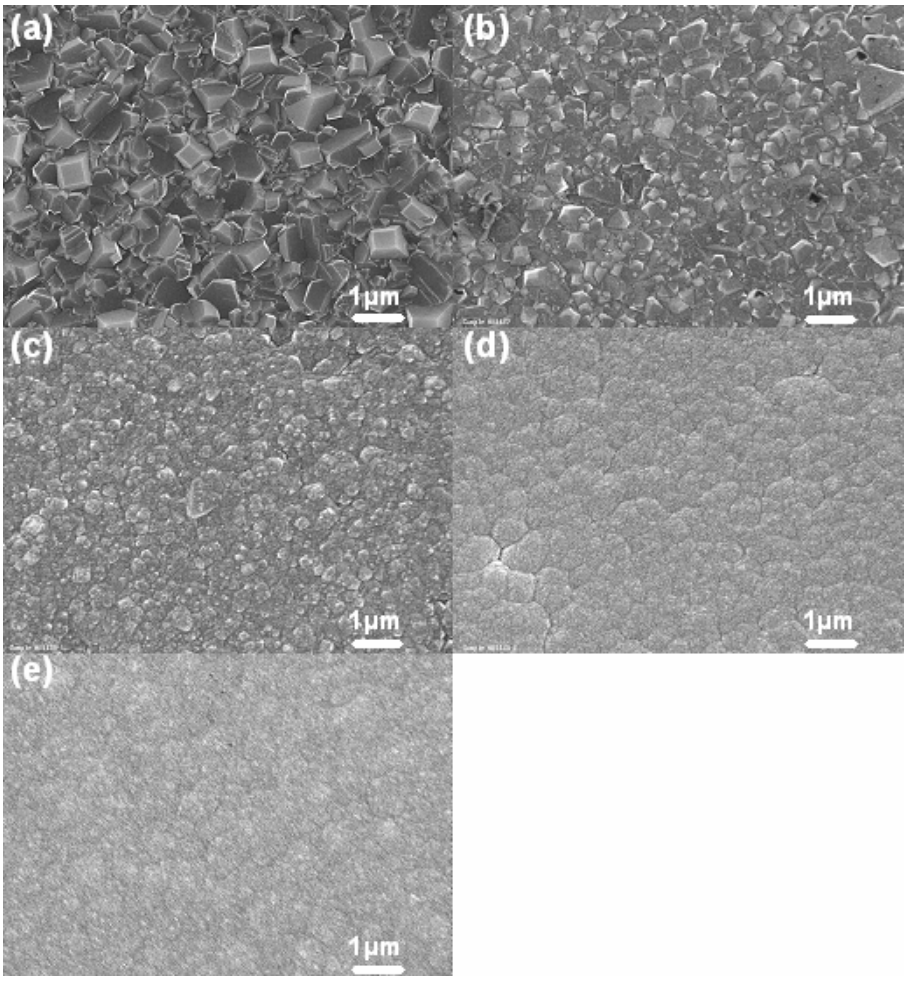

Figure 5-1: Typical SEM micrographs of diamond films grown under different CH_4 concentration without substrate bias voltage: (a) 1 % CH_4, (b) 5 % CH_4, (c) 10 % CH_4, (d) 20 % CH_4, and (e) 50 % CH_4.

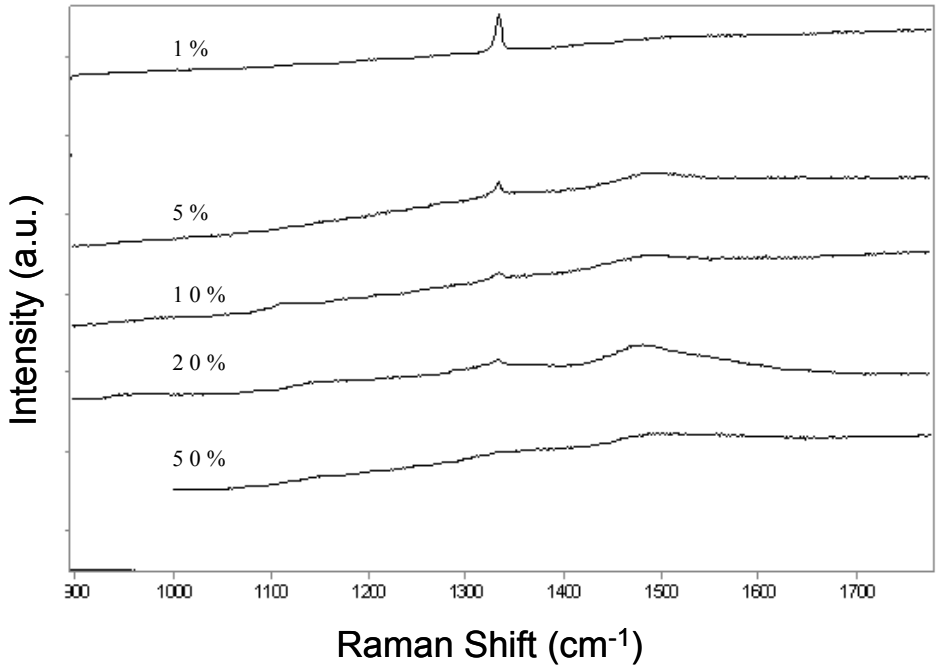

Figure 5-2: Raman spectra of diamond films deposited under different CH_4 concentration without substrate bias voltage.

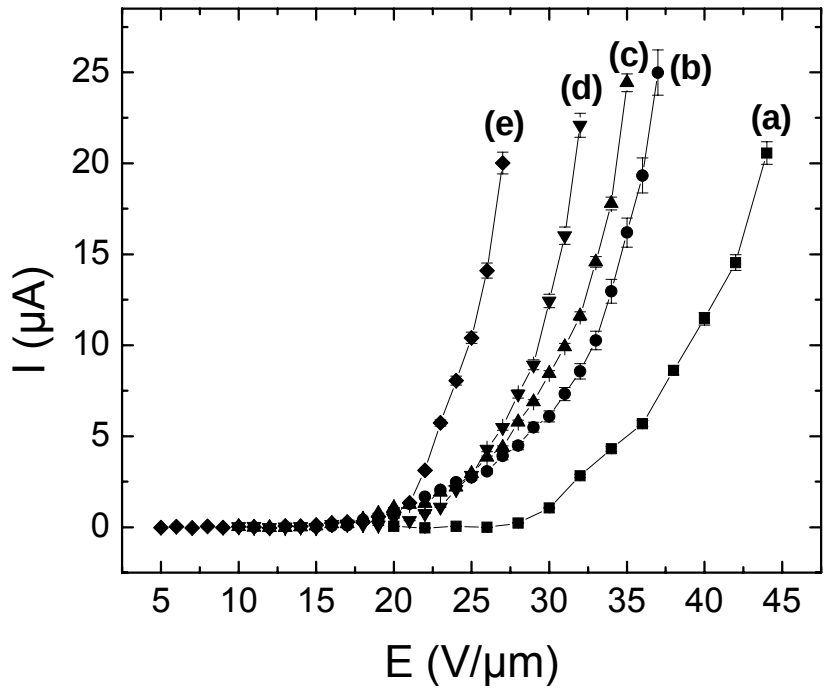

Figure 5-3: field electron emission *I-E* curves of diamond films deposited under different CH_4 concentration without substrate bias voltage: (a) 1 % CH_4, (b) 5 % CH_4, (c) 10 % CH_4, (d) 20 % CH_4, and (e) 50 % CH_4.

Table 5-1: Typical field electron emission parameters of diamond films deposited under different conditions.

Sample	CH_4 concentration	Bias voltage	Turn-on field (V/μm)	Emission current (μA)
01	1 %	0	20	0.12 μA at 26 V/μm
02	5 %	0	16	3.08 μA at 26 V/μm
03	10 %	0	14	2.85 μA at 26 V/μm
04	20 %	0	10	4.28 μA at 26 V/μm
05	50 %	0	6	14.1 μA at 26 V/μm
06	1%	-250 V	26	0.02 μA at 30 V/μm
07	10%	-250 V	25	0.4 μA at 30 V/μm
08	20%	-250 V	20	2.04 μA at 30 V/μm
09	50%	-250 V	14	16.9 μA at 30 V/μm
10	1 %	-50 V	15	0.04 μA at 20 V/μm
11	1 %	-100 V	14	2.68 μA at 20 V/μm
12	1 %	-150 V	20	0.01 μA at 20 V/μm
13	1 %	-200 V	10	5.34 μA at 20 V/μm

5.1.2.2 Diamond Films Deposited Under Different CH_4 Concentrations With -250 V Substrate Bias Voltage

To further improve the field electron emission properties of diamond films, a -250 V bias voltage was applied to the substrate when the methane concentration was varied. Figure 5-4 shows the typical SEM micrographs of the films. Compared with the diamond films deposited using the same CH_4 concentration but without bias voltage, the diamond films deposited with bias voltage exhibit smaller grain sizes, suggesting that the nucleation rate can be increased by applying bias voltage to the substrate. The bias voltage can increase the kinetic energy for the C^+ species, which is expected to enhance the formation of sp^3 C-C bonds. The bias enhanced nucleation technology has been used widely in diamond deposition [79-82].

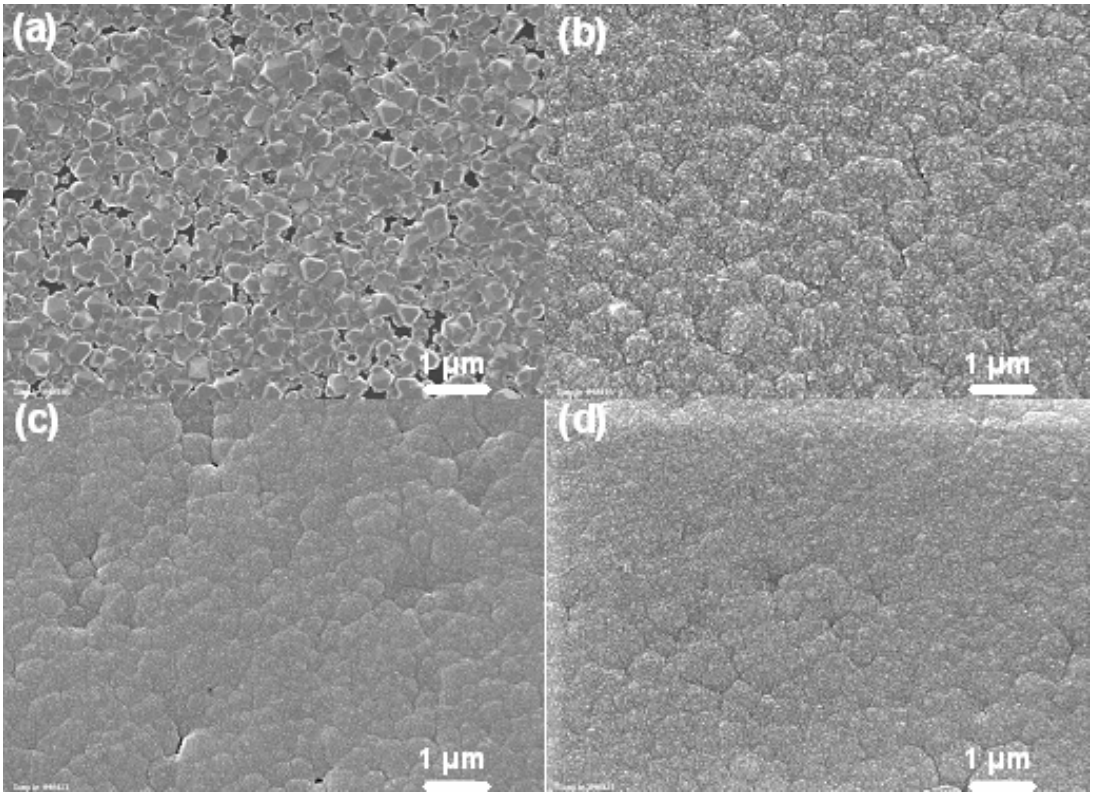

Figure 5-4: Typical SEM micrographs of diamond films grown under different CH_4 concentration with -250 V substrate bias voltage: (a) 1 % CH_4, (b) 10 % CH_4, (c) 20 % CH_4, and (d) 50 % CH_4.

Figure 5-5 shows the corresponding Raman spectra of diamond films deposited using different methane concentrations and with a -250 V bias voltage. Similarly, the ratio of sp^3 phase to sp^2 phase is decreased with the increase of CH_4 concentration. For the diamond films synthesized using methane concentrations of 20% and 50%, very diffuse resonance peaks in the vicinity of 1150 cm^{-1} (D^*), 1332 cm^{-1} (D), and 1580 cm^{-1} (G) can be observed, which is similar to the Raman spectra for nanodiamond films reported in the literature [83, 84].

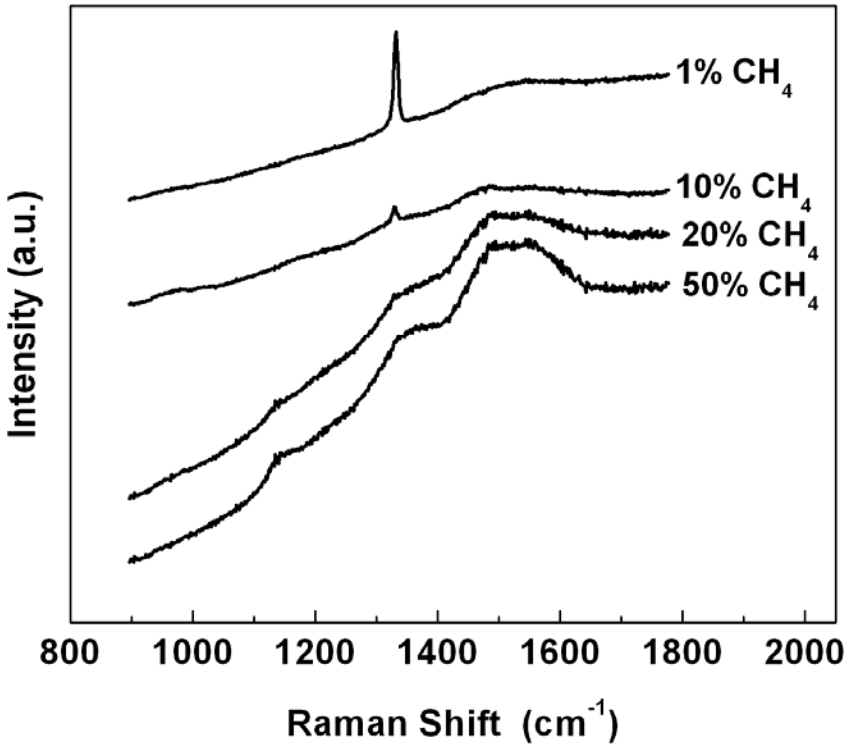

Figure 5-5: Raman spectra of diamond films grown under different CH_4 concentration with -250 V substrate bias voltage.

The field electron emission *I-E* curves of as-grown diamond films are shown in Figure 5-6. It was observed that the field electron emission properties were improved with the increased methane concentration during the deposition process, which is the same as the above diamond films synthesized using different CH_4 concentrations but without applying substrate bias voltages. The field electron emission turn-on electric fields are decreased from 26 V/μm to 25 V/μm, 20V/μm, and then to 14V/μm. The corresponding emission current at the electric field of 30 V/μm is increased from 0.02 μA to 0.4 μA, then to 2.04 μA, and finally to 16.9 μA. On the other hand, compared with the diamond films synthesized without applying bias voltage, the field electron emission properties were degraded, which can be attributed to the etching effect of H^+ species under strong electric field. Although the comparison between Figure 5-1 and Figure 5-4 shows that the grain size becomes much smaller when applying substrate bias voltage during deposition, the etching effect of H^+ ions will decrease the sp^2 phase

concentration in the diamond films, which will decrease the electron transport ability of diamond grain boundaries and so decrease the emission current.

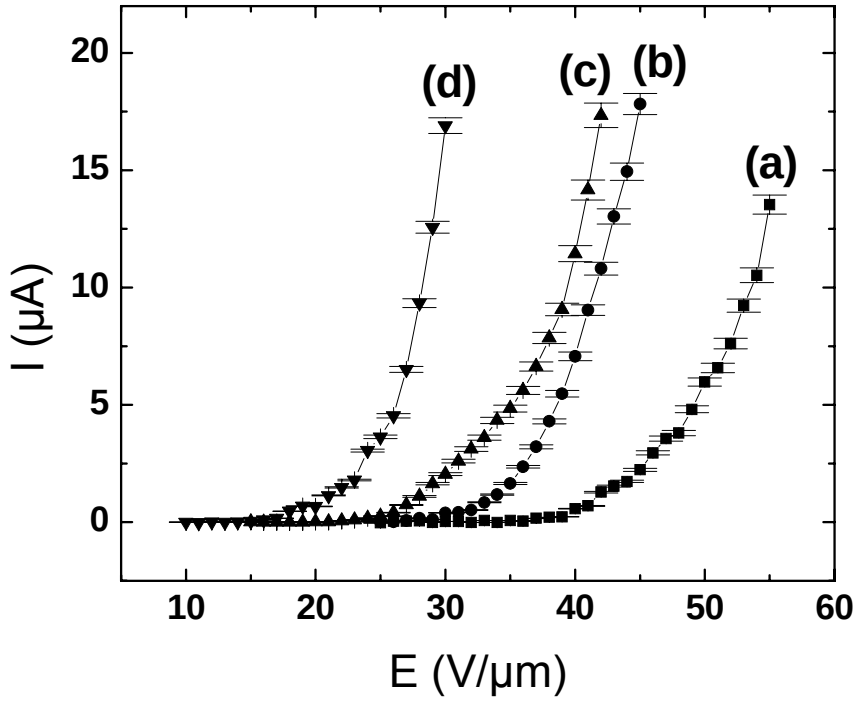

Figure 5-6: field electron emission *I-E* curves of diamond films deposited under different CH_4 concentration with -250 V substrate bias voltage: (a) 1 % CH_4, (b) 10 % CH_4, (c) 20 % CH_4, and (d) 50 % CH_4.

5.1.2.3 Diamond Films Deposited Using 1 % CH_4 With Different Substrate Bias Voltages

To investigate the influence of bias voltage on the diamond growth and field electron emission properties, diamond films were synthesized using 1% CH_4 but with different substrate bias voltages including -50 V, -100 V, -150 V and -200 V. Figure 5-7 shows the typical SEM micrograph of diamond films. Contrary to the phenomenon that the CH_4/H_2 ratio markedly alters the grain size and morphology of the diamond films, the bias voltage shows essentially no influence on the grain size of the diamond films.

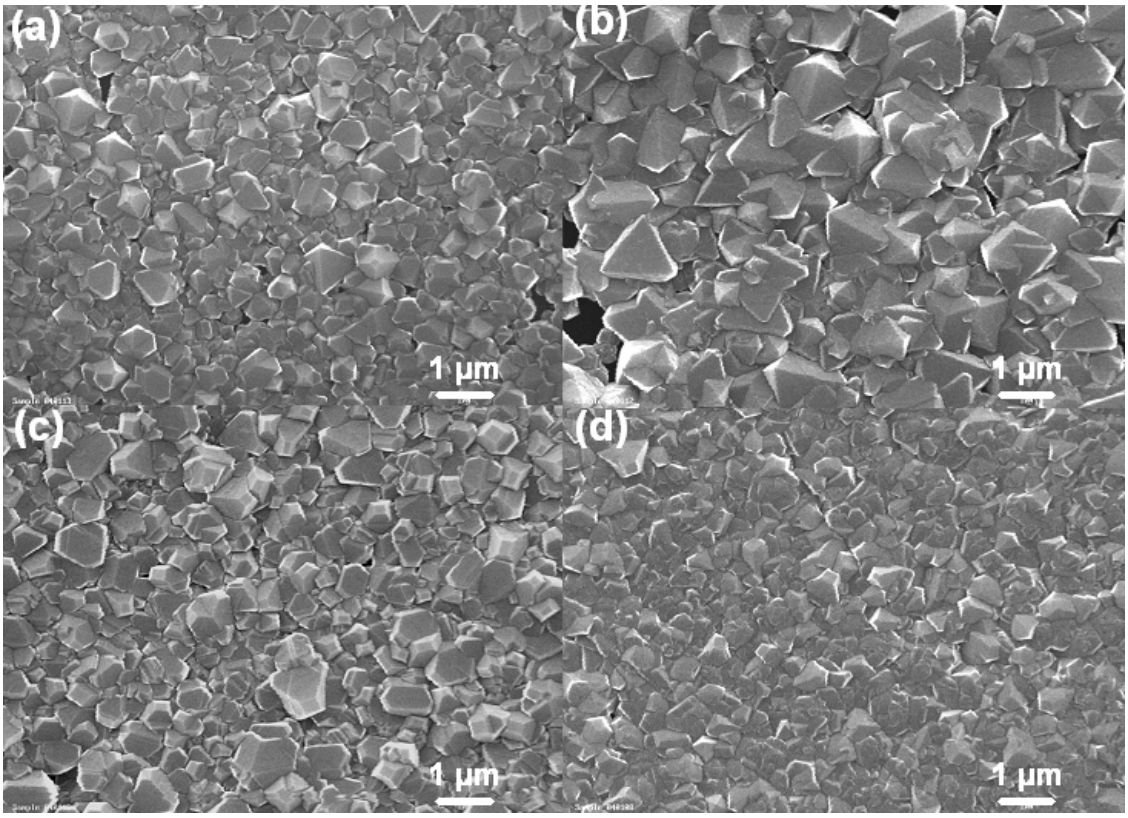

Figure 5-7: Typical SEM micrographs of diamond films grown using 1 % CH_4 with different substrate bias voltage: (a) -50 V, (b) -100 V, (c) -150 V, and (d) -200 V.

No obvious sp^2 C-C peaks are observed from the corresponding Raman spectra. On the other hand, the very sharp sp^3 C-C peaks at 1332 cm^{-1} indicate that these deposited diamond films are almost pure diamond. The nucleation and growth mechanism for diamond films due to applied bias voltages is not obvious. Presumably, the bias voltage not only increases the kinetic energy for the C^+ species, which is expected to enhance the formation of sp^3 C-C bonds, but also raises the bombardment energy of H^+ species, which will increase the etching rate for the freshly formed C-C bonds including sp^3 C-C and sp^2 C-C bonds. Moreover, the H^+ etching rate for sp^3 C-C is much smaller than that of sp^2 C-C bonds due to the difference in the bond strength. Under the action of bias voltage, most sp^2 C-C bonds are etched away and most sp^3 C-C bonds remain intact. This is in accordance with the observed SEM micrographs and Raman spectra.

The field electron emission *I-E* curves for these films are shown in Figure 5-8. Some typical field electron emission parameters are listed in Table 5-1. It can be found that the bias voltage modifies the electron field emission properties of the diamond films less significantly than the methane concentration does. On one hand, compared with the diamond film deposited using 1% CH_4 but without bias voltage, the field electron emission properties were enhanced by the applied bias voltage. But the enhancement is not as significant as that induced by the increase of methane concentration. On the other hand, the influence of bias voltage on the field electron emission properties is not monotonic. For the – 50 V bias voltage deposited diamond film, the field electron emission was turned on at an applied field of 15 V/μm and reached an emission current of 0.04 μA at 20 V/μm. When the bias voltage is increased to -100 V, the turn on electric field remains the same, but the emission current was enhanced to 2.68 μA at 20 V/μm. For a higher bias voltage of -150 V, the field electron emission was degraded significantly with an emission current of 0.01 μA at 20 V/μm. At larger applied bias voltage of -200 V, the field electron emission property was enhanced significantly (with the turn on electric field of 10 V/μm and the emission current of 5.34 μA at 20 V/μm). This can be mainly attributed to the etching effect of H^+ ions under applied electric field, which will decrease the sp^2 phase concentration in the diamond grain boundaries and so decrease the field electron emission properties.

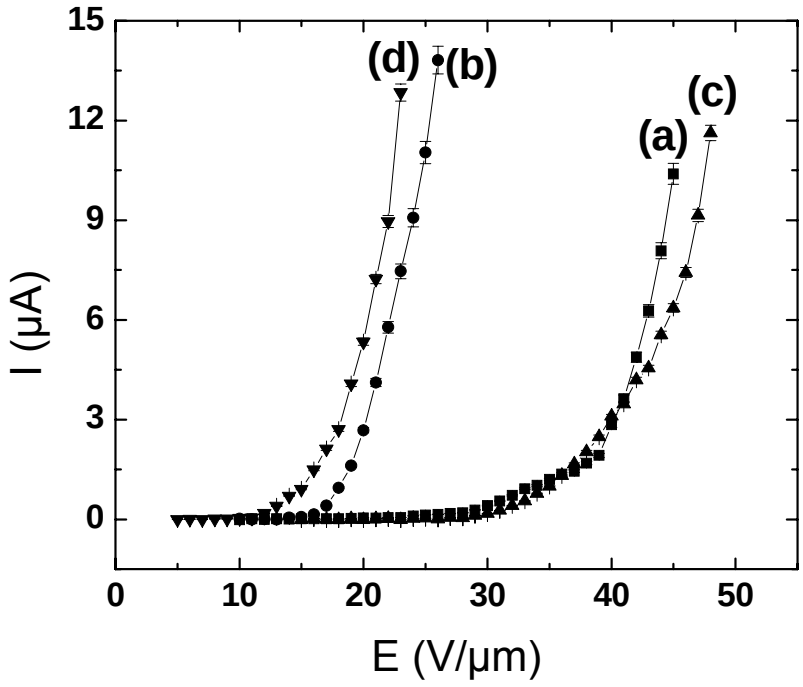

Figure 5-8: Field electron emission *I-E* curves of diamond films deposited using 1 % CH_4 with different substrate bias voltage: (a) -50 V, (b) -100 V, (c) -150 V, and (d) -200 V.

Above mentioned results indicate that although the SEM granular structure and Raman crystal structure of these diamonds are very much alike, the deposition parameters such as methane concentration and substrate bias voltage do impose pronounced influences on the field electron emission characteristics of the diamond films. The modification on the field electron emission characteristics of the diamond films can be attributed to the change in the grain size and the sp^2 phase concentration. By increasing the methane concentration and bias voltage, diamond films with small grain size were synthesized. The large proportion of grain boundaries is the main reason resulting in the improved field electron emission. However, the applied bias voltage will also increase the etching rate of H^+ ions on the diamond films and so decrease the sp^2 phase concentration. Thus, too strong bias voltage will degrade the field electron emission properties of diamond films.

5.1.3 Conclusion

The microstructure and field emission characteristics of diamond films are strongly correlated with the deposition conditions including the methane concentration and the substrate bias voltage. Compared with the bias voltage, the methane concentration shows more prominent effects on the grain structure of the diamond films. The field electron emission properties of the diamond films are markedly enhanced as the methane concentration increases for both cases: with –250 V biasing and without biasing. The main factor modifying the field electron emission properties is related to the increase in the proportion of sp^2-bonded grain boundaries due to the decrease of diamond grain size with the increase of methane concentration. The bias voltage exhibits nonmonotonic influences on the field electron emission properties of diamond films. This can be attributed to the two opposite influences of substrate bias voltage. On one hand, the increased bias voltage can enhance the nucleation of diamond films and so decrease the grain size, which will in turn enhance the field electron emission. On the other hand, the increased substrate bias voltage will also enhance the etching rate of sp^2 phase by H^+ ions in the plasma and so decrease the sp^2 phase concentration in the films, which will degrade the field electron emission from diamond films.

5.2 Control of sp^2 Phase Concentration in Diamond Films Deposited Using Graphite Etching

In conventional diamond synthesis, hydrogen mixed with hydrocarbon gas has been widely used [85-87]. However, in these methods, a substrate temperature above 700 ^{0}C is required for the synthesis of high quality diamond films with reasonably high growth rate. Therefore substrates that melt or undergo problematic phase transitions at such high temperatures cannot be employed. Removing this limitation by decreasing the synthesis temperature would significantly expand the field electron emission applications of diamond films. In the experiment, a novel deposition method of diamond films on Si substrate with a high growth rate using graphite etched by hydrogen as a carbon source in a hot filament chemical vapor deposition reactor without plasma discharge [88, 89] and in a microwave plasma reactor [89] was

developed. High quality diamond films have been deposited at temperatures as low as 250 ˚C using this method. The advantages of the new process over the conventional methods using an H_2+ 1% CH_4 gas mixture include deposition at lower temperature, higher growth rate, and reduced carbon soot contamination to the deposition system [89].

In order to optimize diamond film growth through graphite etching and improve the field electron emission properties of the as-grown diamond films, the effects of the hydrogen flow rate on the growth rate and morphology of diamond were investigated systematically in this experiment. These surface properties were then correlated with the field electron emission properties of the deposited diamond films.

5.2.1 Sample Preparation

Diamond deposition experiments were conducted in a microwave plasma-enhanced CVD reactor filled with hydrogen. The p-type (100)-oriented mirror polished Si wafers with a thickness of 0.65 mm were used as substrates. A 1 mm thick isotropic polycrystalline graphite sheet (Poco's EDM-3) was placed beside the silicon substrate. The vacuum chamber was pumped down to a pressure of 1.0×10^{-6} Torr using a turbo-molecular pump backed by a roughing pump. In order to get a high nucleation density of diamond, the silicon substrates were ultrasonically scratched in a solution containing diamond powder. The substrate temperature was measured with a thermocouple mounted right behind the substrate holder. When the working pressure was stabilized at 30 Torr, a 2.45 GHz microwave source was switched on to produce a hydrogen plasma. The microwave power, substrate temperature and working pressure were fixed at 1000 W, 520 ˚C and 30 Torr, respectively. The hydrogen flow rate was varied from 500 sccm to 1 sccm. The deposition time of the samples was 7 hours. In this process, almost no carbon soot was formed in the deposition system because hydrocarbon was only formed locally from graphite etched by hydrogen, which significantly reduced carbon contamination of the deposition system, compared with the conventional methods. In order to compare the samples grown using a conventional gas mixture of methane and hydrogen, diamond thin films were also

grown using a gas mixture of 1% CH_4 + 99% H_2 under similar conditions without graphite inside the reaction chamber.

5.2.2 Results and Discussion

The surface morphologies of diamond films deposited with different hydrogen flow rates from 500 sccm to 1 sccm were characterized using SEM. Figure 5-9 shows the typical plane-view SEM images of diamond films grown for 7 hours with hydrogen flow rates of 500 sccm, 300 sccm, 90 sccm, 30 sccm, 10 sccm, and 1 sccm, respectively. As shown in Figure 5-9a, with a flow rate at 500 sccm, diamond nucleation density is very low, and only separate diamond particles are formed. The average diamond particle size is around 100 nm, thus the average diameter growth rate of diamond particles is very low (14 nm/h). When the flow rate decreases to 300 sccm (Figure 5-9b), both diamond nucleation density and growth rate increase. Diamond particles start to coalesce. The average diamond particle size increases to 300 nm, increasing their average diameter growth rate to 43 nm/h, three times higher than films grown with a flow rate at 500 sccm. With further decrease in the flow rate to 90 sccm (Figure 5-9c), nearly continuous diamond films were formed with an average grain size of approximately 400 nm. When the flow rate was below 90 sccm (Figure 5-9d-f), denser, continuous diamond films were obtained. The average grain size increases with decreasing flow rate, peaks at a flow rate of 50 sccm, but decreases with further decrease of the hydrogen flow rate. Nanocrystalline diamond films are obtained when the flow rate was 3 sccm or lower. The thickness measurement from cross-section SEM images indicates that the diamond film growth rate increases significantly with decreasing hydrogen flow rate. The diamond film growth rate increases from 3 nm/h at 500 sccm to 2.1 μm/h at 1 sccm.

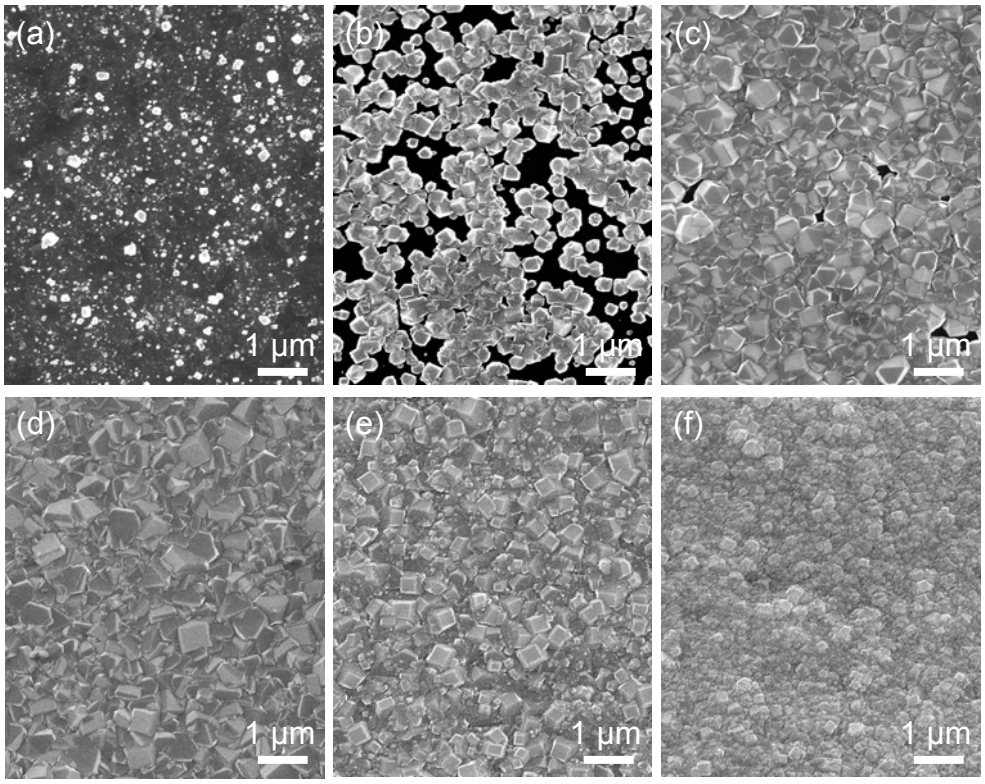

Figure 5-9: Plan-view SEM morphologies of diamond films grown with different hydrogen flow rates of (a) 500 sccm, (b) 300 sccm, (c) 90 sccm, (d) 30 sccm, (e) 10 sccm and (f) 1 sccm.

For comparison, diamond films were deposited under similar conditions using a conventional H_2 + 1% CH_4 gas mixture (without graphite inside the reaction chamber) with different gas flow rates. Diamond growth rates were similar when total gas flow rate varied from 10 sccm to 500 sccm. The average film growth rate is around 0.3 μm/h, 3 to 7 times lower than that of the films synthesized through graphite etching at a flow rate of 30 to 1 sccm. These results show that the method based on graphite etching significantly enhances diamond growth rate. Furthermore, the crystallite size in the film with low flow rates is more than one order of magnitude smaller than that of the film deposited by a gas mixture of 1% CH_4 + 99% H_2. This is attributed to the production of activated hydrocarbon radicals formed through in-situ etching of graphite by hydrogen.

Figure 5-10 shows Raman spectra of the diamond films deposited at different hydrogen flow rates described in Figure 5-9. A clear Raman phonon peak around 1332 cm^{-1}, characteristic of diamond phase, is observed in all the spectra. The broad peak at

around 1582 cm^{-1} (G-band) corresponds to sp^2-bonded carbon. Considering the fact that Raman scattering in the visible range (514 nm) is up to 50 times more sensitive to sp^2-bonded carbon than sp^3-bonded carbon, the sp^2 bonded carbon concentration in all the films is quite low. With the decrease of hydrogen flow rate, the diamond peak at 1332 cm^{-1} decreases in intensity and increases in width. The G-band Raman scattering signal increases with the decreasing hydrogen flow rate, indicating diamond films with more sp^2- bonded carbon were deposited. Thus, the hydrogen flow rate played an important role in affecting the Raman characteristics of the diamond films. For quantitative comparison of the concentration of sp^2- and sp^3- bonded carbon in the films, the integrated intensity ratio of the G-band to the diamond peak (I_G/I_D) is estimated from the Raman spectra. The dependence of I_G/I_D on the hydrogen flow rate is depicted in Figure 5-11b. With the decrease of hydrogen flow rates from 50 sccm to 30 sccm, then to 10 sccm, and finally to 1 sccm, the I_G/I_D ratio is shifted from approximately zero to 0.43, 0.98, and then to 1.08, respectively. Compared with the Raman spectra taken from samples synthesized using a conventional gas mixture of 1% CH_4 + 99% H_2 (not shown), the diamond quality in these films shows no significant degradation.

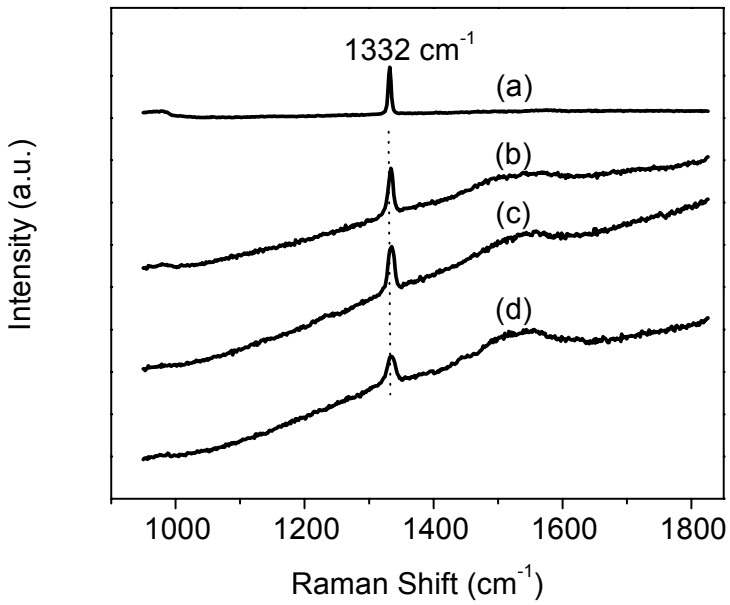

Figure 5-10: Raman spectra of diamond films deposited under different H_2 flow rates: (a) 50 sccm, (b) 30 sccm, (c) 10 sccm, and (d) 1 sccm.

Figure 5-11 summarizes the dependence of the diamond grain sizes (Figure 5-11a), the I_G/I_D ratios (Figure 5-11b), and the film growth rates (Figure 5-11c) on the hydrogen flow rates (ranging from 50 sccm to 1 sccm) for the synthesized continuous films. With decreasing hydrogen flow rate, the grain size decreases, whereas the sp^2–bonded carbon concentration and the growth rate increases.

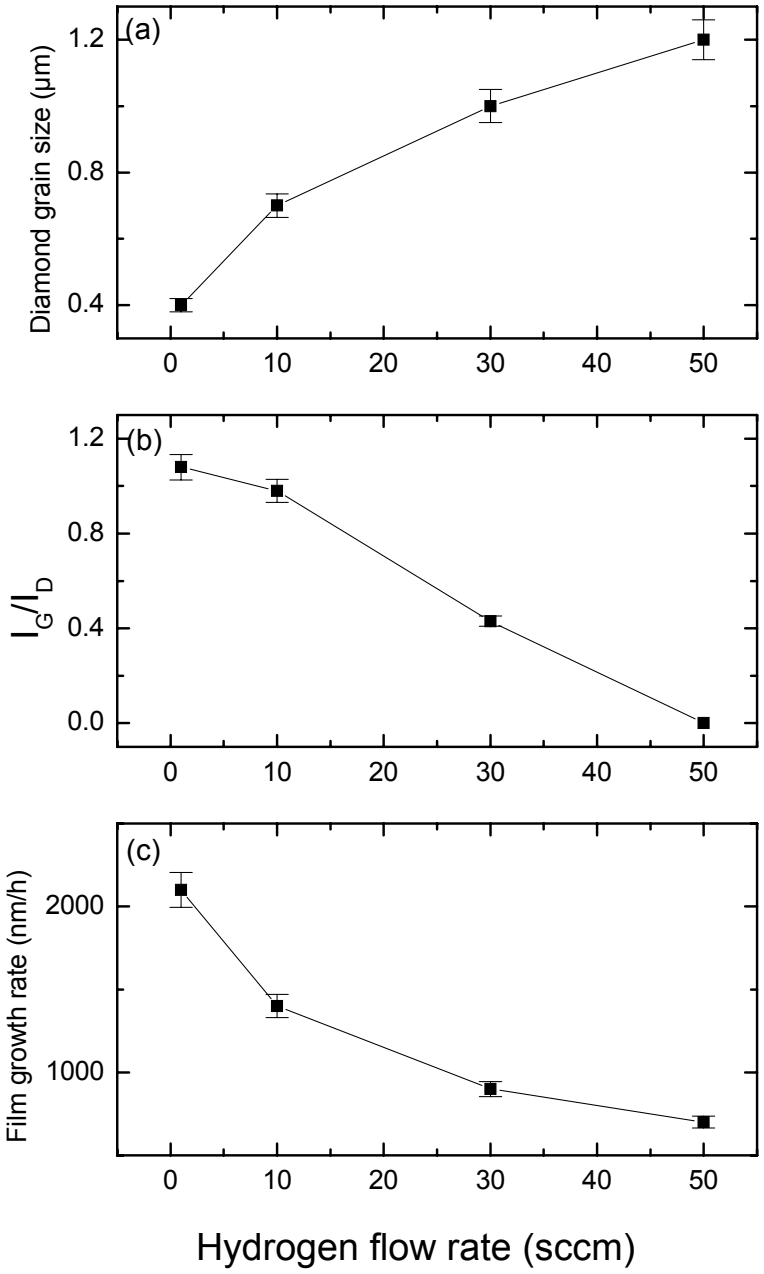

Figure 5-11: The dependence of (a) diamond grain size, (b) I_G/I_D ratio, and (c) film growth rate on the hydrogen flow rate.

Figure 5-12 shows the field electron emission $I-E$ curves of the deposited diamond films. Samples prepared at lower hydrogen flow rate show lower turn-on electric field (defined by the electric field at which the emission current reaches 0.01 μA). Also the emission current increases at higher flow rates. For the diamond film grown at the hydrogen flow rate of 50 sccm, the largest turn-on electric field of 19 V/μm and the largest emission current of 0.2 μA at the electric field of 20 V/μm were obtained. With the decrease of the hydrogen flow rates from 50 sccm to 30 sccm, then to 10 sccm, and finally to 1 sccm, the diamond films exhibited decreased turn-on electric fields of 15 V/μm, 12 V/μm, and 6 V/μm. The corresponding emission current at 20 V/μm increases to 1.9 μA, 13.2 μA, and 36.7 μA, respectively. The dependence of the changes of field electron emission parameters including the turn-on electric field and the emission current at the electric field of 20 V/μm are depicted in Figure 5-13.

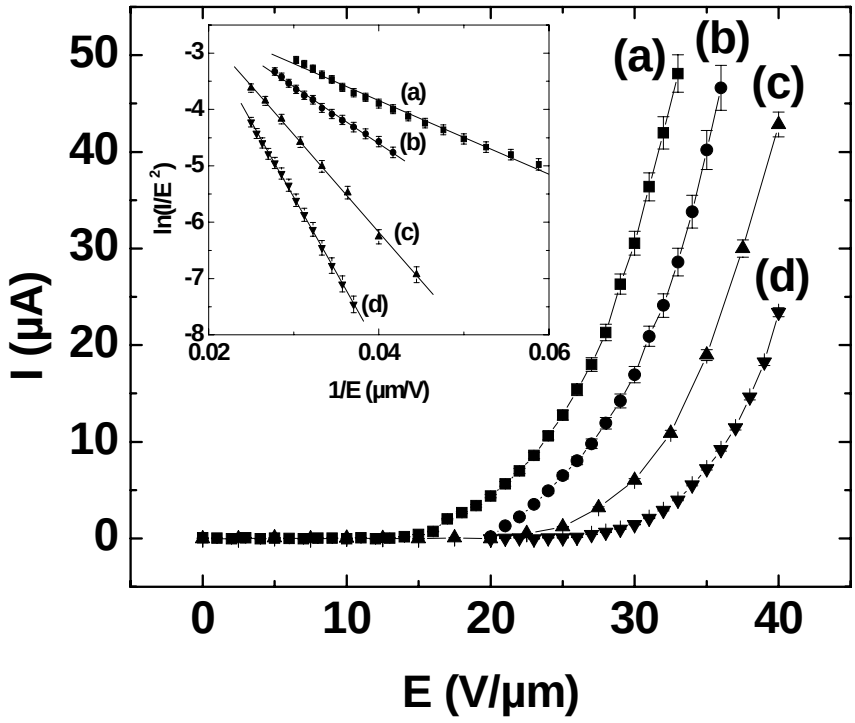

Figure 5-12: FEE *I-E* curves and F-N plots (inset) of diamond films deposited under different H_2 flow rates: (a) 1 sccm, (b) 10 sccm, (c) 30 sccm, and (d) 50 sccm.

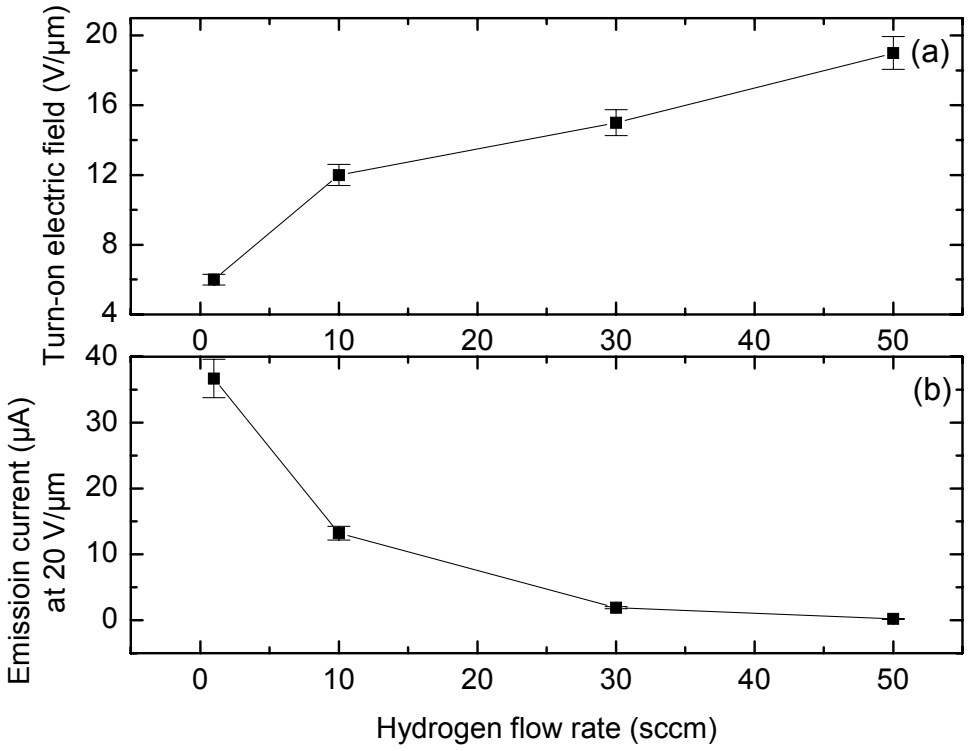

Figure 5-13: The dependence of (a) turn-on electric field (V/μm) and (b) emission current (μA) at 20 V/μm on the hydrogen flow rate.

The Fowler-Nordheim (F-N) plot corresponding to the field electron emission $I-E$ curve for each sample is depicted in the inset of Figure 5-12. Each F-N plot can be fitted into a straight line, supporting the electron emission through the tunneling mechanism. The F-N plot feature is characterized by the field enhancement factor and the effective emission area, which can be obtained through linear fitting. According to the Fowler-Nordheim (F-N) field electron emission theory, the emission current related to the applied electric field is given as

$$\ln(I/E^2) = \ln[A\alpha\beta^2/(\phi/e)] - B(\phi/e)^{\frac{3}{2}}/(\beta E). \quad (5\text{-}1)$$

By linear fitting, the field enhancement factor and the effective emission area can be calculated from the intercept

$$a = \ln\left(\frac{A\alpha\beta^2}{\phi/e}\right), \quad (5\text{-}2)$$

and the slope

$$b = -\frac{B(\phi/e)^{\frac{3}{2}}}{\beta} \tag{5-3}$$

of the F-N plot.

In order to calculate the field enhancement factor β and the effective emission area α, the work function should be known. For diamond, a work function of 4 eV to 5 eV has been used by other authors [58, 59]. An alternative treatment of the uncertain work function is presented below.

From Equations 5-2 and 5-3, the field enhancement factor and the effective emission area can be expressed as functions of the work function:

$$\beta = -\frac{B}{b}\left(\frac{\phi}{e}\right)^{\frac{3}{2}} = -\frac{B}{b}\left(\frac{5}{e}\right)^{\frac{3}{2}}\left(\frac{\phi}{5}\right)^{\frac{3}{2}} = \beta_5(\phi_5)^{\frac{3}{2}}, \tag{5-4}$$

$$\alpha = \frac{b^2 e^a}{AB^2\left(\frac{\phi}{e}\right)^2} = \frac{b^2 e^a}{AB^2\left(\frac{5}{e}\right)^2\left(\frac{\phi}{5}\right)^2} = \frac{\alpha_5}{(\phi_5)^2}, \tag{5-5}$$

where $\beta_5 = -\frac{B}{b}\left(\frac{5}{e}\right)^{\frac{3}{2}}$ and $\alpha_5 = \frac{b^2 e^a}{AB^2(5/e)^2}$ are the field enhancement factor and effective emission area when a work function value of 5 eV is assumed for diamond films. $\phi_5 = \phi/5\text{eV}$ is the work function normalized to 5 eV. Figure 5-14 shows the fitted β_5 (Figure 5-14a) and α_5 (Figure 5-14b) values of diamond films deposited at different hydrogen flow rates. The actual β (α) value is above (below) the curve for $\phi > 5\text{eV}$ as indicated by Equations 5-4 (5-5) and depicted in Figure 5-14. The field enhancement factor increased from 360 to 530, 770, and then to 1100 when the hydrogen flow rate was decreased from 50 sccm to 30 sccm, 10 sccm, and 1 sccm. The corresponding effective emission areas are also increased from 2.5×10^{-6} μm^2 to 5.3×10^{-6} μm^2, 8.7×10^{-6} μm^2, and then to $1.1 \times 10^{-5} \mu m^2$. It has been found that both the field enhancement factor and the effective emission area increase with decreasing hydrogen flow rates if a constant work function value of 5 eV is assumed for all diamond films. Although a work function of 5 eV has been assumed to calculate the values of the field enhancement factor and the effective surface area, which are

displayed in Figure 5-14, the trend of the change of those values for the diamond films synthesized at the decreasing flow rates remains unchanged when the value of the work function is changed between 4 eV and 5 eV. Figure 5-15 further shows the ranges of the field enhancement factors (Figure 5-15a) and effective emission areas (Figure 5-15b) for the assumed work functions between 4 eV and 5 eV.

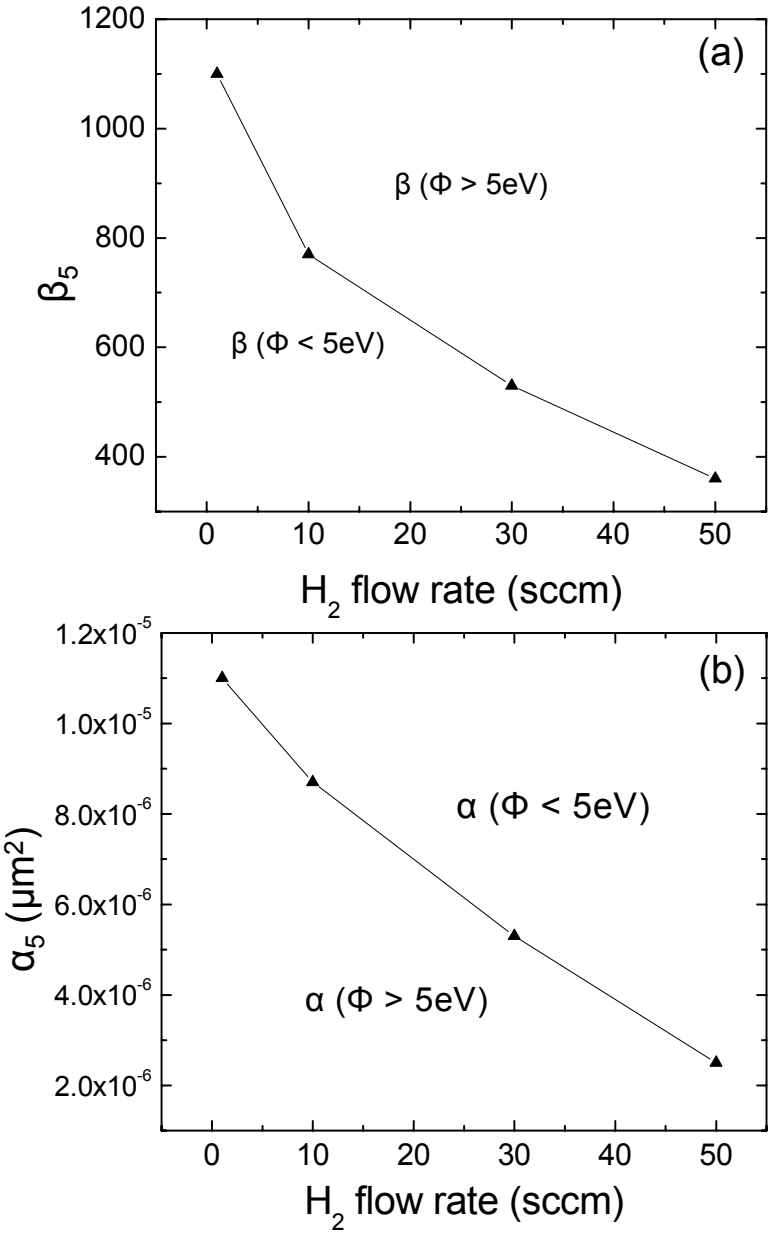

Figure 5-14: Field enhancement factors (a) and effective emission areas (b) calculated from the linear fitting of F-N plots by choosing the diamond work function as 5 eV.

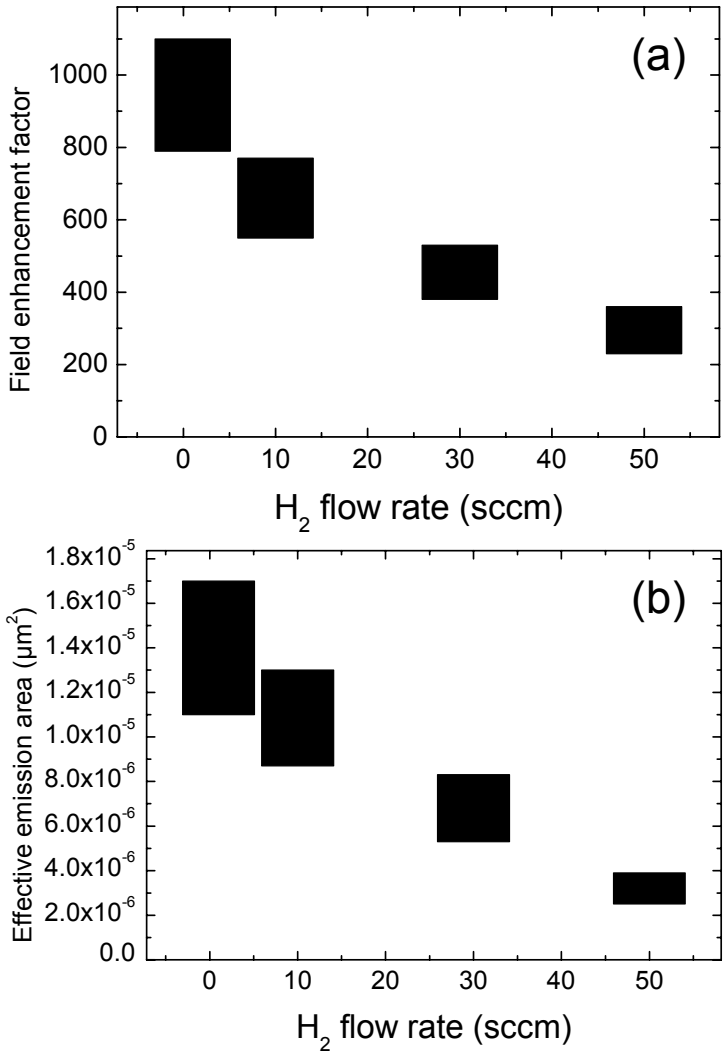

Figure 5-15: Influence of work function change on the linear fitting results of F-N plots.

The combined information shown in Figures 5-12, 5-14 and 5-15 indicate that the hydrogen flow rate has significant influence on the microstructure and chemical bonding of the diamond films, as well as on field electron emission properties. With the decrease in the hydrogen flow rate, the deposited diamond films exhibit lower turn-on electric field and larger emission current. The linear fitting results demonstrate that the field electron emission properties are enhanced by the increase in both the field enhancement factor and the effective emission area, which can be attributed to the increased sp^2 phase concentration in the diamond films.

5.2.3 Conclusion

The results presented in this experiment indicate that hydrogen flow rate is an important parameter influencing the growth of diamond thin films through graphite etching in a microwave plasma reactor. The growth rate and nucleation density of diamond films increase significantly with the decrease of hydrogen flow rate. The diamond films exhibit improved field electron emission characteristics when the hydrogen flow rate decreases. The main factors improving the field electron emission properties may be attributed to the increase of both the surface rms roughness and the sp^2-bonded carbon concentration in the diamond films. The increase in the sp^2 carbon concentration is caused by the decrease of diamond grain size and thus the increase in the grain boundary area, which contains the sp^2 carbon.

5.3 Control of sp^2 Phase Concentration in Diamond Films by Acid Treatment

All the above methods of adjusting the sp^2 phase concentration in diamond films are also accompanied by the change of the diamond grain size. In order to investigate the exact influence of sp^2 phase concentration on field electron emission, it is necessary to change the sp^2 phase concentration without changing the diamond grain sizes. Acid treatment is a good method to solve this problem. Yuan *et al.* have speculated that acid etching can remove graphite and non-diamond impurities present in the film and increase the number of micro-protrusions on the film surface [90]. In this experiment, Raman spectroscopy was employed to understand the influence of acid treatment on the field electron emission properties of diamond films.

5.3.1 Sample Preparation

The diamond samples in this experiment were prepared in a microwave plasma enhanced CVD reactor. The reaction source is 1% methane gas mixed with hydrogen. The total flow rate was 50 sccm and the substrate temperature was kept at ~700°C.

The acid treatment was employed by dipping the diamond films in aqua regia (a mixture of hydrochloric and nitric acids with a volumetric ratio of 1:4). The

treatment was carried out at temperature 90°C for 30 min. After this, the samples were thoroughly rinsed with deionized water.

5.3.2 Results and Discussion

The Raman spectra of as-deposited and acid-treated CVD diamond films are shown in Figure 5-16. The as-deposited film (Figure 5-16 a) shows a characteristic peak at ~1332 cm^{-1} indicating formation of the diamond (sp^3) phase. In addition to this a broad hump around ~1580 cm^{-1} indicative of a non-diamond (sp^2) phase is also observed. Thus the Raman spectrum clearly reveals the presence of both the sp^3 and sp^2 phases in the diamond film with the I_D/I_G ratio of 0.78, where I_D and I_G are the intensities of the diamond and graphite peaks, respectively.

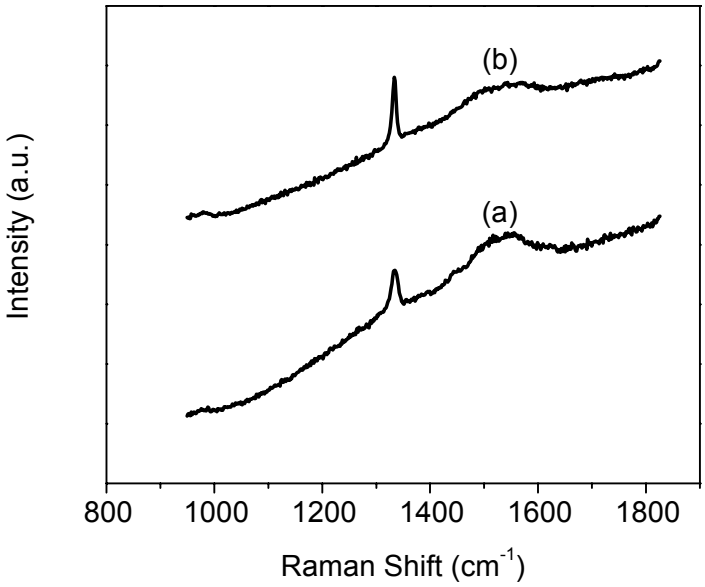

Figure 5-16: Raman spectra of: (a) as-deposited, and (b) aqua regia treated diamond films.

The Raman spectrum of acid-treated diamond film (Figure 5-16b) exhibits spectral features similar to that of as-deposited film but with an I_D/I_G ratio of ~1.02. In comparison with the as-deposited case, a careful observation reveals: (i) reduction in the intensity of the peak corresponding to sp^2 phase and (ii) enhancement in the

intensity and sharpness of the sp^3 peak, and (iii) increase in the I_D/I_G ratio. These observations can be attributed to removal of graphitic content during acid etching. It should be noted that in case of CVD diamond films, Raman scattering from the sp^3 phase is influenced by the amount of sp^2 phase since the scattering efficiency of graphite is higher than that of pure diamond. As a consequence, in the case of diamond films with more sp^2 content, the Raman scattering from the sp^3 phase will be relatively weaker than that from a film with less sp^2 content for the same number of scans. Thus the observed Raman spectrum clearly supports the speculation of removal of graphitic content by the acid treatment.

The *I-E* curves of as-deposited and acid-treated films are shown in Figure 5-17. It is apparent from the *I–E* curves that the field electron emission current at 28 V/μm has reduced from 22 μA to 2.9 μA after the acid treatment. The results demonstrate that field electron emission characteristics of diamond films are influenced by the presence of sp^2 phase in the films. In this experiment, the observed results exhibiting reduction in the emission current and enhancement in the turn-on voltage are due to the removal of the sp^2 phase present in the films by acid treatment, as supported by the Raman spectroscopic studies.

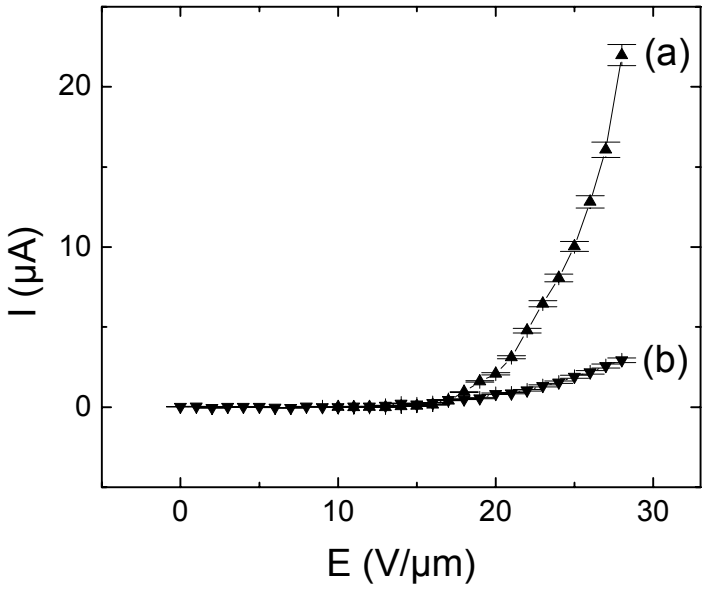

Figure 5-17: FEE *I-E* curves of diamond films before (a) and after (b) acid treatment.

5.3.3 Conclusion

From the observed results, it is clear that the acid treatment of a diamond film leads to the degradation of its field electron emission characteristics. Moreover, in the field electron emission of diamond films, the role of sp^2 content is very important. Diamond films having more sp^2 content show better FEE properties than those with lower sp^2 phase concentration.

Chapter 6

Field Electron Emission Characteristics of Graphitic Nanocones: Deviation of Fowler-Nordheim Plots from Straight Lines

Many researchers have used linear fitting of F-N plots to derive the values of α and β. However, on many occasions the experimental F-N plots cannot be well fitted by a single straight line. In these cases, the values of α and β derived from linear fitting to an F-N plot may not be meaningful. Some recent work tried to explain the nonlinearity in F-N plots by mechanisms such as internal injection at the interface, bulk conduction in the film, the transition from thermionic emission to field electron emission and the space charge effect [59, 91, 92]. In this experiment, the nonlinearity in the F-N plots of graphitic nanocones has been investigated and the results indicate that the nonlinearity in the F-N plots is attributed to the nonuniformity in field enhancement factors of the emitters.

6.1 Sample Preparation and FEE Measurement

Graphitic nanocones were synthesized on the untreated p-type (100) polished silicon wafers in an HFCVD reactor. The H_2 and CH_4 (20%) mixture, introduced by a mutichannel mass flow controller, was used as the reaction source. The typical substrate temperature and deposition time were 700 ºC and 1 hour, respectively. The relatively higher methane concentration and untreated substrate were the main factors that contributed to the growth of graphitic nanocones. Figure 6-1a shows the SEM image of the well-aligned graphitic nanocones. The Raman spectrum in Figure 6-1b

displays the D band at 1350 cm^{-1} and a stronger G band at 1580 cm^{-1}, two characteristic peaks of graphite. The field electron emission characteristics of the samples were measured using anodes with different diameters of 1.5 mm, 2 mm, 2.5 mm, and 3 mm to verify the nonuniform field enhancement factors. The sample size was approximately 4×4 mm^2.

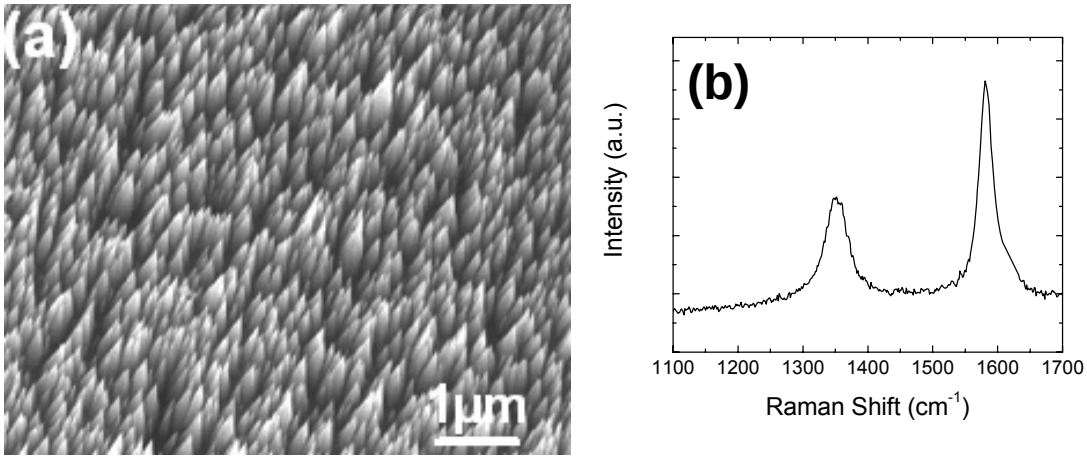

Figure 6-1: SEM image (a) and Raman spectrum (b) of graphitic nanocones.

6.2 Results and Discussion

Figure 6-2 shows the field electron emission F-N plots obtained using different sizes of anodes. The emission current increases with the anode surface area because more nanocones participate in the electron emission when larger probes are used. It was also found that nonlinearity emerges at high electric region in some of the F-N plots. The F-N plots obtained using anodes of 1.5 mm and 2 mm in diameters cannot be fit into one single straight line, but instead require two straight lines with different slopes. At the low electric field region, the F-N plots have smaller slope and so larger FEF than those at the high electric field region. By separate linear fitting in two regions, the FEFs of 493 and 150 were obtained for the anode of 1.5 mm in diameter at low electric field and high electric field, respectively. For anodes with larger diameters, it is appropriate to fit the data to single straight lines. The typical linear fitting parameters for the four anodes with different diameters are listed in Table 6-1. The fact that two different sets of α and β values can be obtained from the F-N plots suggests

that the FEF of graphitic nanocones are not uniform. The FEFs shown in Table 6-1 increase with the probe size, suggesting that the nanocones close to the border of the sample have larger FEFs, presumably due to the edge effect during the synthesis process. This phenomenon of nonuniform FEFs was also evidenced by the FEE scanning test from center to the border of graphitic nanocones using 1 mm probe. It should be noticed that the F-N plot obtained using 1 mm probe is a single straight line, which has been presented in Section 4.2.2 (curve b in Figure 4-8). This is because the electric field range for F-N plot shown in Figure 4-8 ($E = 3 \sim 13$ V/μm or $1/E = 0.08 \sim 0.3$ μm/V) is lower than that for F-N plots shown in Figure 6-2 (>13 V/μm). The nonlinear phenomena occur only at high field region as to be presented as a model in Section 6.3.

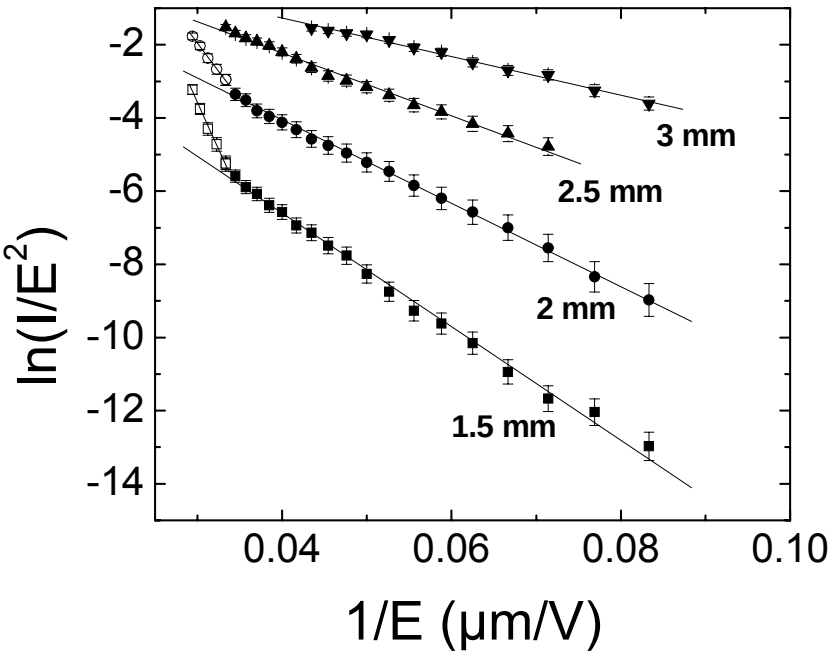

Figure 6-2: Field electron emission F-N plots of graphitic nanocones obtained using anodes with different diameters.

Table 6-1: Results of linear fitting to the experimental data shown in Figure 6-2. β_1 and β_2 are the field enhancement factors derived from the F-N plots at the low and high electric field regions, respectively. α_1 and α_2 are the corresponding effective emission areas.

Probe diameter	β_1	β_2	α_1 (μm^2)	α_2 (μm^2)
1.5 mm	493	150	1.31×10^{-5}	26.2
2 mm	671	249	1.75×10^{-5}	0.1
2.5 mm	892		2×10^{-5}	
3 mm	1454		5.2×10^{-6}	

It was also observed that the deviation of the F-N plot from a straight line reduces with the probe size. For the F-N plot obtained using a 1.5 mm anode, the difference between the slope magnitudes at low and high electric fields is 355. For the anode 2 mm in diameter, the difference reduces to 193. For the anodes of 2.5 mm and 3 mm in diameters, there is no obvious deviation between low and high electric field. The F-N plots can be well fitted into single straight lines representing higher FEFs than those obtained with the smaller anodes.

Bonard *et al.* have found that, for field emitters with large aspect ratios such as CNTs, the FEF measured with a large probe is even higher than that measured from a single nanotube [93]. The result was attributed to the nonuniform FEFs of nanotubes. In large area measurements, the FEF obtained is very close to the FEF of the nanotube with the largest FEF, as the nanotubes with the highest FEF will dominate the emission current [61]. The FEF obtained from any randomly selected nanotubes should not exceed this maximum value. It has also been found that the variation of the work function can lead to the nonlinearity of F-N plot. This is because the slope of the F-N plot, $-B\phi^{\frac{3}{2}}/\beta$, depends on two parameters ϕ and β. The different work function ϕ will produce different slopes, which cause the nonlinearity of F-N plot. It can be speculated that the variation of β can also lead to the nonlinear F-N plot.

It is expected that the FEFs from flat emitters do not vary with probe size. To verify this hypothesis, the field electron emission characteristics of a uniform graphite

film were measured with the same set of anode probes with different diameters as those used for graphitic nanocones. The F-N plots obtained are shown in Figure 6-3. All the plots are almost straight lines and are nearly parallel. The intercept on the vertical axis and therefore the effective surface area α increase with the probe size. Linear fitting of all four F-N plots results in the similar FEF of ~ 120.

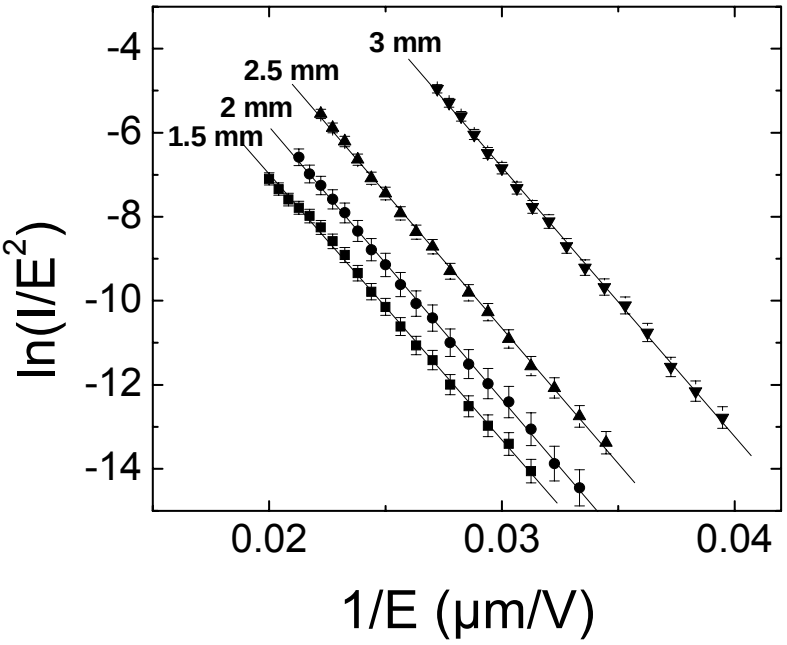

Figure 6-3: Field electron emission F-N plots of flat graphite film obtained using anodes with different diameters.

6.3 Model

In the experiments, the nonuniform nature of the FEF of graphitic nanocones was suggested by the fact that the FEFs increased with anode sizes as listed in Table 6-1. In addition, a 1mm probe was used to perform the field electron emission test in different sites of the sample. The obtained F-N plots are straight lines, a typical one of which has been shown in Chapter 4. By linear fitting, it was found that the field enhancement factors are increased from center to border of the sample. As mentioned above, the slope of an F-N plot is proportional to $1/\beta$. Therefore, the nonlinearity of an F-N plot may emerge if the emission currents from graphitic nanocones with different FEFs coexist on the surfaces probed. To explain the feature of two straight

lines observed in the experiments, the following model is proposed: (i) The nonuniform nanocones are assumed to have two groups with different FEFs of β_1 and β_2, where $\beta_1 > \beta_2$ (the emission contribution from other groups with FEFs smaller than β_2 will be neglected); (ii) At low macroscopic electric field E, electrons only emit from nanocones with the larger FEFs, which corresponds to the section of the F-N plot with a small slope; (iii) At high electric field, nanocones with smaller FEFs also become electron emission sites. The total emission current and thus the F-N plot are determined by the contribution from both groups of nanocones with the larger and smaller FEFs. Therefore, the resultant FEF is expected to be smaller than that of the group with larger FEF, corresponding to the section on the F-N plot with a larger slope.

Based on the above field electron emission model, the nonuniformity of the F-N plots can be quantitatively analysed based on the existing F-N theory. The emission current from the two groups (group 1 and 2) can be separately expressed by the following equations

$$I_m = \alpha_m \beta_m^2 A \phi^{-1} E^2 \exp[-M/(\beta_m E)], \tag{6-1}$$

($m = 1, 2$), where the notation $M \equiv B\phi^{\frac{3}{2}}$ has been used. The total current I_T is thus given by

$$I_T = I_1 + I_2 = A\phi^{-1}E^2\{\alpha_1\beta_1^2 \exp[-M/(\beta_1 E)] + \alpha_2\beta_2^2 \exp[-M/(\beta_2 E)]\}. \tag{6-2}$$

This equation may be re-arranged into the form

$$I_T = A\phi^{-1}E^2 \exp[-M/(\beta_1 E)]\{\alpha_1\beta_1^2 + \alpha_2\beta_2^2 \exp[-M(\beta_1 - \beta_2)/(\beta_1\beta_2 E)]\}, \tag{6-3}$$

where $\beta_1 > \beta_2$ has been assumed, if $\alpha_1 > \alpha_2$, then the contribution from group 2, i.e., the second term in the curly brackets in Equation 6-3, can be neglected. However, if $\alpha_1 < \alpha_2$ and α_1 is so much less than α_2 that the relation $\alpha_1\beta_1^2 < \alpha_2\beta_2^2$ holds, it is possible for both terms in curly brackets in Equation 6-3 to contribute. The relative importance of the two terms changes with E. If a change in the applied electric field occurs, it is clear from Equation 6-3 that the F-N plot may have different slopes in different field ranges.

In order to illustrate the above qualitative analysis, numerical calculations based on Equation 6-3 have been carried out for six groups of graphite emitters (ϕ=5

eV) with FEFs of 3500, 3500/3, 3500/4, 3500/5, 3500/6 and 3500/7, corresponding to groups 1 to 6 marked in Figure 6-4a. The effective emission area is assumed to be 0.05 nm^2 for group 1 and 5 nm^2 for all other five groups. It can be seen from the F-N plots of the six groups that the emission current from group 1 with the largest FEF is much larger than the emission current from any of the other five groups at the low electric fields. With the increasing electric fields, the emission current from the group 2 emitters starts to surpass that from group 1. With further increase of the electric field, the emission current from group 3, and one after another from the other groups, surpasses that from group 1. In order to simulate the influence of nonuniform FEFs, the field electron emission from group 1 is added separately to that from groups 2 to 6. The corresponding F-N plots are depicted in Figure 6-4b and marked as a, b, c, d, and e in which the nonlinear F-N plots are evident for some of the summation combinations. At the low electric region, the field electron emission from the sites with the largest FEF (group 1) plays the major role. The contribution from sites with small FEFs (group 2 to 6) can be neglected. Thus the F-N plot at the low electric field region is almost linear. With the increase of the applied electric field, the emission current of sites with small FEF become comparable to those with the largest FEF due to their large effective emission areas (large intercept in F-N plot). Therefore, F-N plots in the strong electric field region deviate from the straight line. This result is consistent with the experimental observations shown in Figure 6-2, in which the nonlinearity in F-N plots occurs in the strong electric field region. From Figure 6-4b, it can be also found that the deviation of F-N plots from a straight line is less prominent when the difference in FEFs is large within the electric field region investigated. This is also consistent with the experimental results. The nanocones close to the border of the sample have large FEFs as shown in Table 6-1. With the increase of the probe size, more nanocones with larger FEFs at the edge of the sample are covered by the probe. The field electron emission contribution from the nanocones at the center of the sample with much smaller FEFs can be neglected. Therefore, the F-N plot is a straight line. It is expected that the nonlinear nature of the F-N plot for the 3 mm probe in Figure 6-2 will occur at even higher electric fields. However, this region could not be reached in this experiment due to experimental limitations.

In order to compare the experimental F-N plot and the model proposed in this study, the F-N plot has been reproduced for the anode of 1.5 mm in diameter based on the following two methods. Firstly, the FEFs and effective emission areas obtained by separate linear fitting (β_1=493, β_2=150, α_1=1.31 × 10^{-5} μm^2, α_2=26.2 μm^2, as listed in table 6-1) as well as the work function ϕ=5 eV are used in Equation 6-3 and the result is depicted in Figure 6-5a. Secondly, Equation 6-3 with four unknown parameters is used in a one-step fitting procedure using the simplex algorithm [94] to produce the curve b in Figure 6-5. The fitting results are: β_1 = 490, β_2 = 144, α_1 = 1.36 × 10^{-5} μm^2, and α_2 = 29.3 μm^2. It can be seen that both methods result in similar FEF values consistent within 4.0 % and similar effective emission areas consistent within 11.8 %. The χ^2 values describing the goodness of the fitting of the F-N plot, which are given by $\chi^2 = \sum_{i=1}^{N} \frac{(y_i - \bar{y}_{i,\exp})^2}{\sigma_i^2}$, are 0.81 for the separate fitting method corresponding to curve a in Figure 6-5 and 0.34 for the one-step fitting method corresponding to curve b.

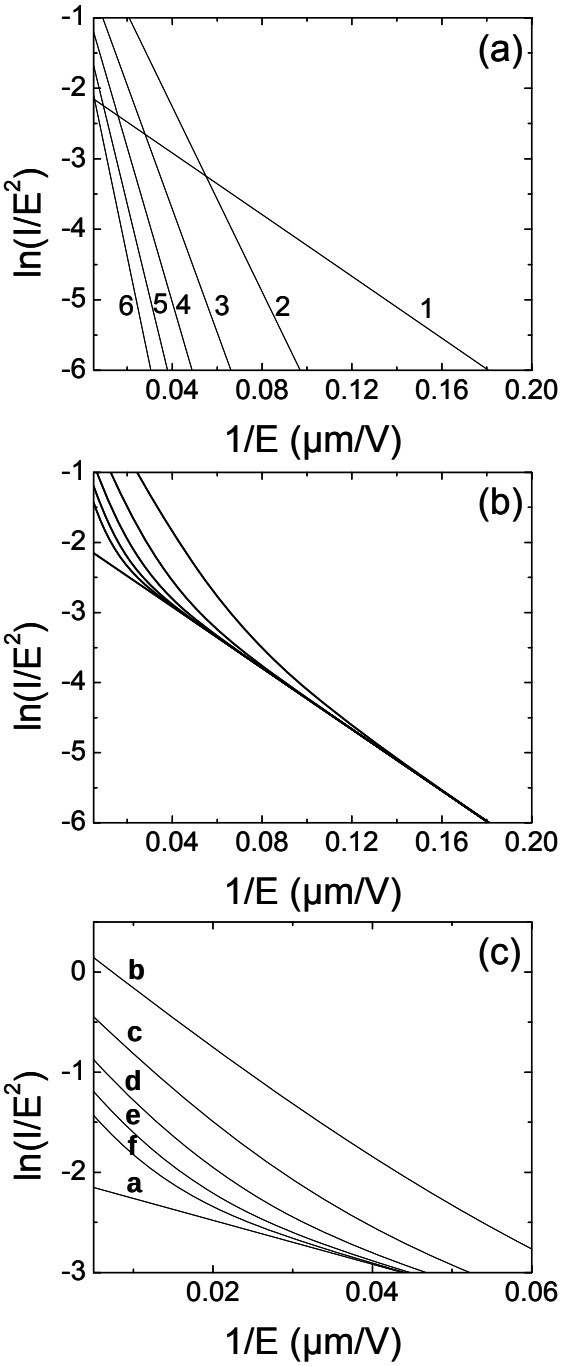

Figure 6-4: Calculated field electron emission F-N plots for emitters with two types of emission sites with different FEFs and effective emission areas: (a) single groups (β_1=3500, α_1=0.05 nm^2; β_2=1167, α_2=5 nm^2; β_3=875, α_3=5 nm^2; β_4=700, α_4=5 nm^2; β_5=583, α_5=5 nm^2; β_6=500, α_6=5 nm^2); (b) summation of FEEs of group 1 and group 2 (curve b), 3 (curve c) , 4 (curve d), 5 (curve e) and 6 (curve f); (c) enlarged plots of (b) in high field region.

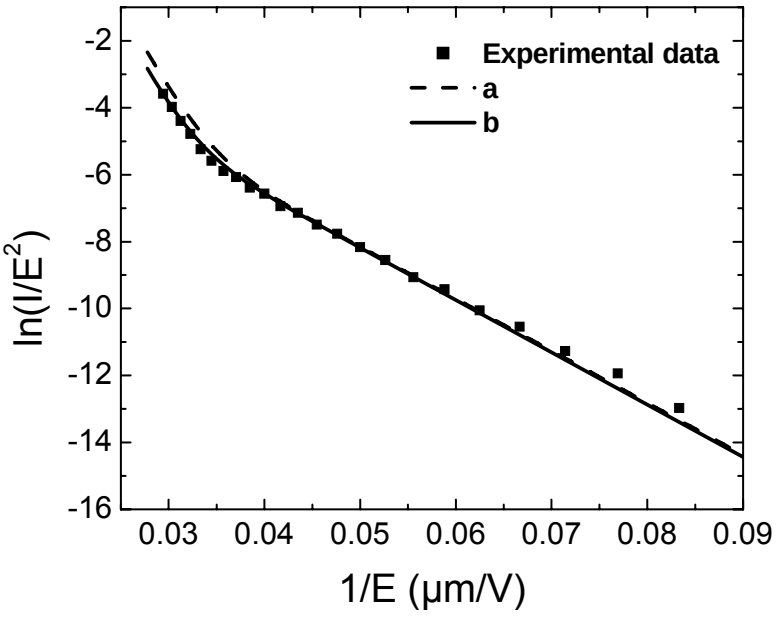

Figure 6-5: Field electron emission F-N plots obtained with the anode of 1.5 mm in diameter: (a) reproduced F-N plots using separate linear fitting parameters in Table 1; (b) one-step fitting.

For comparison, Equation 6-3 for emitters with uniform FEFs ($\beta_1 = \beta_2$) was also analyzed. In this case, Equation 6-3 reduces to

$$I_T = (\alpha_1 + \alpha_2) A\phi^{-1}\beta^2 E^2 \exp[-M/(\beta E)]. \quad (6\text{-}4)$$

In F-N coordinates, it becomes

$$\ln(I_T / E^2) = \ln[A(\alpha_1 + \alpha_2)\beta^2\phi^{-1}] - M/(\beta E). \quad (6\text{-}5)$$

Obviously, the corresponding F-N plots are parallel straight lines. The results show that the uniform FEFs do not produce nonlinear F-N plots as confirmed by the F-N plot shown in Figure 6-3 for a uniform graphite sample.

6.4 Conclusion

In summary, the field electron emission characteristics of graphitic nanocones were investigated using anodes with different diameters. The deviation of F-N plots from a straight line was observed in the field electron emission measurements. The experimental results and numerical calculation demonstrate that the nonlinearity in the

F-N plots originates from the nonuniform FEFs of graphitic nanocones. At the low macroscopic electric field region, electrons are emitted mainly from nanocones with large FEFs, which correspond to an F-N plot with small slope. At the strong electric field, nanocones with small FEFs also become electron emission sites, which reduce the average FEF and so increase the slope of the F-N plot. The FEFs and effective emission areas can be obtained either by separate straight line fitting or by one-step fitting to the summed emission current.

Chapter 7

Conclusion

Some major contributions resulting from the Ph.D. work are concluded below.

7.1 Plasma Enhanced CVD Synthesis of Diamond and Related Carbon-Based Films

The nucleation and growth mechanisms of diamond and related carbon-based films in the microwave plasma enhanced CVD and plasma enhanced HFCVD processes have been investigated. The synthesis of these carbon-based films with controlled structure, morphology and properties has been studied.

This research is motivated by the outstanding properties of diamond which will allow it to operate under high temperature, high radiation and corrosive environments where Si based electronics are inadequate. A range of analytical tools was used in this research. Particularly, some expertise in the use of SEM and Raman Microscopy to analyze diamond and related carbon-based films was acquired. The deposition parameters including the reaction source, gas flow rate, reaction pressure, substrate bias voltage and substrate temperature were varied to obtain different diamond films. In this experiment, the diamond films with different grain morphologies and different sp^2/sp^3 ratios have been deposited by adjusting the gas flow rate and substrate bias voltage.

7.2 Field Electron Emission of Diamond and Related Carbon-Based Films

In the experiment, field electron emission properties of diamond films with different morphologies and compositions were studied. On the one hand, surface

morphology has great influence on the field electron emission properties of diamond films. Firstly, by reducing the grain sizes, the field electron emission properties of diamond films were enhanced due to the increase of effective emission areas. Secondly, diamond films with randomly oriented grains exhibit larger emission current than those with well-oriented grains. The enhancement of the field electron emission property is mainly due to the larger effective emission area of randomly oriented diamond films. Thirdly, for the diamond films with well-oriented grains, the field electron emission properties were enhanced with the decrease of top area of grains. The increase in the field enhancement factor is the main reason for field electron emission enhancement. In addition, special nanostructured diamond films with large aspect ratio, diamond nanocones, have been synthesized successfully. Superior field electron emission property was observed for diamond nanocones due to the very large field enhancement factor. The FEE properties of diamond nanocones can be further enhanced by depositing a layer of nanocrystalline diamond film on the top of nanocones, which is attributed to the local field enhancement in both microscale and nanoscale.

On the other hand, the emission current of diamond films can be increased by increasing the sp^2 phase concentration, which can provide more conduction channels for the electron emission. For diamond films synthesized using H_2 and CH_4, this can be realized by increasing the CH_4 concentration during deposition. For diamond films synthesized using graphite etching, the sp^2 phase concentration can be increased by decreasing the H_2 flow rate during deposition.

In general, microcrystalline diamond films exhibit lower emission current than nanocrystalline diamond films. Among nanocrystalline diamond films, diamond nanocones have larger emission current than the flat nanocrystalline diamond films but smaller emission current than the nanocomposite diamond films. Compared with various diamond films, graphitic nanocones show the strongest emission current of 180 μA at a relatively low electric field of 13 V/μm. The corresponding emission current density (23.0 mA/cm^2) exceeds the industry requirement for a field emission flat panel display (10 mA/cm^2). The diamond nanocone films studied in this experiment have

maximum current density of 11 mA/cm^2 at a higher electric field of 26 V/μm. Its application for FED is promising.

The nonlinear Fowler Nordheim plots of graphitic nanocones were observed. It can be attributed to the influence of spatial nonuniformity in field enhancement factors of graphitic nanocones. A field electron emission model was also proposed to explain this nonlinear phenomenon.

LIST OF REFERENCES

[1] J. C. Angus, A. T. Collins, Electronic era elusive, Nature **370** (1994) 601.

[2] W. A. de Heer, A. Chatelain, D. Ugarte, A carbon nanotube field-emission electron source, Science **270** (1995) 1179.

[3] W. Zhu, G. P. Kochanski, S. Jin, L. Seibles, Electron field emission from chemical vapor deposited diamond, J. Vac. Sci. Technol. B **14** (1996) 2011.

[4] Y. Cheng, O. Zhou, Electron field emission from carbon nanotubes, C. R. Physique **4** (2003) 1021.

[5] H. S. Uh, S. J. Kwon, D. K. Lee, Process design and emission properties of gated n+ polycrystalline silicon field emitter arrays for flat-panel display applications, J. Vac. Sci. Technol. B **15** (1997) 472.

[6] H. Mimura, O. Yilmazoglu, H. Shimawaki, K. Yokoo, K. Mutamba, H. Hartnagel, Emission characteristics of a GaAs wedge emitter monolithically fabricated with an air bridge and a cantilever anode, J. Vac. Sci. Technol. B **21** (2003) 471.

[7] T. Matsumoto, H. Mimura, Point x-ray source using graphite nanofibers and its application to x-ray radiography, Appl. Phys. Lett. **82** (2003) 1637.

[8] J.L. Grand-Clement, Technology, applications and market analysis for Field Emitter Displays (FEDs), in: Proceedings of the 6th IVMC, Newport, RI, 1993 p. 3.

[9] A. Ghis, R. Meyer, P. Ramband, F. Levy, T. Leroux, Sealed vacuum devices: fluorescent microtip displays, IEEE Trans. Electron Devices **38** (1991) 2320.

[10] W.B. Choi, D.S. Chung, J.H. Kang, H.Y. Kim, Y.W. Jin, I.T. Han, Y.H. Lee, J.E. Jung, N.S. Lee, G.S. Park, J.M. Kim, Fully sealed, high-brightness carbon-nanotube field-emission display, Appl. Phys. Lett. **75** (1999) 3129.

[11] P. O'Donovan, The cathode-ray tube's years of TV display dominance are over. What will come next? IEEE Spectrum **12** (2006) 38.

[12] D. Etchells, Canon Expo 2005 - a one-company trade show, the imaging resource, http://www.imaging-resource.com/NEWS/1126887991.html (2006).

[13] S. Sque, Structure of diamond, University of Exeter, http://newton.ex.ac.uk/research/qsystems/people/sque/diamond/structure/ (2006).

[14] P. M. Koinkar, P. P. Patil, M. A. More, V. N. Tondare, D. S. Joag, Field emission studies of CVD diamond thin films: effect of acid treatment, Vacuum **72** (2004) 321.

[15] J. B. Cui, J. Ristein, L. Ley, Electron affinity of the bare and hydrogen covered single crystal diamond (111) surface, Phys. Rev. Lett. **81** (1998) 429.

[16] P. Peinke, P. Kania, P. Oelhafers, Investigation of the nucleation mechanism in bias-enhanced diamond deposition on silicon and molybdenum, Thin Solid Films **270** (1995) 124.

[17] O. Groning, O.M. Kuhel, E. Schaller, P. Groning, L. Schlapbach, Vacuum arc discharges preceding high electron field emission from carbon films, Appl. Phys. Lett. **69** (1996) 476.

[18] C. Wang, A. Garcia, D.C. Ingram, M. Lake, M.E. Kordesch, Cold field emission from CVD diamond films observed in emission electron microscopy, Electron. Lett. **27** (1991) 1459.

[19] N.S. Xu, A.D. Archer, R.V. Latham, The dynamic, simultaneous imaging of both photon-and field-induced electron emission from "electron pin-holes" in planar vacuum-insulated HV electrodes, Surf. Sci. **339** (1995) 194.

[20] R.V. Latham, K.H. Bayliss, B.M. Cox, Spatially correlated breakdown events initiated by field electron emission in vacuum and high-pressure SF6, J. Phys. D **19** (1986) 219.

[21] N.S. Xu, R.V. Latham, Similarities in the 'cold' electron emission characteristics of diamond coated molybdenum electrodes and polished bulk graphite surfaces, J. Phys. D **26** (1993) 1776.

[22] N.S. Xu, R.V. Latham, Y. Tzeng, Field-dependence of the area-density of `cold' electron emission sites on broad-area CVD diamond films, Electron. Lett. **29** (1993) 1596.

[23] M.W. Geis, A. Gregory, B.B. Pate, Capacitance-voltage measurements on metal-SiO_2-diamond structures fabricated with (100)- and (111)-oriented substrates, IEEE Trans. Electron.Dev. **38** (1991) 619.

[24] M.W. Geis, J.C. Twichll, T.M. Lyszczarz, Diamond emitters fabrication and theory, J. Vac. Sci. Technol. B **14** (1996) 2060.

[25] N.S. Xu, R.V. Latham, Coherently scattered hot electrons emitted from MIM graphite microstructures deposited on broad-area vacuum-insulated high-voltage electrodes, J. Phys. D **19** (1986) 477.

[26] N.S. Xu, J.C. She, J. Chen, S.Z. Deng, J. Chen, Microfabrication and characterization of an array of diode electron source using amorphous diamond thin films, Appl. Phys. Lett. **77** (2000) 2921.

[27] J. Chen, S.Z. Deng, J. Chen, N.S. Xu, Substrate nanoprotrusions and their effect on field electron emission from amorphous-diamond films, Appl. Phys. Lett. **80** (2002) 4030.

[28] W.P. Kang, J.L. Davidson, D.V. Kerns, A study of diamond field emission using micro-patterned monolithic diamond tips with different sp^2 contents, Appl. Phys. Lett. **71** (1997) 3394.

[29] V.D. Frolov, A.V. Karabutov, S.M. Pimenov, V.I. Konov, V.P. Ageev, Similarity in field electron emission from nanocrystalline diamond and related materials, Diam. Relat. Mater. **10** (2001) 1719.

[30] J. Bardeen, Theory of work function, Phys. Rev. **49** (1936) 653.

[31] J. Bardeen, The image and Van der Waals forces at a metallic surface, Phys. Rev. **58** (1940) 727.

[32] P. Hohenberg, W. Kohn, Inhomogeneous electron gas, Phys. Rev. **136** (1964) B864.

[33] W. Kohn, L.J. Sham, Self-consistent equations including exchange and correlation effects, Phys. Rev. **140** (1965) A1133.

[34] B.Y. Tong, L.J. Sham, Application of a self-consistent scheme including exchange and correlation effects to atoms, Phys. Rev. **144** (1966) 1.

[35] R.D. Cowan, A.C. Larson, D. Liberman, J.B. Mann, J.Waber, Statistical approximation for exchange in self-consistent-field calculations of the ground state of neutral argon, Phys. Rev. **144** (1966) 5.

[36] N.D. Lang, W. Kohn, Theory of metal surface: charge density and surface energy, Phys. Rev. B, **1** (1970) 4555.

[37] K.L. Jensen, Exchange-correlation, dipole, and image charge potentials for electron sources: temperature and field variation of the barrier height, J. Appl. Phys. **85** (1999) 2667.

[38] O.W. Richardson, On the extraction of electrons from cold conductors in intense electric fields, Proc. Roy. Soc. **A117** (1928) 719.

[39] S. Dushman, Electron emission from metals as a function of temperature, Phys. Rev. **21** (1923) 623.

[40] L.W. Nordheim, The effect of the image force on the emission and reflection of electrons by metals, Proc. Roy. Soc. **A121** (1928) 626.

[41] G.L. Pollack, D.R. Stump, Electromagnetism, Addison Wesley, 2002, p244.

[42] N.A.de Bruyne, The action of strong electric fields on the current from a thermionic cathode, Proc. Roy. Soc. **A120** (1928) 423.

[43] S.C. Miller, R.H. Good, A WKB-type approximation to Schrodinger Equation, Phys. Rev. **91** (1953) 174.

[44] E.L. Murphy, R.H. Good, Thermionic emission, field emission, and the transition region, Phys. Rev. **102** (1956) 1464.

[45] W.W. Dolan, W.P. Dyke, Temperature-and-field emission of electron from metal, Phys. Rev. **95** (1954) 327.

[46] W.W. Dolan, Current density tables for field emission theory, Phys. Rev. **91** (1953) 510.

[47] C.A. Spindt, I. Brodie, L. Humphery, E.R. Westerberg, Physical properties of thin-film field emission cathodes with molybdenum cones, J. Appl. Phys. **47** (1976) 5248.

[48] R. H. Fowler, L. W. Nordheim, Electron emission in intense electric fields, Proc. R. Soc. (London) **119** (1928) 173.

[49] J.H. Schultz, J.V. Minervini, R.J. Thome, A basis for magnet improvements in the U.S. fusion magnet program, http://www.fusion.ucla.edu/snowmass/questions/pq2/42299_1.html (2006).

[50] M. Geis, J. Twichell, N. Efremow, K. Krohn, T. Lyszczarz, Comparison of electric field emission from nitrogen-doped, type Ib diamond, and boron-doped diamond, Appl. Phys. Lett. **68** (1996) 2294.

[51] K. Okano, T. Yamada, A. Sawabe, S. Koizumi, J. Itoh, G. Amaratunga, Metal-insulator-vacuum type electron emission from N-containing chemical vapor deposited diamond, Appl. Phys. Lett. **79** (2001) 275.

[52] Y. Chen, C. Hu, I. Lin, Defect structure and electron field-emission properties of boron-doped diamond films, Appl. Phys. Lett. **75** (1999) 2857.

[53] M. Hiramatsu, K. Kato, C. Lau, J. Foord, M. Hori, Measurement of C_2 radical density in microwave methane/hydrogen plasma used for nanocrystalline diamond film formation, Diam. Relat. Mater. **12** (2003) 365.

[54] S. Y. Chen, M. Y. Lee, C. S. Chen, J. T. Lue, The mechanism of field emission for diamond films studied by scanning tunneling microscopy, Phys. Lett. A **313** (2003) 436.

[55] J. Van der Weide, R. J. Nemanich, Argon and hydrogen plasma interactions on diamond (111) surfaces: Electronic states and structure, Appl. Phys. Lett. **62** (1993) 1878.

[56] J. Van der Weide, R. J. Nemanich, Schottky barrier height and negative electron affinity of titanium on (111) diamond, J. Vac. Sci. Technol. B **10** (1992) 1940.

[57] J. Van der Weide, Z. Zhang, P. K. Baumann, M.G. Wensell, J. Bernholc, R. J. Nemanich, Negative-electron-affinity effects on the diamond (100) surface, Phys. Rev. B **50** (1994) 5803.

[58] W. A. Mackie, J. E. Plumlee, A. E. Bell, Work function measurements of diamond film surfaces, J. Vac. Sci. Technol. B **14** (1996) 2041.

[59] E. S. Cho, C. A. Lee, G. Baek, H. S. Uh, S. J. Kwon, H. Shin, B. G. Park, J. D. Lee, Effects of phosphorus implantation and subsequent growth on diamond, Thin Solid Films **462/463** (2004) 24.

[60] R. Collazo, R. Schlesser, Z. Sitar, Role of adsorbates in field emission from nanotubes, Diam. Relat. Mater. **11** (2002) 769.

[61] J. C. She, N. S. Xu, S. Z. Deng, J. Chen, H. Bishop, S. E. Huq, L. Wang, D. Y. Zhong, E. G. Wang, Vacuum breakdown of carbon-nanotube field emitters on a silicon tip, Appl. Phys. Lett. **83** (2003) 2671.

[62] R. S. Takalkar, J. L. Davidson, W. P. Kang, A. Wisitsora-at, D. V. Kerns, Edge-shaped diamond field emission arrays, J. Vac. Sci. Technol. B **23(2)** (2005) 800.

[63] K.B.K. Teo, M. Chhowalla, G..A.J. Amaratunga, W.I. Milne, G. Pirio, P. Legagneux, F. Wyczisk, D. Pribat, D.G. Hasko, Field emission from dense, sparse, and patterned arrays of carbon nanofibers, Appl. Phys. Lett. **80** (2002) 2011.

[64] A.A. Talin, L.S. Pan, K.F. McCarty, T.E. Felter, H.J. Doerr, R.F. Bunshah, The relationship between the spatially resolved field emission characteristics and the raman spectra of a nanocrystalline diamond cold cathode, Appl. Phys. Lett. **69** (1996) 3842.

[65] W. Zhu, C. Bower, G.P. Kochanski, S. Jin, Field emission properties of diamond and carbon nanotubes, Diam. Relat. Mater. **10** (2001) 1709.

[66] A.V. Karabutov, V.I. Konov, S.M. Pimenov, E. D. Obraztsova, V. D. Frolov, V. G. Pereverzev, and A. A. Smolin, Dielectric-carbon composites for field electron emitters, J. Wide Bandgap Mater. **7** (1999) 68.

[67] F. Lacher, C. Wild, D. Behr, P. Koidl, Electron field emission from thin fine-grained CVD diamond films, Diam. Relat. Mater. **6** (1997) 1111.

[68] S.P. Bozeman, P.K. Baumann, B.L. Ward, M. J. Powers, J. J. Cuomo, R. J. Nemanich and D. L. Dreifus, Electron emission measurements from CVD diamond surfaces, Diam. Relat. Mater. **5** (1996) 802.

[69] V.I. Merkulov, D.H. Lowndes, L.R. Baylor, S. Kang, Field emission properties of different forms of carbon, Solid-State Electronics **45** (2001) 949.

[70] M.W. Geis, N.N. Efremow, K.E. Krohm, J.C. Twichell, T.M. Lyszczarz, R. Kalish, J.A. Greer, M.D. Tabat, A new surface electron-emission mechanism in diamond cathodes, Nature **393** (1998) 431.

[71] S. Lee, S.Y. Han, S.G. Oh, Growth and characterization of defective diamond films, Thin Solid Films **353** (1999) 45.

[72] D.S. Knight, W.B. White, Characterization of diamond films by Raman spectroscopy, J. Mater. Res. **4** (1989) 385.

[73] J. Liu, V.V. Zhirnov, G.J. Wojak, A.F. Myers, W.B. Choi, J.J. Hren, S.D. Wolter, M.T. McClure, B.R. Stoner, J.T. Glass, Electron emission from diamond coated silicon field emitters, Appl. Phys. Lett. **65** (1994) 2842.

[74] W. Zhu, G.P. Kochanski, S. Jin, L. Seibles, Defect-enhanced electron field emission from chemical vapor deposited diamond, J. Appl. Phys. **78** (1995) 2707.

[75] S.S. Proffitt,, S.J. Probert, M.D. Wichael, J.S. Foord, R.B. Jackman, Growth of nanocrystalline diamond films for low field electron emission, Diam. Relat. Mater. **8** (1999) 768.

[76] Y.C. Lee, S.J. Lin, C.T. Chia, H.F. Cheng, I.N. Lin, Synthesis and electron field emission properties of nanodiamond films, Diam. Relat. Mater. **13** (2004) 2100.

[77] S. Gupta, B.R. Weiner, G. Morell, Electron field emission properties of microcrystalline and nanocrystalline carbon thin films deposited by S-assisted hot filament CVD, Diam. Relat. Mater. **11** (2002) 799.

[78] D.M. Gruen, Nanocrystalline diamond films, Annu. Rev. Mater. Sci. **29** (1999) 211.

[79] S. Yugo, T. Kanai, T. Kimura, T. Muto, Generation of diamond nuclei by electric field in plasma chemical vapor deposition, Appl. Phys. Lett. **58** (1991) 1036.

[80] B.R. Stoner, G.H. Ma, S.D. Woltor, J.T. Glass, Characterization of bias-enhanced nucleation of diamond on silicon by invacuo surface analysis and transmission electron microscopy, Phys. Rev. B **45** (1992) 11067.

[81] T. Sharda, M. Umeno, T. Soga, T. Jimbo, Growth of nanocrystalline diamond films by biased enhanced microwave plasma chemical vapor deposition: A different regime of growth, Appl. Phys. Lett. **77** (2000) 4304.

[82] N. Jiang, K. Sugimoto, K. Nishimura, Y. Shintani, A. Hiraki, Synthesis and structural study of nano/micro diamond overlayer films, J. Cryst. Growth **242** (2002) 362.

[83] P. Gonon, E. Gheeraert, A. Deneuvile, F. Fontaine, L. Abello, G. Luazeau, Characterization of heavily B-doped polycrystalline diamond films using Raman spectroscopy and electron spin resonance, J. Appl. Phys. **78** (1995) 7509.

[84] G. Popovici, C.H. Chao, M.A. Prelas, E.J. Charlson, J.M. Meese, Smooth diamond films grown by hot filament chemical vapor deposition on positively biased silicon substrates, J. Mater. Res. **10** (1995) 2011.

[85] N. Jiang, K. Nishimura, Y. Shintani, A. Hiraki, Field electron emission of diamond films grown on the ultrasonically scratched and nano-seeded Si substrates, J. Cryst. Growth **255** (2003) 102.

[86] G.H. Chen, R.Q. Cai, X.M. Song, J.X. Deng, Preparation and field electron emission of microcrystalline diamond deposited on a porous silicon substrate, Mater. Sci. Eng. B **107** (2004) 233.

[87] S.H. Seo, T.H. Lee, Y.D. Kim, C.K. Park, J.S. Park, Electron-emission from nano- and micro-crystalline diamond films: the effects of nitrogen and oxygen additives, Thin Solid Films **447** (2004) 212.

[88] Q. Yang, W. Chen, C. Xiao, R. Sammynaiken and A. Hirose, Synthesis of diamond films and nanotips through graphite etching, Carbon **43** (2005) 748.

[89] Q. Yang, C. Xiao, A. Hirose, Plasma enhanced deposition of nano-structured carbon films, Plasma Sci. Tech. **7** (2005) 2660.

[90] G. Yuan, Y. Jin, C. Jin, L. Han, X. Wang, H. Chen, H. Ji, C. Gu, W. Wang, H. Zhao, H. Jiang, T. Zhou, Y. Tian, J. Vac. Sci. Technol. B **17** (1999) 688.

[91] P. Lerner, N.W. Miskovsky, P.H. Culter, Model calculations of internal field emission and J–V characteristics of a composite n-Si and N–diamond cold cathode source, J. Vac. Sci. Technol. B **16** (1998) 900.

[92] P.W. May, S. Hohn, M.N.R. Ashfold, W.N. Wang, N.A. Fox, T.J. Davis, J.W. Steed, Field emission from chemical vapor deposited diamond and diamond-like carbon films: Investigations of surface damage and conduction mechanisms, J. Appl. Phys. **84** (1998) 1618.

[93] J.M. Bonard, K.A. Dean, B.F. Coll, C. Klinke, Field emission of individual carbon nanotubes in the scanning electron microscope, Phys. Rev. Lett. **89** (2002) 197602.

[94] M. Caceci, W. Cacheris, Fitting curves to data: the Simplex. algorithm is the answer, Byte **9** (1984) 340.